Physics & Astronomy ETDs   Electronic Theses and Dissertations

2-1-2016

Monitoring the Long Wavelength Transient Sky with the LWA1 Telescope

Kenneth S. Obenberger

Follow this and additional works at: https://digitalrepository.unm.edu/phyc_etds

_____

Candidate

_____

Department

This dissertation is approved, and it is acceptable in quality and form for publication:

Approved by the Dissertation Committee:

_____, Chairperson

_____

_____

_____

_____

_____

_____

_____

Monitoring the Long Wavelength
Transient Sky with the LWA1 Telescope

by

Kenneth Steven Obenberger

B.S., Physics and Astronomy, University of Washington, 2010

M.S., Physics, University of New Mexico, 2013

DISSERTATION

Submitted in Partial Fulfillment of the

Requirements for the Degree of

PhD

Physics

The University of New Mexico

Albuquerque, New Mexico

December, 2015

Acknowledgments

I would like to thank several people whom without I would have never got to where I am now:

Greg Taylor for providing excellent scientific and technical advice as well as funding, and for giving me much freedom,

Joe Craig and Frank Schinzel, who collectively taught me a great deal about radio astronomy,

collaborators such as Chin Lin, Jayce Dowell, Namir Kassim, Mike Kavic, Joe Helmboldt, and many other members of the LWA collaboration,

my fishing buddy Andy Ferdinand who helped keep me sane,

my parents, Lisa and Glenn, who always encouraged me and bought me my first telescope,

and finally Jessica Jungwirth for her love, support, and patience.

Monitoring the Long Wavelength Transient Sky with the LWA1 Telescope

by

Kenneth Steven Obenberger

B.S., Physics and Astronomy, University of Washington, 2010

M.S., Physics, University of New Mexico, 2013

PhD, Physics, University of New Mexico, 2015

Abstract

Radio transient astronomy has received a vastly increasing amount of interest within the last few decades. In this time, several new sources have been discovered and many more have been predicted. These sources are spread throughout the radio spectrum, and many emit strongly within the low frequency (10 - 100 MHz) regime. The first station of the Long Wavelength Array (LWA1) is a compact array of 260 dual polarization dipole antennas operating between 10 and 88 MHz. With good sensitivity, high time and frequency resolution, and an instantaneous field of view up to $\sim 20,000$ deg^2, the LWA1 an ideal instrument for searching for transient phenomena. This dissertation presents transient work done with the LWA1, which includes a search for prompt emission from gamma ray bursts as well as a blind search for unspecific transients. These searches resulted in new limits on astronomical transients and the discovery of radio emission from large meteors (fireballs). This dissertation also presents a highly sensitive followup study on the fireball emission, which has yielded new insight into the origin of the emission, suggesting that it is emission of plasma waves within the plasma trail.

Contents

Contents

Contents

Contents

List of Figures

List of Figures

List of Tables

Glossary

BAT   Burst Alert Telescope, transient finding telescope aboard the Swift Satellite, operating between optical and X-ray wavelengths.

Dec   Declination: latitudinal coordinate in the earth based elliptical system used in astronomy.

DM   Dispersion measure: value used by transient astronomers, and describes the frequency time dispersion caused the free electrons between a source and the observer.

ELF   Extremely Low Frequency: Frequency range between 3 Hz and 3 kHz

EMP   Electromagnetic Pulse: Very short (μs) pulse of electromagnetic radiation.

FWHM   Full Width at Half Maximum: The angular width of a beam greater than half of the maximum value.

GBM   Gamma-ray Burst Monitor: GRB detecting telescope aboard the Fermi satellite.

GCN/TAN   Gamma-ray Coordinates Network / Transient Astronomy Network: a NASA operated system for alerting astronomers of transient

events.

GRB	Gamma-Ray Burst: Flash of gamma-rays, thought to be caused by merging neutron stars (short), and collapsing stars (long).
HF	High frequency: Frequency range between 3 and 30 MHz
IGM	Intergalactic Medium: The material between Galaxies.
Jy	Jansky: Unit of flux density used by radio astronomers. 1 Jy$= 10^{-26}$ W m^{-2} Hz^{-1}.
FRB	Fast Radio Burst: a type of highly dispersed millisecond radio pulse currently observed near 1.4 GHz
LHC	Left-hand Circular polarization
LOFAR	The Low Frequency Array: A low frequency radio telescope operating between 30 and 250 MHz, located in various countries around Europe. Operated by ASTRON in the Netherlands.
LWA	Long Wavelength Array: a future aperture synthesis radio telescope consisting of 53 stations similar to LWA1
LWA1	The first LWA station, now operating as a single-station radio observatory.
LWA-OVRO	An independent LWA observatory located at Owens Valley Radio Observatory in California.
LWA-SV	A LWA observatory located at Sevilleta National Wildlife Refuge in Central New Mexico.
LWDA	The Long Wavelength Demonstrator Array: a 16 stand dipole array.

Glossary

MAXI	Monitor of All-sky X-ray Image: An X-ray transient finding space telescope.
MWA	The Murchison Wide-field Array: A low frequency radio telescope operating between 80 and 300 MHz, located in Western Australia.
NED	NASA/IPAC Extragalactic Database: Database of extragalactic sources made available by NASA.
PASI	Prototype All-Sky Imager: A correlating and Imaging backend for LWA1.
PASIFx	The PASI correlation software.
RA	Right Ascension: Longitudinal coordinate in the earth based equatorial system used in astronomy.
RHC	Right-Hand Circular Polarization
RFI	Radio Frequency Interference
RMS	Root Mean Square
SEFD	System Equivalent Flux Density
Swift	A space telescope equipped with several instruments for detecting transients.
TBN	Transient Buffer Narrowband (an LWA1 "all sky" observing mode).
TBW	Transient Buffer Wideband (an LWA1 "all sky" observing mode).
UVOT	UV/Optical Telescope: A ultraviolet and optical telescope aboard the Swift Satellite.
VHF	Very High Frequency: Frequency range between 30 and 300 MHz

Glossary

VLA   The Karl Jansky Very Large Array: A wideband radio telescope, consisting of 27 25 meter dishes, configurable in a Y-shape. Located in central New Mexico

VLSS   The Very Large Array Low-frequency Sky Survey: A VLA survey of the sky at 74 MHz.

VLF   Very Low Frequency: Frequency range between 3 kHz and 3 MHz

XRT   X-Ray Telescope: The X-Ray telescope aboard the Swift Satellite.

Chapter 1

Introduction

Low frequency radio astronomy (< 100 MHz) is a relatively unexplored field. Despite early interest in low frequencies, the past several decades have seen the majority of radio astronomy research focused at high frequencies. Recent advancements in technology combined with renewed interest has sparked the construction of several highly sensitive low frequency telescopes, such as the Low Frequency Array (LOFAR;van Haarlem et al., 2013), the Murchison Wide-field array (MWA;Bowman et al., 2013) and the Long Wavelength Array (LWA1; Taylor et al., 2012; Ellingson et al., 2013a) opening up new opportunities in the low frequency regime. LOFAR operates from 30 to 250 MHz, and has many stations located in various countries within Europe. MWA operates between 80 and 300 MHz, located in Western Australia. The LWA1 operates from 10 to 88 MHz and is located in central New Mexico.

While there are many targets for these new, low frequency telescopes, transient phenomena have been a key component to the scientific motivation. Several of these telescopes have been designed with very large fields of view (sometimes the entire sky), which is extremely helpful when conducting a search for objects of unpredictable origin.

In recent decades a large variety of sources have been theorized to produce coherent, transient radio emission on timescales of milliseconds to minutes at frequencies below 100 MHz. Many of these sources would have a large scientific impact if discovered, providing a wealth of knowledge about the physics and composition of both the sources themselves and their surroundings.

1.1   Transients: Extragalactic

Among these sources are several interesting extragalactic candidates. Gamma-Ray Bursts (GRBs; Usov & Katz, 2000; Sagiv & Waxman, 2002), neutron star mergers (Hansen & Lyutikov, 2001; Pshirkov & Postnov, 2010; Moortgat & Kuijpers, 2004; Yancey et al., 2015), primordial black holes (Rees, 1977; Blandford, 1977; Kavic et al., 2008). The predictions of prompt radio counterparts to these sources is highly dependent on the physical evolution of the progenitors and their subsequent explosions. Furthermore the signature and strength of any radio emission generated by a source can be modified by its immediate surroundings as well as the intergalactic medium. A measurement of the frequency/time dispersion of a pulse gives the electron column density between the observer and the source. Similarly a measurement of the temporal broadening due to scattering gives information about the inhomogenaties present within the intervening plasma. Thus a detection of radio emission from one of these progenitors would not only aid in the understanding of these mysterious sources themselves but also shed light on their immediate surroundings as well as the larger scale structure of the universe (Ioka, 2003; Inoue, 2004; Zhou et al., 2014).

Considering these potential uses it is no mystery why the newly discovered fast radio bursts (FRBs), ~ 1 ms pulses found near 1.4 GHz, have created such a buzz within the radio transient community (Lorimer et al., 2007; Keane et al., 2012; Thornton et al., 2013; Spitler et al., 2014; Petroff et al., 2015). These sources, currently of

unknown origin, show an extreme amount of dispersion, which suggests that they may be coming from great distances (redshifts $z \sim 1$). Most events have been measured to have flux densities near 1 Jy, and while their spectrum is not well characterized, a steep spectrum could provide the potential for expanded studies at low frequencies where the pulses could be very bright.

1.2   Transients: Galactic

Interest is not just limited to those objects at great distances. Within our own galaxy there are numerous targets of high scientific value. Pulsars are known to emit single giant pulses, orders of magnitude brighter than their cyclic pulses, the Crab pulsar being the most famous giant pulse emitter (Ellingson et al., 2013b; Wei et al., 2015).

Rotating Radio Transients (RRATs) are another example of a known radio transient, detectable at low frequencies (McLaughlin et al., 2006). These sources produce pulsar-like bursts, with similar dispersion and pulse durations. However the occurrence of pulses is intermittent, as opposed to perfectly periodic pulse nature of pulsars. RRATs are thought to be pulsars where some of the pulses are either blocked or not emitted.

Related to pulsars, neutron stars with extreme magnetic fields (magnetars) have recently been observed to produce radio bursts at higher frequencies (Cameron et al., 2005). These detections suggest that flaring magnetars may be detectable at low frequencies.

A very strong (~ 1 Jy), long duration (~ 10 min), coherent transient has been detected near the Galactic center at 330 MHz (Hyman et al., 2005). The source repeatedly bursts every ~ 1.27 hours, but the origin is currently unknown. Two other transients of even longer duration have also been observed near the Galactic

center at 235 and 330 MHz (Hyman et al., 2009, 2002). The transient reported in Hyman et al. (2009) had a peak flux density of 100 mJy, and had a very steep spectrum, opening the possibility of detection at lower frequencies.

Even closer to home, Jupiter has long been known to be a bright radio transient at frequencies below 40 MHz (Burke & Franklin, 1955). This emission is due to a cyclotron-maser created within plasma flowing towards the planet along the geomagnetic field lines in the auroral regions. By analogy Jupiter sized extroplanets are highly likely to emit at low frequencies (Stevens, 2005). Hot Jupiters, which are very close to their parent star are particularly favorable for large amplitude emission since the incoming particle flux would be so high. At higher frequencies similar auroral emission has been observed coming from M dwarf stars and substellar brown dwarfs (Hallinan et al., 2008), which have a strong magnetic field and therefore emit at higher cyclotron frequencies. Detection of auroral emission from extrasolar planets would allow for accurate field strength measurements of those planet's magnetic fields.

This auroral emission is not to be confused with the bursting emission from flaring stars, where eruptions on the surface of stars eject energetic particles. Radio emission from stellar flares have been detected at higher frequencies since the 1960s (Lovell, 1963). These flaring stars however have yet to be detected at lower frequencies, but are likely to do so considering the analogous low frequency emission from the Sun's radio bursts (Reid & Ratcliffe, 2014).

1.3 Transients: Atmospheric

While of less interest to the broader astrophysics community, there are a large number of transient radio sources that occur within our own atmosphere and can be studied with low frequency radio telescopes. Lightning for instance generates very

strong low frequency broadband pulses, which have been studied by low frequency interferometers (Warwick et al., 1979; Obenberger et al., 2015a).

Low frequency radio telescopes can also employ passive radar techniques to study both the ionosphere and meteor plasmas (Helmboldt et al., 2013, 2014). These techniques typically utilize a strong transmitter, such as an analog TV station or FM radio. These signals are scattered off of high altitude plasmas, such as the trails left by meteors, and are then detectable from the ground. With knowledge of the frequency of the transmitter, the radial velocity of the plasma can be calculated via the Doppler effect.

Furthermore scintillation of celestial sources can be used as a probe of the ionospheric plasma. Recently a study with the MWA (Loi et al., 2015) used the positional offset of thousands of sources over a very large field of view to map the plasma distribution, finding large scale structure following the geomagnetic field lines.

As will be shown in chapters 4 and 5 it has been a surprise to find that the plasma trail left behind by some large meteors radiates at frequencies below 60 MHz (Hawkins, 1958; Obenberger et al., 2014b). Large meteors have been shown to create short (~ 1 s) Very Low Frequency (VLF, 3 to 30 kHz) and Extremely low Frequency (ELF, 3 Hz to 3 kHz) pulses coincident with entry (Keay, 1980; Beech et al., 1995). Recent studies have also shown that meteors most likely create a very short (μs) electromagnetic pulse (EMP) immediately after vaporization similar to a nuclear weapon detonation (Close et al., 2010, 2013). These meteor related EMPs may be detectable within our own atmosphere or even on the surface of the moon.

1.4 Past Searches

Due to a historic lack of low frequency telescope facilities, there have been very few limits placed on low frequency transients. Recently two searches at 142 MHz with LOFAR limited low frequency emission from FRBs and other short duration transients (Coenen et al., 2014; Karastergiou et al., 2015). Karastergiou et al. (2015) showed that FRBs of 5 ms duration, brighter than 62 Jy could not occur more than $29 \, \mathrm{sky}^{-1} \, \mathrm{day}^{-1}$. This is much lower than that of the FRB rate measured at 1.4 GHz, but it does not eliminate the potential for future low frequency detection of FRBs since the pulses would most likely be scatter broadened, spreading the pulse energy over a longer duration. Furthermore 62 Jy is much larger than the observed ~ 1 Jy flux density at 1.4 GHz for many FRBs, requiring the spectrum to increase in flux density at lower frequencies at rate nearly ν^{-1}.

Bell et al. (2014) used the MWA to place limits on long duration transients of timescales of 30 minutes at 154 MHz over a large field of view. Similarly Murphy et al. (2015) obseved 17 known Jupiter-class exoplanets using the MWA, placing 3 to 115 mJy limits on emission from these systems.

LOFAR and the MWA have both been probing the transient universe at frequencies above 100 MHz, placing new limits in that regime. However to date there have been very few blind searches for transients below 100 MHz (Kardashev et al., 1977; Lazio et al., 2010; Cutchin, 2011), and none of these studies have resulted in a detection.

Kardashev et al. (1977) used several observing stations (including the Mars 7 space probe) spread by many kilometers, to search for transient pulses at frequencies between 30 and 550 MHz. The distance between stations allowed for anti coincidence between pulses. This study found no pulses, except those coming from the Sun. They limited the 0.5 s pulses to $< 10^{-3} \, \mathrm{yr}^{-1} \, \mathrm{deg}^{-2}$, and quote 5 σ sensitivities of $\sim 4 \times 10^4$

Jy at 38 and 60 MHz. No dedispersion was carried out for these observations.

Lazio et al. (2010) used the Long Wavelength Demonstrator Array (LWDA), the precursor to the LWA project, to limit transients on 300s timescales at 74 MHz. With an all-sky field of view, 106 hours of observation, and a 5 σ sensitivity of 2500 Jy, they limited transients of those parameters to $< 10^{-2}$ yr^{-1} deg^{-2}. No dedispersion was carried out for these observations.

Finally Cutchin (2011) used the Eight-meter-wavlength Transient Array (ETA) to search for dispersed transients with pulse widths of 3 s, at 38 MHz, with 3.75 MHz of bandwidth. The ETA was reported to have an estimated 5 σ sensitivity of ~ 780 Jy, and in 30 hours of observations, limited transients of these parameters to < 0.25 yr^{-1} deg^{-2}.

With so many potential low frequency transient sources and so few attempts to find them, this field of research has high potential for discovery. A blind "agnostic" search covering a large field of view with a sensitive telescope could yield the discovery of any of the many sources discussed above. The highly sensitive LWA1 telescope (Ellingson et al., 2013a), with its good time resolution and all-sky capabilities make it a great transient search telescope, surpassing the abilities of the instruments used in prior transient searches.

1.5   This Dissertation

This dissertation is a compilation of searches for and studies of transients at low frequencies using the LWA1 telescope. Chapters 3, 4, and 5 are all slightly modified published papers. A fourth published paper has been modified and split into Chapters 2 and 6. The chapters are presented in a logical but not chronological order. This may be confusing to the reader and therefore a description of the chapters is

necessary.

Chapter 2 is taken from a paper describing the Prototype All-Sky Imager (PASI), a backend correlator of the LWA1 telescope (Obenberger et al., 2015a). This paper was published after the contents of Chapters 3 and 4 were published but given the fact that both Chapters 3 and 4 contain research using PASI, it is logical to present the full description of that system before discussing the results derived from it. Obenberger et al. (2015a) also contained rate density and energy density limits for 13,000 hours of data. These limits are out of date and therefore not included in this chapter. It should be noted that I, the author of this dissertation and first author of the Obenberger et al. (2015a), did not build nor design PASI. The hardware and software sections of this chapter (§2.2 and 2.3) describe components designed and built by several of the other co-authors; specifically Jake Hartman did a large fraction of this work.

Chapter 3, which describes a search for prompt radio emission from GRBs, was the first paper presented in this dissertation to be published (Obenberger et al., 2014a). In this study we searched only the data that was recorded around the times of 34 GRBs, but ignored the bulk of the data archive. We omitted the rate density and pulse energy density limits originally recorded in this paper since they are out of date. Also we removed the portion of the introduction that briefly describes the LWA1 and PASI, since these are covered in Chapter 2. The original paper contained estimates of the RMS that were nearly a factor of 2 greater than those later derived by a more rigorous process and presented in Chapter 2. Therefore the GRB limits presented in Chapter 3 have been modified to represent the more accurate values.

In the limited data used for the GRB study we did discover two transients that were not related to any GRBs. Sparked by this discovery we developed a pipeline to search a much larger volume of data, and used it on 11,000 hours of data, in which we found an additional 42 transients, bringing the total to 44. We were then

able to show that these transients were evidence of radio emission from large meteors (fireballs), by correlating them with events from the NASA All-Sky Fireball Network. We then used archived events from the Fireball Network to find 5 more events in old PASI movie files, which were not searchable by the pipeline. This then brought the total number of transients to 49, the majority of which were most likely fireballs (Obenberger et al., 2014b). The contents of this paper are presented in a modified format in Chapter 4.

The contents of Chapter 5 are currently under review for publication. This chapter describes a followup study to the discovery of meteor radio emission. For this study we used both PASI as well as beam formed observations to record the first ever broad band dynamic spectra of meteor radio emission. We describe these spectra in detail and also report a total of 104 detected transients found in 16,000 hour of data. The vast majority of these transients we assume to be fireballs. This chapter also presents our current theory on the nature of the radio emission.

Finally in Chapter 6 we give the most up-to-date rate density and pulse energy density limits of astronomical (non meteor) transients at 38, 52, and 74 MHz. These limits are derived from 16,000 hours of observations, and we compare these results to the previous studies discussed in §1.4. This chapter was originally published as (Obenberger et al., 2015a), which only included analysis of 13,000 hours of data.

Chapter 2

Monitoring the Sky with the Prototype All-Sky Imager on the LWA1

Abstract: We present a description of the Prototype All-Sky Imager (PASI), a backend correlator and imager of the first station of the Long Wavelength Array (LWA1). PASI cross-correlates a live stream of 260 dual-polarization dipole antennas of the LWA1, creates all-sky images, and uploads them to the LWA-TV website in near real-time. PASI uses a permanent archive to store all-sky images at frequencies between 10 and 88 MHz creating opportunities for new research and discoveries.

2.1   Introduction

The first station of the Long Wavelength Array (LWA1; Ellingson 2013; Taylor 2012) is a radio telescope which operates between 10 and 88 MHz. The telescope consists of 256 dual-polarization dipole antennas (Hicks et al., 2010) distributed within a 100 × 110 m ellipse, with 5 additional outlier antennas with distances between 200 to 500 m from the center of the main array. The array is collocated with the Karl Jansky Very Large Array (VLA) at a latitude of 34.070° N and a longitude of 107.628° W.

The beam pattern of each LWA1 antenna is sensitive to nearly the entire sky and, therefore, delay tracking for specific sources is not necessary. Rather since all-sky images are the desired result, the array can simply be phased to zenith. This fact makes interferometry with a dipole-based array simpler than a typical array using dishes.

Several observing programs have recorded a small amount of raw LWA1 data and correlated it for different scientific applications, including ionospheric and meteor studies (Helmboldt et al., 2013, 2014). However, since the raw data rate is so large (357 GB/hr), recording it to disk for later correlation is not feasible for large scale, blind transient searches, which are one of the main science drivers of the LWA1. Instead realtime correlation and imaging is the preferred method of observing, because it enables a large reduction in the data rate.

The Prototype All-Sky Imager (PASI) is a backend to the LWA1 that correlates and images the live stream of all LWA1 antennas and uploads the images to the LWA-TV[1] website in near real-time. The all-sky images are also are stored in a permanent archive where they can be accessed by anyone. Previous and ongoing projects have used this data to discover non-thermal radio emission from large meteors [fireballs; Obenberger et al., 2014b (Chapter 4)] and place limits on both prompt low frequency

---

[1]http://www.phys.unm.edu/~lwa/lwatv.html

radiation from GRBs and general transients [Obenberger et al., 2014a (Chapter 3); Chapter 6].

This chapter describes the PASI system and is organized as follows: §2.2 describes the PASI computing hardware. §2.3 describes the correlation and imaging software. §2.4 describes the data output from PASI and its calibration and analysis. §2.6 discusses the outreach and education benefits of PASI. Finally, in §2.7 we present our conclusions.

2.2   Hardware

The PASI computing cluster consists of 4 nodes. All nodes contain two quad-core Nehalem 2.93 GHz processors and 12 GB of RAM, except for node 4 which has 14 GB of RAM. The nodes are connected using an Infiniband switch. Processing tasks are divided between the nodes. Node 1 reads the TBN stream and handles the polyphase fast Fourier transform (FFT), Node 2 runs the correlator, and Node 4 runs the imager, leaving Node 3 for user post-processing and as a spare node in case one of the others irreparably fails. During operation the 15 minute averaged processing loads[2] on each of the nodes are as follows: Node 1 $\sim$ 4.7, Node 2 $\sim$ 0.2, and Node 4 $\sim$ 1.8. Since each node has two quad core processors with 2 threads per core, none of the nodes are overloaded.

The cluster has an internal storage capacity of 7.5 TB, with eSATA ports for connecting external storage as needed. Currently PASI is connected to 17 TB of external storage, 15 TB of which are dedicated to a ring buffer for visibilities. The other 2 TB are used as a swappable image archive. Output data from PASI can be accessed on the external hard drives and be copied over fiber to other machines.

---

[2]A load number of 0 represents an idle computer, any process using or waiting for CPU increments the load number by 1.

PASI can also be controlled remotely and used for post-processing without having to copy the data to other machines.

PASI is located within the electronics shelter of the LWA1. Figure 2.1 shows a flow chart that describes how PASI interfaces with the LWA1 system. The signals received from each antenna are impedance matched and pre-amplified by the front end electronics (FEE) at each stand. The generated signals are then passed on to the analog receiver boards (ARX) inside the electronics shelter where they are further amplified and filtered. After that, the digital processor (DP) converts the analog signals to digital complex voltages for further processing.

DP can operate in two modes: digital beam forming and transient buffer (Elling-son et al., 2013a). The transient buffer provides the linearly-polarized voltage time series from all antenna stands, and has two submodes: wideband and narrowband. Wideband (TBW) allows for the entire 78 MHz bandwidth output from the ARX to be collected in a 61 ms burst every $\sim$ 5 min. Narrowband (TBN) provides a stream of 100 kSPS allowing for a single tuning of 100 kHz (75 kHz[3] usable) to be collected continuously. DP is configured such that the TBN data is duplicated between PASI and a data recorder (DR). This allows data to be both recorded for later processing and correlated in near real-time by PASI.

2.3   Software

2.3.1   Correlation

Correlations of the digitized voltages are achieved using a software FX correlator (PasiFx) written using a highly modular design to facilitate testing and modification

---

[3]The filter rolloff removes 25 kHz of bandwidth.

of multiple components in parallel by multiple developers.

The initial FX correlator code was developed at Los Alamos National Laboratory as part of their contribution to the LWA and was modified further at the University of New Mexico (UNM). The code's primary tasks are divided between the four nodes in the cluster, and it is highly threaded to take advantage of the multiple CPU cores per node.

Data can be input into PasiFx (Fig. 2.1) from three different sources: (1) Self-generated simulated antenna data, which produces Gaussian noise plus the signals from a number of user-specified point sources in the sky, (2) a stream of TBN data from DP, through the DR, via the 10 GbE connection to the DR, and (3) raw TBN data saved to a disk, which was mainly used during the testing and commissioning phase and is useful for debugging. Normal PASI operation uses the live stream of TBN.

PASI receives the stream of TBN time series at a rate of 357 GB/hr. However, due to a limited number of inputs into DP one of the antennas from the main array is not used, resulting in the correlation of 260 dual polarization antennas. The voltages are then Fourier transformed and all 33,670 pairs are correlated to produce the full linear polarization products XX, YY, XY, and YX. Each visibility covers 100 kHz of bandwidth (75 kHz usable) with eight 12.5 kHz channels and are integrated for 5 seconds[4]. For each integration PasiFx outputs a CASA measurement set, containing all the visibilities. Figure 2.2 shows the snapshot (u, v) coverage of the inner core of the LWA1, and Figure 2.3 shows perpendicular (l, m) slices of the model PSF generated from the (u, v) snapshot in Figure 2.2.

The final data rate of the visibilities is 5 GB/hr, roughly 1% of the data rate of

---

[4]Integrations for near real-time imaging can be as fine as 1 s, however the CPU burden at <5 s causes overheating. Therefore, PASI has almost exclusively been run at 5 s integrations.

TBN into PASI. The visibilities are saved for ∼4 months on a 15 TB ring buffer. This allows for a considerably lengthy time frame in case an interesting transient is found in the image data and reanalysis of the visibilities is needed.

Before correlation PASI also extracts and saves the averaged spectrum from all the antennas for each 5 s interval, with 256 390 Hz channels. The averaged spectra are used for identifying bright radio frequency interference (RFI) when searching for transients.

2.3.2   Imaging

Due to a lack of computational resources and input sky models PASI only produces dirty images of the uncalibrated visibilities[5]. The measurement sets are imaged using the Fourier transform and summing features of the CASA CLEAN script (McMullin et al., 2007), but without any deconvolution using the CLEAN algorithm (niter = 0). We phase the visibilities to zenith so that the sky is projected onto a 2D circle with zenith at the center. We also use natural weighting with no (u, v) taper. The pipeline produces dirty images for each of the four Stokes parameters[6] and is executed within a Python-based pipeline outside of the normal CASA-Python interface. Each image is averaged over the inner six channels, which cover the 75 kHz of usable bandwidth. The image and cell size depends on the frequency, for 38 MHz we use 128×128 pixels with a cell size of $1° \times 1°$, we use larger image size and smaller cell size for higher frequencies and vice versa for lower frequencies.

The images, averaged spectra, and metadata are saved within a binary file onto an

---

[5]All antenna signal paths have been delay calibrated and these delays are used by the correlator. However, no additional phase or amplitude calibration, i.e., self calibration, is applied to the visibilities.

[6]Stokes I is total intensity, Stokes ±Q are the North/South and East/West linear polarization components, Stokes ±U are the linear components offset +45° from Stokes ±Q, and Stokes ±V are the right and left hand circular polarization components.

external disk. Metadata includes a time stamp, integration length, central frequency, and bandwidth. New files are generated every hour or every time the center frequency is changed. The images are also uploaded to the LWA-TV website where the Stokes I and V images, as well as the averaged spectrum, are displayed in near real-time. Figure 2.3 shows an example of the LWA-TV display with an equatorial coordinate grid overlaid.

The final data rate for the images is 200 MB/hr, roughly 0.06% of the raw TBN. This data rate is small enough to allow for a permanent archive with infrequent disk swaps. While the initial intent of PASI was to run 24 hours a day, this cannot be accomplished. Down time is primarily due to the fact that currently beam observations degrade TBN observing when both modes operate in parallel. Since April 2012 PASI has been observing an average of 16 hours a day.

2.4 Data and Analysis

The previous sections contain all the processing implemented automatically by PASI. Post processing requires user implementation either from a local computer or remotely from PASI.

2.4.1 Flux Calibration

Flux calibration for PASI is determined for different frequencies as a function of elevation. The primary beam pattern of PASI is essentially the combined beam patterns of the two dipole antennas of an individual antenna stand. To measure this we simply extract the observed power received for Cygnus A and fit it with a 3rd order polynomial. Figure 2.5 shows the measured normalized power pattern at 38 MHz of Cygnus A and Cassiopeia A. The data was chosen from seven days across a

year to show annual and diurnal consistency. This figure also shows the polynomial model derived for Cygnus A. The same procedure was carried out at 52 and 74 MHz, and the derived models were used when calibrating other sources as well as calculating the root mean square (RMS) of the image noise. The models were scaled using interpolated flux densities from the VLSS Bright Source Spectral Calibrator[7] (Helmboldt et al., 2008), which is based on values from Baars et al. (1977). The values used for Cygnus A at 38, 52, and 74 MHz are 25.5, 21.215, and 17.25 kJy.

It should be noted that the measured flux of any given source is affected by both the diffuse Galactic emission surrounding it and the side lobes of other sources in the image. In particular, large negative bowls arise due to the combined side lobes of bright sources and the diffuse Galactic emission. As can be seen in Figure 2.3 much of the PSF of the dirty beam is negative; therefore the added contribution from many sources can create negative bowls. The depth, size, and location of these negative bowls depends on what sources are present in the sky. Since Cygnus A and Cassiopeia A, the two point sources which contribute the most to the negative bowl, do not contribute to the negative bowl in their own locations, they are inherently less affected. Moreover since they are an order of magnitude brighter than the next brightest point source, they are fractionally affected least by the negative bowls. Other sources such as Taurus A and Virgo A are sufficiently affected by negative bowls that they do not accurately portray the primary beam pattern, and are therefore not used when calibrating.

Over 90% of the data collected by PASI have been at center frequencies of 38, 52, and 74 MHz, with 71%, 11%, and 10% recorded at those frequencies respectively. Therefore, flux calibration and sensitivity estimates have been obtained at these frequencies only.

---

[7]http://www.nrl.navy.mil/rsd/vlss/calspec/

2.4.2   Sensitivity

The zenith angle dependent RMS noise for PASI is calculated by calibrating the noise from pixels spread every degree from east to west running through zenith. This method provides estimates of 47 ± 13, 34 ± 11, and 45 ± 11 Jy at zenith for 38, 52, and 74 MHz. The large range (± 13 and ± 11) in these values is due to confusion from the Galactic plane. Figure 2.6 shows the calculations of the RMS noise at 38 MHz at zenith as a function of Galactic latitude. It is clear that classical confusion from the Galactic plane contributes greatly to the noise at low Galactic latitudes. Moreover, the fact that there is also some dependence far away from the Galactic plane also suggest that we are affected by side lobe confusion as well.

Median values for the zenith angle dependent RMS at 38, 52 and 74 MHz are shown in Figure 2.7. The inverse of the polynomial models used for the power pattern are also shown. These models fit very well to the RMS data, but deviate at large zenith angles at 38 and 52 MHz most likely due to RFI that was not removed from the data.

Derived from beam measurements, estimates for the system equivalent flux density (SEFD) of the LWA1 range from 5 to 15 kJy, for frequencies between 36 and 80 MHz (Schinzel & Polisensky, 2014). Given these values, the estimated RMS sensitivity for PASI at zenith with 5 second integrations and 75 kHz of bandwidth should range from 6 - 17 Jy, which is significantly lower than our measurements.

There are many possibilities as to this discrepancy. For instance there could be phase and amplitude errors in the uncalibrated visibilities in addition to classical and side lobe confusion from bright sources. Certainly any variation in the gain from the receiver chain could introduce errors to the measured RMS noise. This variation in gain has been measured and is mainly influenced by the temperature of the low noise amplifiers both in the shelter where the analog receivers are located, as well

as at each of the antenna stands where the pre-amplifiers are located. Therefore the analog gain is affected by both the temperature inside the shelter as well as the ambient temperature to which the pre-amplifiers are exposed. On short time scales the air conditioning units are cycling on and off introducing a measurable variation in the gain of typically around 1% (Schinzel, 2013). The seasonal variation of ambient temperatures has a much larger effect on receiver gains introducing variations of up to 10% over the course of a year, which was demonstrated by monitoring the received power of Cygnus A (Schinzel et al., 2015).

For this study, however, the seasonal effects were not removed, instead we used a spread of days across the year. When we fit the 3rd order polynomial, the seasonal variations were averaged out. Similarly since we used the same data for measuring the RMS and used the median values, there should not be any systematic offset for the measured RMS. Indeed even if there was an offset, the maximum effect would be on the order of 10%, which is much smaller than the near factor of 3 difference between our measurements and the beam measurements of Schinzel & Polisensky (2014). Therefore gain variations cannot be the reason sole behind this discrepancy.

It is interesting to note that the Stokes V images have only slightly less noise than the Stokes I images. Since there is a lack of circularly polarized sources it is expected that the confusion contribution to the noise should go away. However, the Stokes V zenith sensitivities are 40 $\pm$ 11, 27 $\pm$ 8, and 41 $\pm$ 9 Jy, at 38, 52, and 74 MHz respectively. Moreover they too display a similar Galactic longitude dependance as the Stokes I data. See Figure 2.6. As will be discussed in the next section it is unlikely that instrumental leakage could be responsible for this since the leakage into Stokes V is < 5%. One possibility is that ionospheric scintillation is adding noise to the data. As will be shown in §2.5.4, the scintillation seen in PASI is often circularly polarized. Since Schinzel & Polisensky (2014) used averaged power ratios to determine the SEFD, they would not have been sensitive to noise caused

by ionospheric scintillation, since it would average out in their observations. Further research into the RMS noise is necessary to fully understand the discrepancy between the imaged and beam formed data.

2.4.3 Polarization Leakage

PASI saves images from all four Stokes parameters, but in order to measure the true polarization of a source, characterization of the instrumental leakage into each of these modes needs to be measured. Polarization leakage into the LWA1 dipoles is a function of both azimuth and elevation. By computing the ratio of power in Stokes V to Stokes I for a bright, unpolarized source one can measure the amount of leakage in that direction. However, there are only a handful of sources bright enough to perform such measurements, and they do not cover an extremely large range of individual azimuth/elevation coordinates. Therefore, a full characterization is not possible with PASI.

Nevertheless we have measured the polarization leakage seen in the directions of Cygnus A and Cassiopeia A as they transit the sky. Figure 2.8 shows the percent leakage as a function of zenith angle for each Stokes parameter at 38 MHz. The leakage into the linear modes becomes significant at large zenith angles, but the leakage into the circular modes is hardly measurable. For all polarizations the mean leakage never rises above 15%, and for Stokes V the leakage never gets above 5% for zenith angles $< 60°$.

2.5 Transients

As mentioned in §2.1 transient searches with PASI have resulted in the detection of non-thermal radio emission from large meteors (fireballs) as well as limits on

prompt radio emission from GRBs. PASI also observes many other types of transient phenomenon, this section describes many of the non astronomical transients observed by PASI. For limits on astronomical transients see Chapter 6.

2.5.1 Image Subtraction

Image subtraction algorithms have been developed for the purpose of finding transient sources on time scales of 5 s to several minutes. From every image a running average of the previous four images is subtracted, removing all steady sources. The images are then searched for pixels which exceed the 6 σ level. The measured image noise values at zenith for subtracted images at 38, 52, and 74 MHz are 41, 19 and 35 Jy and their dependance on zenith angle is shown in Figure 2.7. For 38 MHz there does not appear to be much sensitivity improvement when using image subtraction. On the other hand, RMS noise at 52 and 74 MHz are vastly decreased when using image subtraction. The fact that the 38 MHz only slightly improves may point to ionospheric scintillation as the cause of decreased sensitivity. This effect would certainly be worse at lower frequencies and would most likely be observed on the order of several seconds. Therefore it may not get entirely removed by our image subtraction scheme.

2.5.2 Radio Frequency Interference

Depending on the frequency, time of day, and time of year PASI is subjected to varying amounts of RFI. A large fraction of the RFI seen by the LWA1 is narrow band (Obenberger and Dowell, 2011), which we can avoid by tuning TBN to protected or limited bands. Within the frequency range that PASI operates there are four protected bands designated for radio astronomy: 13.36 – 13.41, 25.55 – 25.67, 37.5 – 38.25, and 73.00 – 74.60 MHz. These protections allow for an exceptionally clean

environment at 38 and 74 MHz, however 13 and 25 MHz can at times be significantly affected by interference, presumably from out of band emission from transmitters at other frequencies.

When RFI does appear in PASI it is almost always located on the horizon and is easily removed by ignoring zenith angles greater than 60°. Moreover, RFI is almost always linearly-polarized and is narrower than PASI's 75 kHz bandwidth. Therefore, transient candidates are checked for both linear polarization as well as spectral features within the six channels. The PASI image files contain all four Stokes parameters, however to retrieve the six frequency channels, the visibilities need to be reimaged.

Along with narrow band RFI, PASI is also affected by broadband RFI from power lines and electrical equipment. These sources are easily identified because they come from fixed regions on the horizon. Situated only a few hundred meters to the north east of the array are power lines which feed the LWA1 and facilities of the VLA. These power lines create micro-sparks which emit broadband bursts and are typically only a problem during the dry windy days of spring.

2.5.3 Lightning

Long Wavelength interferometry has been used to explore the physics of lightning since the late 1970s (Warwick et al., 1979). Recently, with the advent of inexpensive time-keeping via GPS and improvements in signal processing, a number of dedicated systems such as the Lightning Mapping Array (LMA; Rison et al., 1999) have been deployed. This has clearly demonstrated the regions in clouds where lightning flashes originate, as well as illuminating in three dimensions the charge structures of clouds (Marshall et al., 2005). It has also been correlated with severe weather of all types and with radar measurements to produce a much deeper understand-

ing of the relation between lightning and its parent storm. These arrays generally make use of a small number of dipoles, which is reasonable given the strength of the emission, but leads to limitations in the imaging quality obtained. The LWA1 and the PASI back-end have collected over 40 hours of lightning observations. A special lightning mode was developed to produce rapid (200 fps) imaging with PASI in post-processing of recorded TBN data. In principle, this imaging could be extended down to the sampling rate of 100 ksps or 0.01 msec. At 5 msec time-resolution (Fig. 2.9) one can see the step-like motion of negative breakdown inside a positively charged cloud region. The entire sequence of this flash can be viewed at www.phys.unm.edu/∼lwa/lwatv/lightning/056161_000042789_00254.400_5ms.mov.

2.5.4   Ionospheric Scintillation

The transient search pipeline finds many transient sources which correspond to bright catalog sources, normally not detectable by the LWA1 because their flux densities are well below the noise floor. These events are not inherent to the sources themselves, but are thought to be caused by scintillation by the Earth's ionosphere (Obenberger et al., 2014a). The scintillation often appears in both the Stokes I and V images. See Figure 2.10. This is most likely due to the fact that the ionosphere is a magnetized plasma and therefore displays birefringence for the LHC and RHC polarizations, and therefore magnifying them separately. In addition to the amplitude scintillations we have observed position shifts in Cygnus A and Cassiopeia A of up to $\sim 10°$ in extreme conditions. These shifts along with the amplitude scintillation may be responsible for the remaining subtracted image vs beam formed sensitivity discrepancy described in §2.5.1.

Because of this scintillation, the regions within 1.5° of known bright sources are ignored in the transient search pipeline. A catalog of these sources is provided by

the VLA low frequency sky survey (VLSS; Cohen et al., 2007; Lane et al., 2012). Excluding the ~ 350 sources that are > 20 Jy at 74 MHz removes $\sim 10\%$ of the sky observable from the LWA1, but sufficiently suppresses these false detections.

Likewise the diffuse emission from the Galactic plane and north polar spur is focused by the ionosphere. Rather than excluding these regions, we increase the threshold for transient candidates to 10 σ for Galactic latitudes of -7° to +7° and 8 σ for latitudes from -10° to -7° and +7° to +10°. For the north polar spur we set a threshold of 7 σ for Galactic latitudes from +10° to +70° and Galactic longitudes from +20° to +45°. While these regions are not completely excluded the potential for discovering transients here is lessened. These regions comprise 25% of the sky observable from the LWA1.

2.6   LWA TV

LWA TV has been viewed in numerous countries, and recently we have been receiving ~ 400 unique IP hits per month. While most of these hits are presumably members of the public at large, we know of several cases in which LWA TV has been used during astronomy lectures. Dedicated[8] monitors displaying LWA TV have been installed at the VLA Visitor Center and in the lobby of the Physics and Astronomy department at UNM.

LWA TV has also been used to localize and mitigate interference at the site. In one instance some of the fluorescent light fixtures in the antenna assembly building of the VLA were found to be emitting by noticing that they switched on at the start of the work day and switched off at the end. Several times now we have used LWA TV to localize and mitigate power line noise (recognizable by its presence at the

---

[8]To learn how to set up a dedicated monitor for viewing LWA TV, please visit http://fornax.phys.unm.edu/lwa/trac/wiki/EPO

horizon and its extent) working with the Socorro Electric Cooperative.

2.7 Conclusions

This chapter has described the system design of PASI, a backend correlator of the LWA1 telescope. This chapter also described the flux calibration and sensitivity measurements of the LWA1 telescope using image data and showed that the ionosphere may be influencing our measurements of the true sensitivity. We also performed the first characterization of the polarization leakage of the instrument.

PASI has been used to characterized radio transient foregrounds such as emission from fireballs and ionospheric scintillation, which will need to be taken into account in future transient studies with the LWA1 as well as other low frequency telescopes. It also offers the potential for future studies of the ionosphere, lightning, and meteors.

2.8 Acknowledgments

PASI system design

Figure 2.1: A block diagram showing the PASI components and other relevant LWA systems. Dashed lines indicate command and status information pathways and are carried by standard Ethernet connections. Solid lines indicate signal or high-bandwidth data pathways and are carried by 10 GbE connections outside of PASI and Infiniband connections or shared memory within it. Grey boxes represent LWA1 hardware systems, and blue boxes represent components of PasiFx. A description of the acronyms are as follows: DR (Data Recorder), DP (Digital Processor), ARX (Analog Receiver), DRSU (Data Recorder Storage Unit), and TBN (Transient Buffer Narrow band)
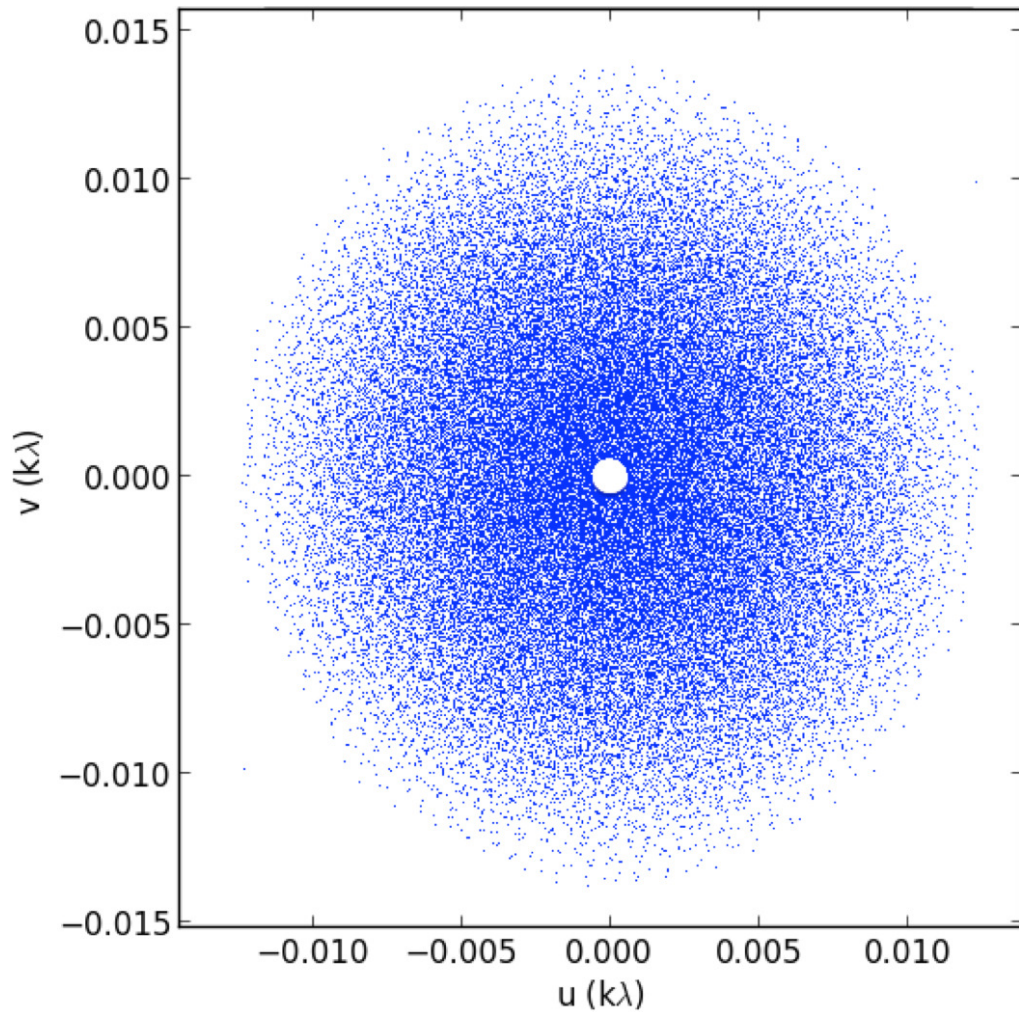
Figure 2.2: A plot of the (u, v) coverage of the main core of the LWA1 at 38 MHz, u and v are in units of kilo wavelength. The inner hole is a result of the required minimum separation between dipoles of 5 meters (Kogan & Cohen, 2009).
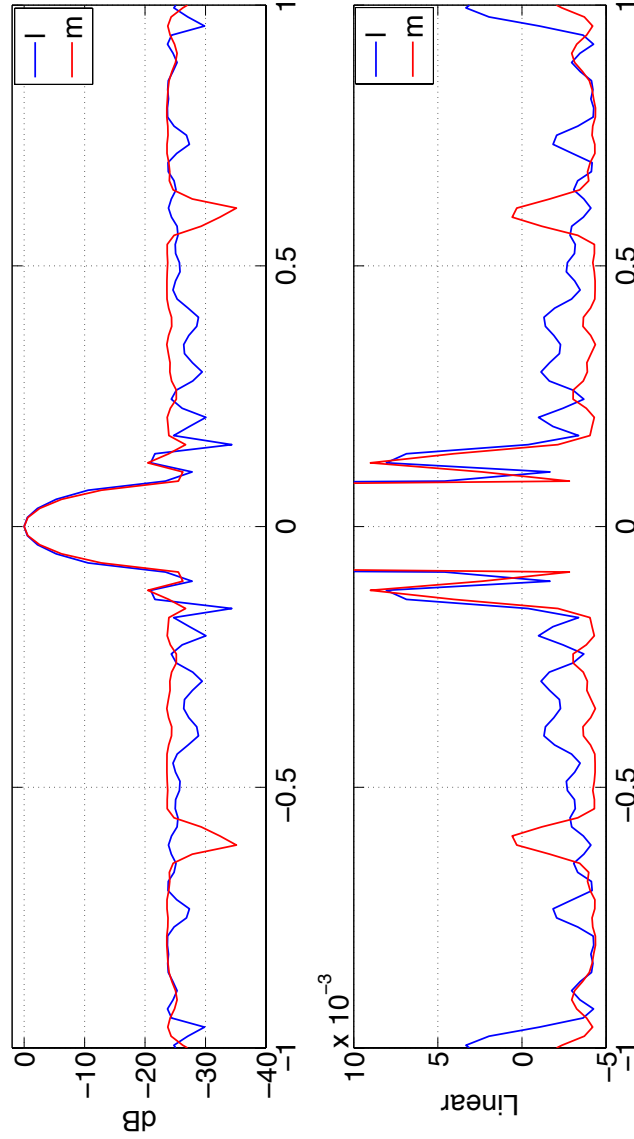
Figure 2.3: Perpendicular (l, m) slices of the normalized, modeled point spread function taken from the (u, v) snapshot at 38 MHz in Figure 2.2. The slices are shown in both absolute value dB (top) and linear (bottom) scaling. The units of l and m are directional cosines covering the full 180° from horizon to horizon, -1 to 1. The red line covers all l where $m = 0$. Likewise the blue line covers all m where $l = 0$.
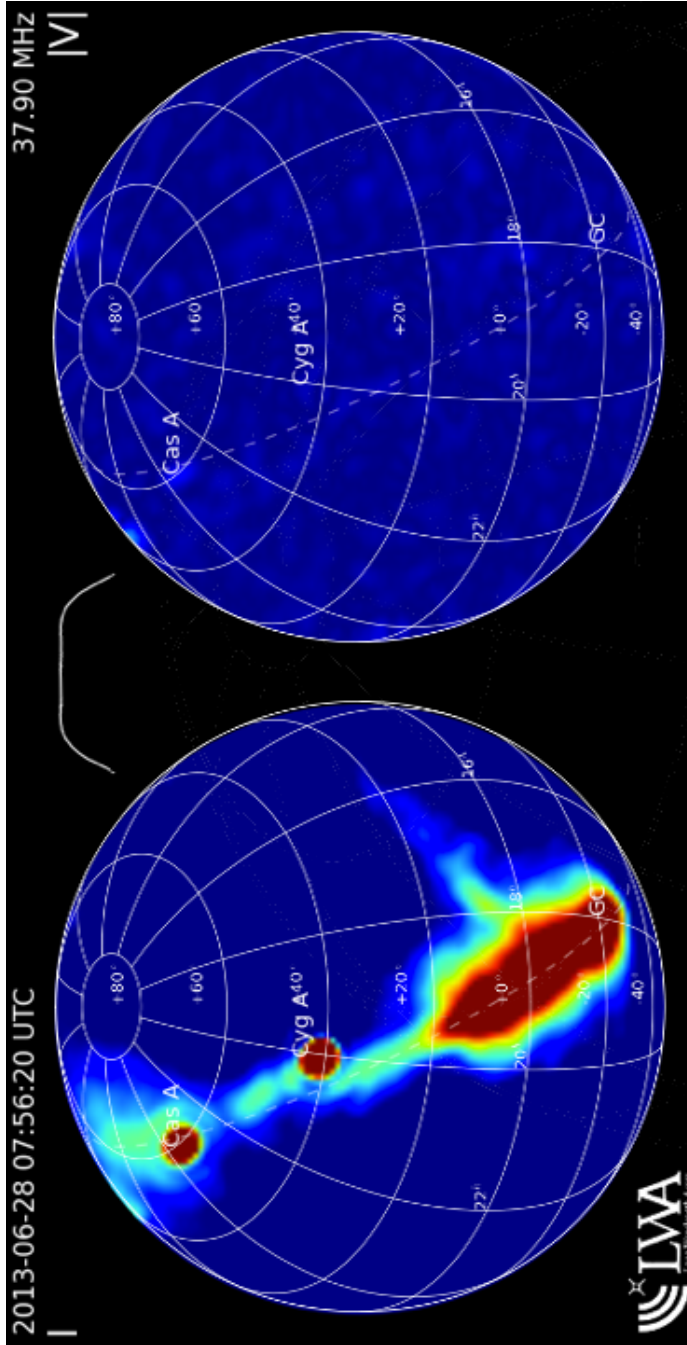
Figure 2.4: Example of a PASI 5 second snapshot centered at 37.9 MHz as displayed on the LWA-TV website, overlaid with a gird showing equatorial coordinates. The Stokes I image is shown on the left with a dynamic range of ∼ 300. The Stokes V image is shown on the right, with values shown as the absolute value so that both left hand circular (LHC) and right hand circular (RHC) are shown as positive. These images show the full 2π sr of sky above the LWA1. The Galactic plane, Galactic Center (GC), Cygnus A (Cyg A), and Cassiopeia A (Cas A) can all be seen in the Stokes I image. The 256 channel averaged spectrum is shown in the top center of the figure.
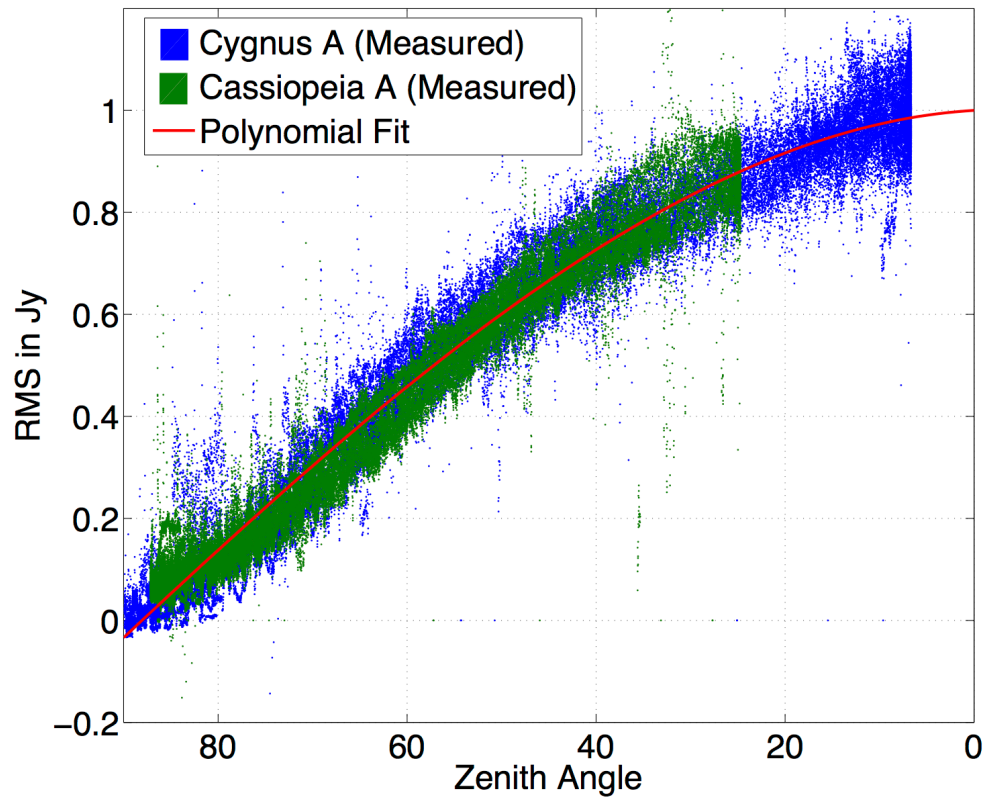
Figure 2.5: Normalized fluxes for Cygnus A (Blue) and Cassiopeia A (Green) at 38 MHz, taken as the sources transited on seven separate days between June 2013 and June 2014. The polynomial model is shown in red.
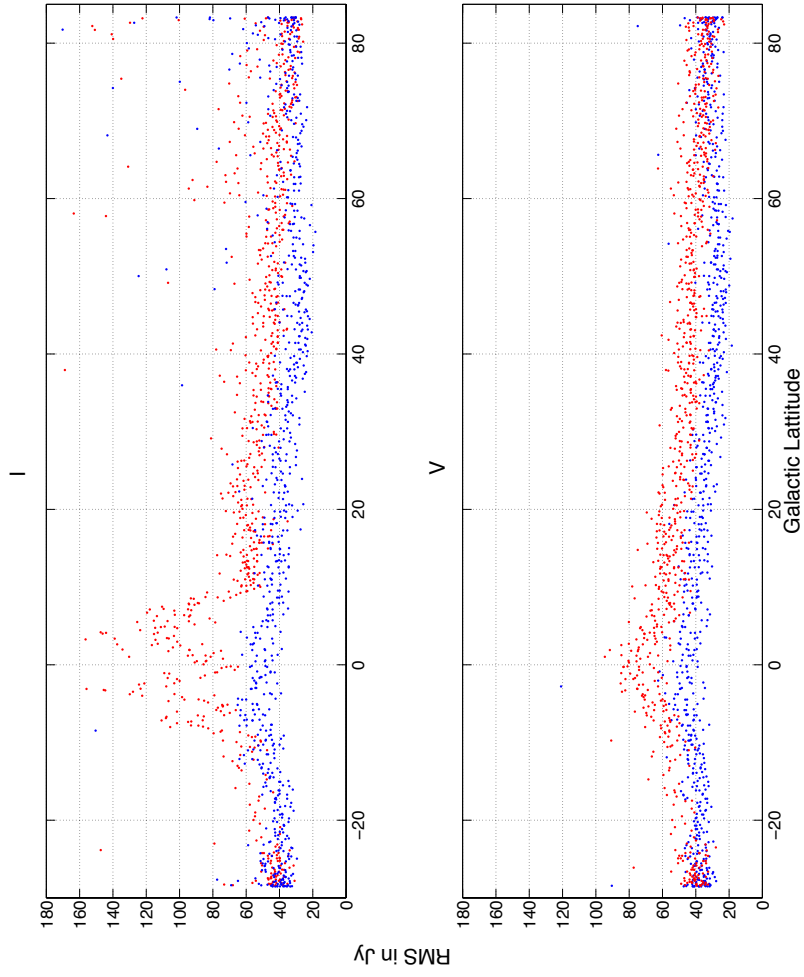
Figure 2.6: Calculations of the RMS at 38 MHz as a function of Galactic latitude for both Stokes I and V. The red dots correspond to Galactic longitudes $< 120°$ and the blue dots correspond to Galactic longitudes $> 120°$.
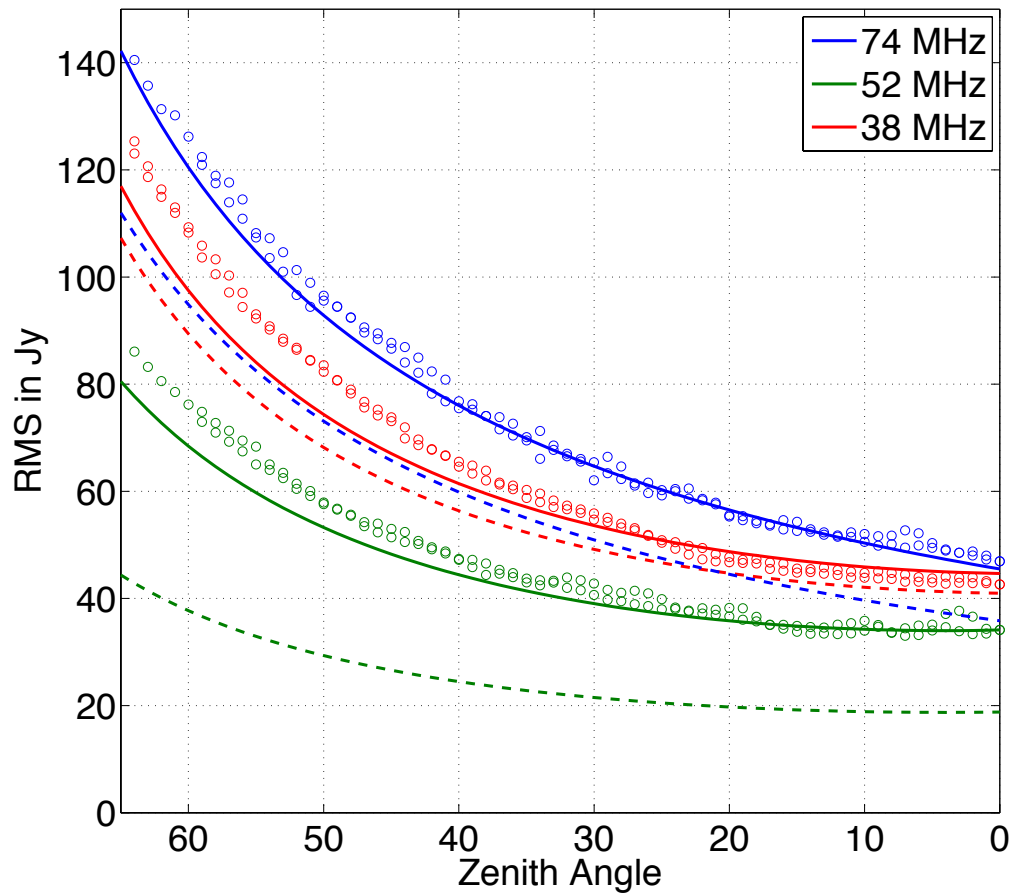
Figure 2.7: Shown here are the median values for the RMS noise for regular PASI images (open circles), the inverted polynomial model (solid lines), and the RMS of the subtracted images (dashed lines) for 38, 52, and 74 MHz.
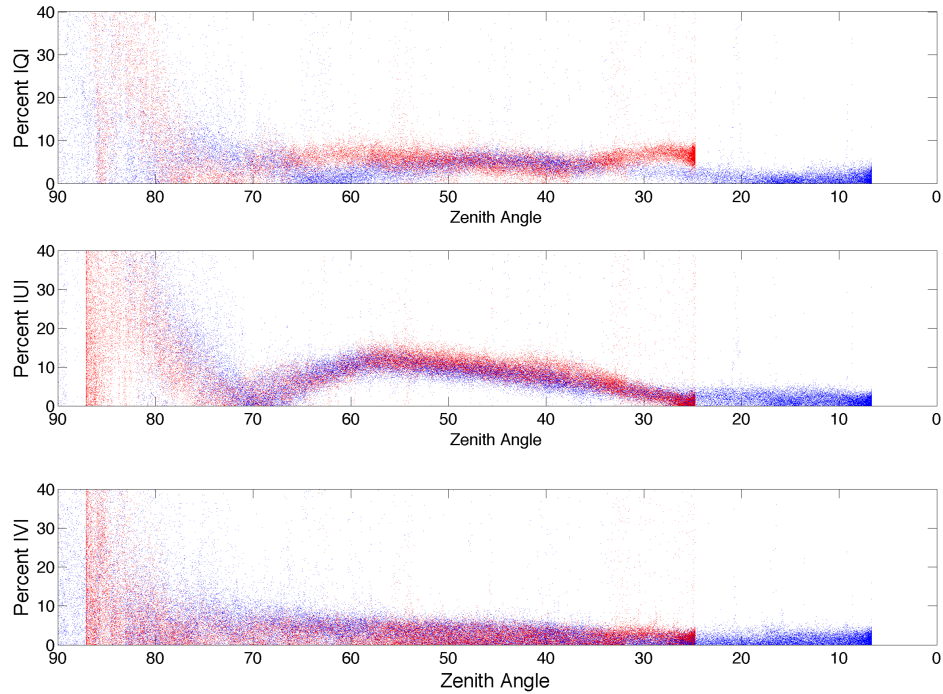
Figure 2.8: The measured magnitudes of polarization in Stokes Q, U, and V for unpolarized sources Cygnus A (Blue) and Cassiopeia A (Red), showing the amount of leakage into each Stokes parameter as a function of zenith angle. These data were taken from four different days at 38 MHz, one from each season of the year, showing no significant difference from one season to the next. While these two sources alone do not give a full picture of the azimuthal/zenith angle dependence of the polarization leakage, as plotted they do provide an estimate of the expected leakage as a function of zenith angle.
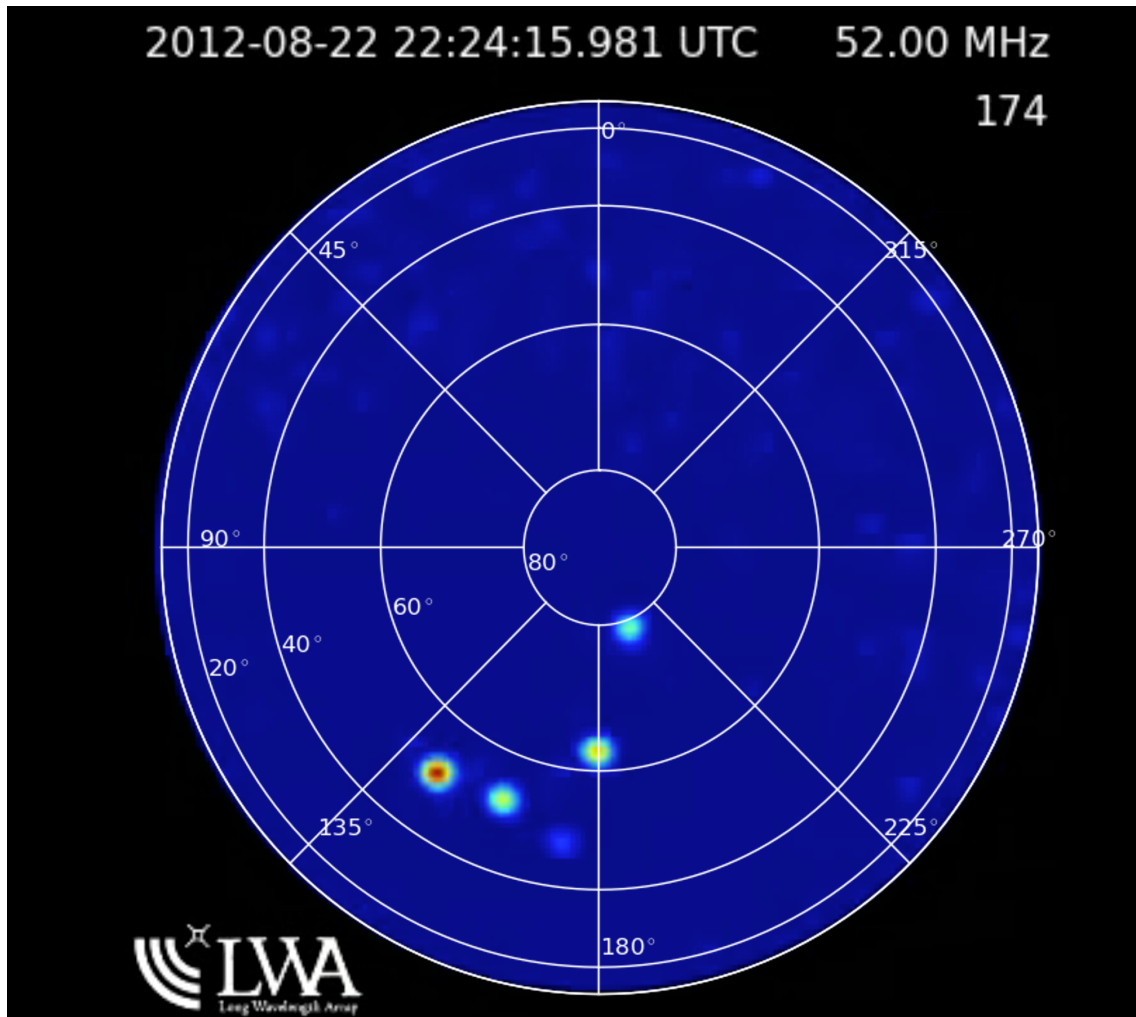
Figure 2.9: A 5 ms snapshot from PASI's lightning mode showing the step-like motion of the negative breakdown within a positively charged cloud region. Overlaid is the a grid showing Horizontal coordinates.
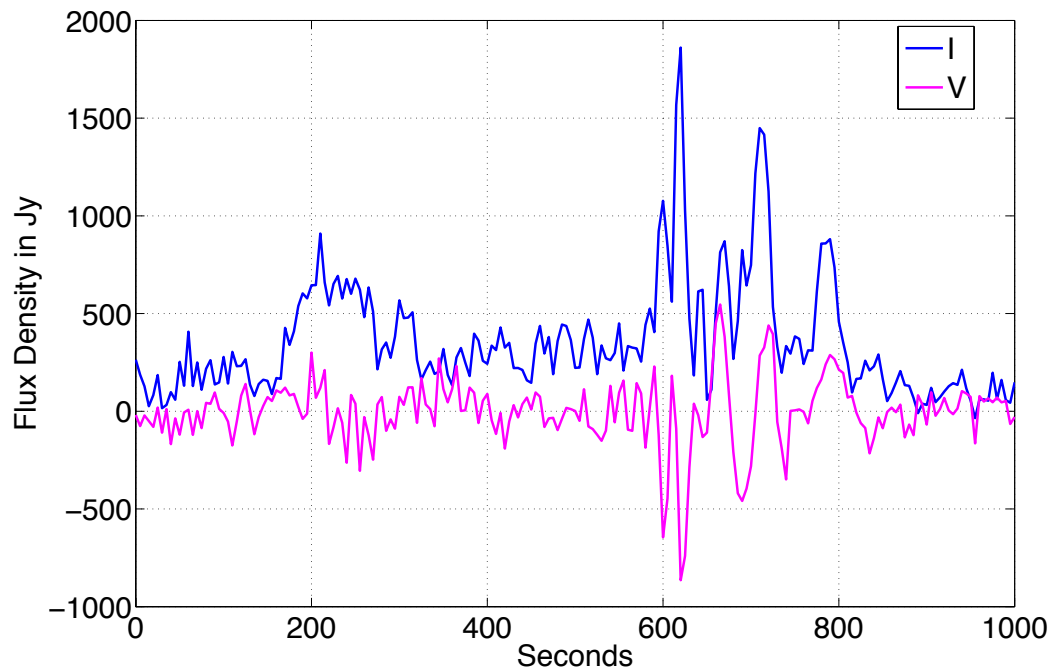
Figure 2.10: A light curve showing the scintillation of 3C254, a 60 Jy source at 38 MHz (Kellermann et al., 1969). The scintillation can be seen in Stokes V, where positive values correspond to RHC and negative values correspond to LHC. This cannot be due to instrumental leakage, which is < 5% and does not rapidly switch between LHC and RHC.

Chapter 3

A Search for Prompt Emission from GRBs

Abstract: As a backend to the first station of the Long Wavelength Array (LWA1) the Prototype All Sky Imager (PASI) has been imaging the sky > -26° declination during 34 Gamma Ray Bursts (GRBs) between January 2012 and May 2013. Using this data we were able to put the most stringent limits to date on prompt low frequency emission from GRBs. While our limits depend on the zenith angle of the observed GRB, we estimate a 1σ RMS sensitivity of 47, 34 and 45 Jy for 5 second integrations at 37.9, 52.0, and 74.0 MHz at zenith. These limits are relevant for pulses ≥ 5 s and are limited by dispersion smearing. For pulses of length 5 s we are limited to dispersion measures (DMs) ≤ 220, 570, and 1,600 pc cm^{-3} for the frequencies above. For pulses lasting longer than 5s, the DM limits increase linearly with the duration of the pulse. We also report two interesting transients, which are, as of yet, of unknown origin, and are not coincident with any known GRBs.

3.1   Introduction

Gamma ray bursts (GRBs) come in two flavors; short duration bursts of hard gamma rays (Berger, 2014) and long duration bursts of softer gamma rays (Woosley & Bloom, 2006). Both varieties are thought to occur from the violent formation of black holes. Short bursts most likely occur when two neutron stars collide forming a black hole surrounded by an accreting debris disk. Long bursts most likely occur when the core of a massive star collapses directly into a black hole and the outer shells of the star are accreted onto the black hole. In both the short and long burst scenarios, the accreting back hole forms two narrow, symmetric relativistic jests, which produce beamed gamma rays along the jet direction. If an observer's line of sight is directly down a jet, a gamma ray burst is observed.

Since the discovery of GRBs by Klebesadel et al. (1973) there have been several groups to propose mechanisms capable of producing prompt low frequency (<100 MHz) radio emission observable from Earth. Usov & Katz (2000) suggested that low frequency radiation could be created by oscillations in the current sheath that separates a strongly magnetized jet and the surrounding ambient plasma. This emission would peak at 1 MHz and drop off following a power law at higher frequencies. The bulk of the emission lies below the ionospheric cutoff of about 10 MHz, but the high frequency tail of this might extend up to frequencies observable by ground based telescopes. The flux density of the high frequency tail is approximated with a power law $\propto \nu^{-1.6}$. As an example they provide a best case estimate of $\sim 10^2$ Jy at 30 MHz.

Sagiv & Waxman (2002) also predict low frequency emission to occur in the early stages of the afterglow (10s after the GRB). In this scenario a strong synchrotron maser condition is created at frequencies below 200 MHz, due to an excess of low

energy electrons. The excess is created by a build up of injected electrons that cool to low energies through synchrotron radiation. The effect is amplified when the jet propagates into a medium denser than the ISM. Such a dense environment would exist around high mass Wolf-Rayet stars, which are thought to be the progenitors of long duration GRBs.

While no prompt low frequency emission has yet been detected, a future detection would yield a number of constraints on the parameters of GRBs. The dispersion measure (DM) of prompt radio emission would allow estimates of the physical conditions of the region immediately surrounding nearby $(z \lesssim 0.5)$[1] GRBs, telling us about the environment in which GRB progenitors are formed. For more distant GRBs the DM would be dominated by the Intergalactic Medium (IGM), thus giving a measurement of the number of baryons in the universe (Ginzburg, 1973). For extremely distant $(z > 6)$ GRBs a dispersion measure could also act as a probe of the reionization history (Ioka, 2003).

Over the past three decades there have been many searches for prompt, low frequency GRB emission (Baird et al., 1975; Dessenne et al., 1996; Koranyi et al., 1995; Benz & Paesold, 1998; Balsano, 1998; Morales et al., 2005; Bannister et al., 2012). Of these studies, 2 have been below 100 MHz. Benz & Paesold (1998) covered the range from 40 - 1000 MHz, had a RMS sensitivity of $\sim 10^5$ Jy, and observed during 7 GRBs between February of 1992 and March of 1994. Balsano (1998) covered 72.8 - 74.7 MHz, observed 32 GRBs between September of 1997 and March of 1998, and had a wide range in root mean square (RMS) sensitivities for each GRB. The best limit reported in Balsano (1998) was $\sim$200 Jy for 50 ms integrations. Both of these studies used BATSE triggers, which had a position uncertainty typically

---

[1]A redshift of 0.5 is chosen because above this point the DM contribution from the intergalactic medium would be roughly equal to the maximum contribution from a galaxy similar to our own (Ioka, 2003). However if the DM of the host galaxy is larger than that of our own, "nearby" would include larger redshifts.

around a few degrees. Morales et al. (2005) reported on a planned study centered at 30 MHz.

In this chapter we present a search for prompt low frequency emission from 34 GRBs using the all-sky imaging capabilities of the Prototype All Sky Imager (PASI), a backend to the first station of the Long Wavelength Array (LWA1). While our objective was to find or place limits on prompt emission from GRBs, we also conducted a search for generic transients occurring during our observations but located elsewhere in the sky. In §3.2 we describe the NASA GCN/TAN (Gamma- ray Coordinates Network / Transient Astronomy Network) and how we made use of it for our observations, in §3.3 we discuss how dispersion would effect prompt emission from GRBs, in §3.4 we discuss our data, analysis and our results, in §3.5 we describe our search for generic transients and our results, and §3.6 is a discussion of our findings.

3.2 GCN Trigger Archive

Currently we use the NASA GCN/TAN (Gamma-ray Coordinates Network / Transient Astronomy Network) trigger archive[2] (Barthelmy et al., 1995) from Swift (Burrows et al., 2005; Barthelmy et al., 2005), Fermi GBM (Gamma-ray Burst Monitor,Meegan et al., 2009; Briggs et al., 2009), and MAXI (Monitor of All-sky X-ray Image,Matsuoka et al., 2009). MAXI provides the fewest triggers with about 1 GRB per month, and has 1 arcmin resolution. Swift is more favorable with 2 GRBs per week and arcsec resolution with the XRT (X-Ray Telescope) and UVOT (UV/Optical Telescope) and arcmin with BAT (Burst Alert Telescope) covering the electromagnetic spectrum from optical to hard X-rays. Fermi GBM is the most prolific with a large field of view enabling the detection of 20 GRBs per month, but only a position accuracy of 1-10 degrees at best.

---

[2]http://gcn.gsfc.nasa.gov

For this study we have used the GCN GRB triggers that occurred during PASI operation between January 1 2012 and May 25 2013. Furthermore we excluded triggers with initial zenith angles greater than 60° (with 6 exceptions[3] in the eastern sky) and those that occurred during periods of exceptionally high RFI.

3.3   Delay and Dispersion

A prompt pulse is delayed and stretched out in time at low frequencies. A dispersion measure, DM, is proportional to the number of electrons between an observer and a source. For a pulse of constant frequency (expansion is negligible) the delay time of a pulse of frequency ν with DM is given by:

$$\tau(\nu) = k_{DM} \times DM \times \frac{1}{\nu^2}, \tag{3.1}$$

where the dispersion constant $k_{DM} = e^2/(2\pi m_e c) = 4149$ MHz^2 pc^{-1} cm^3 s. The total dispersion measure can be broken up into three regions, our own galaxy DM$_{Gal}$ the intergalactic medium DM$_{IGM}$, and the GRB's host galaxy DM$_{host}$. The DM of our galaxy varies based on the orientation to the plane, and ranges from DM$_{Gal}^{min} \sim 30$ pc cm^{-3} to DM$_{Gal}^{max} \sim 10^3$ pc cm^{-3} (Taylor & Cordes, 1993; Nordgren et al., 1992). Using Equation 3.1 this range of DM correspond to a range in time delay of 46 s to 25 min at 52 MHz.

The DM$_{IGM}$ depends on the number of electrons in the intergalactic medium between us and the GRB and is therefore dependent on the redshift of the galaxy. However, because of the expansion of the universe, the frequency of the radiation

---

[3]To account for possible unknown, intrinsic delays, these 6 triggers were selected to provide a sample that would be at smaller zenith angles several hours after the γ-ray emission arrived.

emitted in our direction will decrease. Thus a generalization of equation 3.1 must be used to calculate the delay caused by DM_{IGM}. Ioka (2003) estimates the redshift dependent DM_{IGM} would be:

$$DM_{IGM} = \frac{3cH_0\Omega_b}{8\pi Gm_p} \int_0^z \frac{(1+z)dz}{[\Omega_m(1+z)^3 + \Omega_\Lambda]^{1/2}}. \tag{3.2}$$

This cosmological DM takes into account the redshift in frequency over time. Therefore combining Equations 3.1 and 3.2 the time delay of an emitted photon observed to be at frequency, ν_{ob}, is given by:

$$\tau(\nu) = \frac{k_{DM}3cH_0\Omega_b}{\nu_{ob}^2 8\pi Gm_p} \int_0^z \frac{(1+z)dz}{[\Omega_m(1+z)^3 + \Omega_\Lambda]^{1/2}}, \tag{3.3}$$

with $(\Omega_m, \Omega_\Lambda, \Omega_b, h) = (0.3175, 0.6825, 0.04810, 0.6711)$, (Plank Collaboration, 2013), the values for the time delay, $\tau(\nu_{ob})$, due to the intergalactic medium, are shown in Figure 3.1. DM_{host} is the most difficult quantity to estimate, and may dominate the total DM in some cases. Examining at Equations 3.1 and 3.3 it is easy to see that at higher redshifts the DM of a host galaxy similar to ours would play a very small role in the delay. However if the GRB progenitors dwell in dense star forming regions, such as the case may be for some long GRBs, then a very small optical depth may make it difficult to detect any signal at all.

Since we do not dedisperse the bursts, we are subject to dispersion smearing across our entire 75 kHz band. In seconds the dispersion smearing time is given by:

$$\tau_{smear} = 8242 \times DM \times \nu^{-3} \times \Delta\nu, \tag{3.4}$$

where ν is the center frequency in MHz and $\Delta\nu$ is the bandwidth in MHz. Therefore bursts ≤ 5 seconds would become smeared out across our band to at least 1.5 times their duration at $DMs \geq 220$, 570, and 1,600 pc cm^{-3} at 37.9, 52.0, and 74.0 MHz. However, if the bursts are of longer duration, then dispersion smearing has less of

an effect on the sensitivity to those bursts, and we can see out to larger DMs. For instance a burst of 30 seconds would be smeared out to 1.5 times their duration at DMs = 1,300, 3,400, and 9,800 pc cm^{-3} at those frequencies.

3.4 Data, Analysis, and Results

When given a set of GRB coordinates, a date, and time, we used our archived visibility data to image the entire sky and track the GRB's position. Using Figure 3.1 as a reference for expected DM, we analyze the 2 hours after the prompt γ-ray emission for observations at 74.0 MHz, 3 hours for 52.0 MHz and 4 hours for 38.0 MHz. These values allow enough time for burst coming from $z < 4$. Tracking of the source is accomplished by mapping the images onto an right ascension (RA) and declination (DEC) coordinate system and selecting the pixels of one beam around the source location. We can then analyze the light curve of that region and look for detections.

From our data, there have not been any significant ($> 5\sigma$) transient events corresponding spatially and temporally to any GRB triggers. However we can provide limits to the peak intensity of a transient.

Given the zenith angle of the GRB at the time the γ-ray emission arrives, we estimated the 1 σ limit with the RMS sensitivity model described in §2.4.2. See Table 3.1 for our list of GRBs and estimated limits[4]. Since we are using only the dirty images from PASI, which undergo neither a phase self calibration nor deconvolution.

---

[4]While there were ∼500 GRBs detected by GCN/TAN telescopes during the 17 months of our study, PASI only observes 1/4 of the total sphere. Moreover PASI was only fully operating during about 1/3 of this time. Also there were a handful of events which occurred during periods of high RFI or solar activity, which prevented us from making reliable limits. This is why we only have 34 GRB observations.

These limits reflect the RMS noise for 5 second integrations. If a pulse was shorter than 10 seconds, our signal to noise (S/N) would be decreased by the ratio of time spent in any one time bin to the size of the bin itself. For instance consider a 7 second, 1000 Jy pulse, that occurred at zenith at 38 MHz and spent 3 seconds in the first bin and 4 seconds in the second. In the second bin the observed flux density would be $1000 \times (0.8)$ Jy. Therefore our S/N would decrease by a factor of 0.8.

3.5 Interesting Transients Not Associated with GRBs

Throughout the course of searching for prompt radio emission from GRBs we also searched our data for generic transients in our field of view. We automated our search using image subtraction methods, which remove all of the continuous sources in the sky, and provide images with a gaussian distribution of pixel values centered at zero. Since this method adds noise but no signal the S/N inherently increases by $\sqrt{2}$, but allows us to statistically find changes on the order of 10 s. To do this we subtract the third previous image from every image and set a threshold of 6σ for pixel values. Below 6σ the number of events detected displayed gaussian behavior as expected with an additional bump at 5σ from false detections from RFI. Above 6σ we found 18 events at 37.9 MHz, 7 at 52.0 MHz, and 2 at 74.0 MHz. Except for 1 event at 37.9 MHz and 2 events at 52.0 MHz, nearly all of these events were immediately identified as RFI.

The two events at 52.0 MHz each lasted for only one integration (5s) and appear to be broadband across the 75 kHz. However, upon further investigation these events were found to have significant linear polarization, which indicates that they were most likely reflected man-made RFI, possibly from the ionosphere or from ionized trails

left by meteors.

The 37.9 MHz event, however, was a Fast Rise / Exponential Decay (FRED) transient candidate. The event occurred on 2012 Oct. 24 (121024) at 08:37:39 UT, lasted for 75 seconds, had an RA and DEC of 04h 14m 00s +76d 54m 00s with an estimated error of $\sim 1.5°$. The light curve of the transient displayed a rise time of ~ 15 s and decay of ~ 60 s (Fig. 3.2). At peak intensity, this source appears to be ~ 2.4 kJy, and is constant across the 75 kHz band. However upon examining all 4 Stokes parameters, there is a slight bump of linear (-U) and left hand circular (-V) as shown in Figure 3.2. The exact percentage of polarization is difficult to quantify since both the -U and -V components each last for one integration and are both $< 5\sigma$. When compared to the entire 75 s burst the -U and -V components are $5 \pm 1\%$ and $4 \pm 1\%$. While this polarization may be real, instrumental leakage is very likely the cause. The leakage into the three Stokes polarizations on the LWA1 is a function of a sources position on the sky but has not yet been characterized. As a reference we measured the leakage of Cassiopeia A, an unpolarized source at 38 MHz, during the same period the transient was detected. During this time we measured -Q, U, and V leakages of $\sim 3\%$, 8%, and 3%. Cassiopeia A was at approximately the same zenith angle as the transient.

A second event occurred on 2012 Nov. 18 (121118) at 09:53:40 UT, lasted for 100 seconds, had an RA and DEC of 07h 22m 24s +41d 18m 00s, and was observed at 29.9 MHz. The light curve shows similar properties to the 121024 event with a rise time of ~ 25 s and decay time of ~ 75 s, a maximum flux density of 3.2 kJy, and is also constant across the band. However during this event there were no detectable polarized components (Fig. 3.2).

Examining the 75 kHz bandwidths we see no signs of any dispersion for either event. However we are able to limit the DMs of the 121024 and 121118 events to be approximately ≤ 450 and ≤ 250 pc cm^{-3}.

Using the NASA/IPAC Extragalactic Database[5] we found 5 sources above 20 Jy at 38 MHz within 3°, twice our estimated position error, of the 121024 event and none above 20 Jy at 38 MHz within 3° of the 121118 event. All of the 121024 sources were part of the revised source list of the Rees 38-MHz (8C) survey (Hales et al., 1995; Rees, 1990), and no additional sources were found using that catalog. Also there were no additional sources above 7 Jy at 74 MHz found using the VLSS within 3° of either event (Cohen et al., 2007).

Table 3.2 lists the sources near the 121024 event. It is possible for any one of these 5 sources to be focused by the ionosphere and temporarily increase in brightness. In fact this is a regular occurrence with sources in our field of view. There will often be periods when several sources on the sky will fluctuate up to 15 times their normal brightness. The effect usually covers the entire sky, in that many sources across the sky will fluctuate (scintillate) for up to several hours. This is likely caused by turbulence in the ionosphere; similar variation has been observed by other instruments at the same frequency (Bezrodny et al., 2008).

At these times of high scintillation, sources that lie below our detectable limit will sometimes be magnified above our threshold and appear for a short period of time. While the vast majority of events occur for sources above 100 Jy, there have been 4 at lower flux densities in the 112 hours of observations at 37.9 MHz data reported in this chapter. The typical shape for a light curve of one of these events is a fast rise, fast decay, often lasting for just one integration. Occasionally the source will stay bright for up to a minute, displaying several peaks as it dims and brightens. Figure 3.3 shows two typical light curves from brightening events. The first is 3C249, which is the dimmest object (37 Jy at 38 MHz) to be magnified above 6σ in the data reported in this chapter. The second is 3C230 (76 Jy at 38 MHz), which displayed a brightening event lasting ~ 75s, during which it peaked several times.

---

[5]http://ned.ipac.caltech.edu

There are several reasons why we believe the 121024 event was not simply one of these focusing events. The first is that this would be one of the strongest focusing events we have seen that is a factor of ~ 60 if it is 8C 0422+770 and ~ 120 if it is 8C 0415+763. The second is that during the hours before and after, the other sources in the sky were scintillating only slightly. Finally the light curve is very similar to the light curve of the 121118 event for which there is no corresponding bright sources and is dissimilar to a light curve of a typical scintillation event. Therefore it is our belief that these events are not ionospheric focusing of objects just below our sensitivity limit.

Many astrophysical sources have been theorized to produce low frequency transient emission. Possible sources include neutron star mergers (Hansen & Lyutikov, 2001; Yancey et al., 2015), primordial black holes (Rees, 1977; Blandford, 1977; Kavic et al., 2008), and flaring stars (Loeb et al., 2013). However a highly likely RFI candidate is a meteor reflection. The ionized trails of meteors have long been known to reflect man-made RFI. In particular there is a population of long-duration meteor reflections which last up to several minutes and have similar temporal evolution to these two events (Bourdillon et al., 2005). These meteor reflections tend to be linearly polarized, a property the 121118 event is lacking and the 121024 displays no more than what we expect from leakage.

3.6 Discussion

We have carried out a search for prompt low frequency radio emission from 34 GRBs at 37.9, 52.0, and 74.0 MHz. In this search we found no burst-like emission but have placed limits at these frequencies. Our 1σ limits for each frequency are listed in Table 3.1 and range from ~ 35 to 200 Jy, for ≥ 5 second bursts. The range of DMs that we are sensitive to depends on the duration of the burst. For 5 second bursts

we could see to a maximum of 220, 570, and 1,600 pc cm^{-3} for 37.9, 52.0 and 74.0 MHz.

While these limits do not disprove any of the possible emission mechanisms discussed in the introduction of this chapter these are the most stringent to this date. In the future we do plan to improve our sensitivity by using targeted beam formed observations, which have greater bandwidth and are therefore more sensitive. It should be noted that temporal broadening due to scattering from an inhomogeneous medium may be the limiting factor if indeed GRBs produce low frequency radio emission.

In this chapter we also report two transient events, 121024 and 121118, at 37.9 and 29.9 MHz respectively, that lasted for 75 and 100 seconds. We limit their DMs to be approximately ≤ 450 and ≤ 250 pc cm^{-3}.

If it is true that we should see one FRED transient for every ≤ 115 hours of observation at 37.9 MHz then a full analysis on the 1000s of hours of data PASI has collected at this frequency should yield several more. Chapters 4 and 6 address the results of such a large scale search.

3.7 Acknowledgements

Chapter 3. A Search for Prompt Emission from GRBs

Part of this research was conducted at the Jet Propulsion Laboratory, California Institute of Technology, under contract to NASA
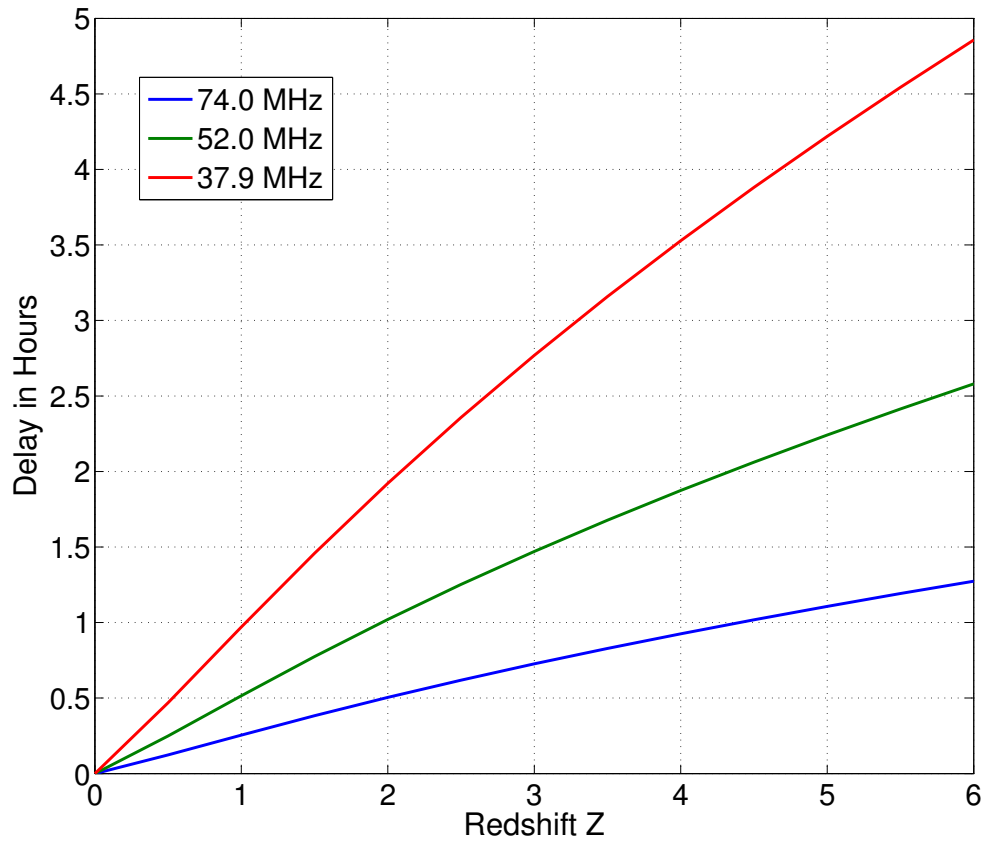
Figure 3.1: Time delay due to the IGM dispersion for 37.9, 52.0 and 74.0 MHz, as a function of redshift. These are numerical calculations of Equation 3.3 derived from Equation 3.2 of Ioka (2003).

Table 3.1: GRBs and their limits.

Telescope	Trigger #	Name	Frequency (MHz)	1σ RMS (Jy)
Fermi	347464837	120105584	74.0	49
Fermi	347831163	120109824	74.0	64
Fermi	348250807	120114681	74.0	85
Swift	519211	120403A	74.0	85
Fermi	356223561	120415958	74.0	92
Fermi	356646915	120420858	74.0	116
Fermi	357141744	120426585	74.0	109
Fermi	357182249	120427054	74.0	180
Fermi	358605842	120513531	74.0	165
Fermi	359894162	120528442	74.0	61
Fermi	360039223	120530121	74.0	80
Fermi	360586337	120605453	74.0	95
Fermi	364008918	120715066	52.0	50
Fermi	364139465	120716577	52.0	72
Fermi	364151106	120716712	52.0	136
Swift	529095	120729A	52.0	35
Fermi	367031309	120819048	52.0	53
Fermi	372317712	121019233	37.9	62
Fermi	374504566	121113544	37.9	194
Fermi	374804740	121117018	37.9	56
Fermi	375534890	121125469	37.9	66
Swift	539866	121128A	37.9	130
Swift	540964	121209A	37.9	76
Swift	544784	130102A	37.9	60
Fermi	379209148	130106995	37.9	95
Fermi	381843217	130206482	37.9	78
Swift	548760	130215A	37.9	54
Fermi	383388785	130224370	37.9	56
Swift	552063	130327A	37.9	53
Fermi	387054766	130407800	37.9	52
Swift	553918	130419A	37.9	84
Swift	554620	130427A	37.9	70
MAXI	418849999	N/A	37.9	59
Swift	556344	130521A	37.9	58
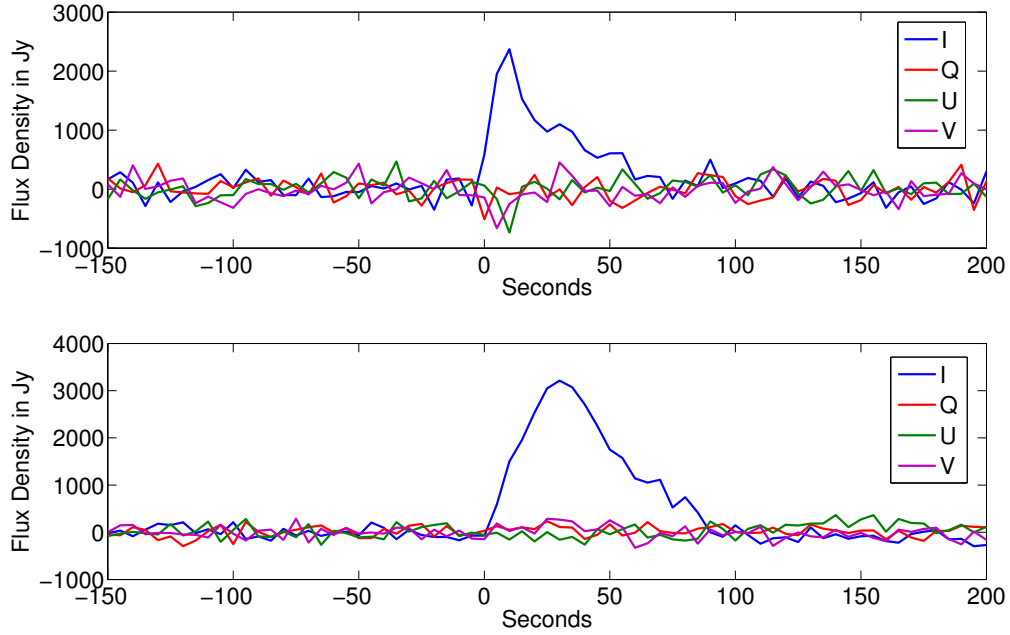
Figure 3.2: (Top) Light curve of the 121024 event, at 37.9 MHz. The -U burst is at 10 s and the -V burst is at 5 s. (Bottom) Light curve of the 121118 event, at 29.9 MHz.

Table 3.2: Sources above 20 Jy within 3° of the 121024 event

Name	RA	DEC	S_{int} (Jy)	Dist
8C 0422+770	04h 29m 19s	+77d 09m 13s	42.8	0.9°
8C 0357+747	04h 03m 15s	+74d 55m 58s	35.1	2.1°
8C 0407+747	04h 13m 16s	+74d 51m 05s	28.5	2.0°
8C 0343+749	03h 49m 52s	+75d 09m 01s	22.0	2.3°
8C 0415+763	04h 22m 06s	+76d 27m 05s	21.8	0.6°
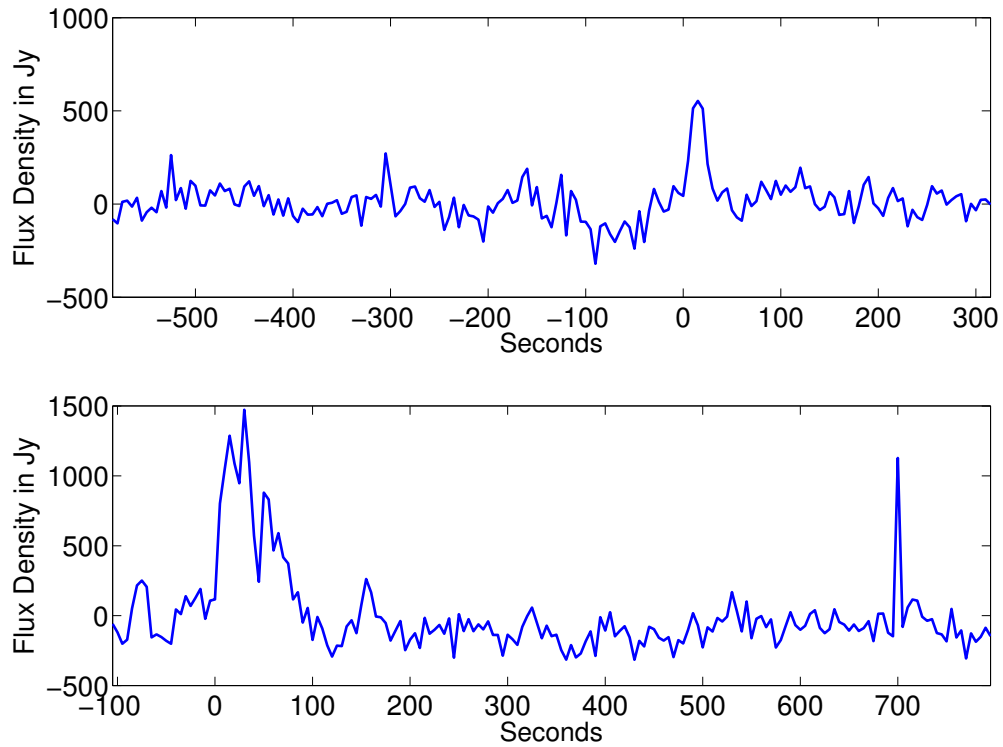
Figure 3.3: Light curves 3C249 (Top) and 3C230 (Bottom). Each source has been magnified far above their actual flux densities (37 and 76 Jy) due to ionospheric focusing. 3C230 shows as second brightening lasting for only one 5 second integration 700 seconds after the initial brightening.

Chapter 4

Detection of Radio Emission from Firebalis

Abstract: We present the findings from the Prototype All-Sky Imager (PASI), a backend correlator of the first station of the Long Wavelength Array (LWA1), which has recorded over 11,000 hours of all-sky images at frequencies between 25 and 75 MHz. In a search of this data for radio transients, we have found 49 long (10s of seconds) duration transients. Ten of these transients correlate both spatially and temporally with large meteors (fireballs), and their signatures suggest that fireballs emit a previously undiscovered low frequency, non-thermal pulse. This emission provides a new probe into the physics of meteors and identifies a new form of naturally occurring radio transient foreground.

4.1   Introduction

A recent study with the LWA1 yielded two promising transients below 40 MHz (Obenberger et al., 2014a). This search was focused on placing limits on prompt emission from gamma ray bursts and therefore only the times shortly after the occurrence of GRBs were searched. In total < 200 hours of data were analyzed. The two detected transients were not associated with GRBs, but at the time of publication their origins were unknown. However the need to conduct further investigation was evident.

In this letter we present an analysis of over 11,000 hours of all-sky images recorded by the LWA1. Including the two previously mentioned events, a total of 49 transients have been detected in this data and there is strong correlation to large meteors known as fireballs.

4.2   Discovery of Transients and Correlations with Fireballs

Image subtraction algorithms have been developed to search for transients in the full 11,000 hours of PASI data. The underlying method is that from every image, the image 15 seconds prior is subtracted. Pixels above $6\,\sigma$ of the image noise are reported as candidate events and the equatorial coordinates are calculated. All four Stokes parameters and total spectra are saved and used to check if the candidate event is radio frequency interference (RFI). The coordinates of events are also checked against known bright sources which can be focused by the ionosphere at low frequencies (Obenberger et al., 2014a).

This method has resulted in the discovery of 22 transients at 37.8 MHz, 20 at 37.9 MHz, 1 at 29.9 MHz, 1 at 25.6 MHz, and none at either 52.0 MHz or 74.0 MHz.
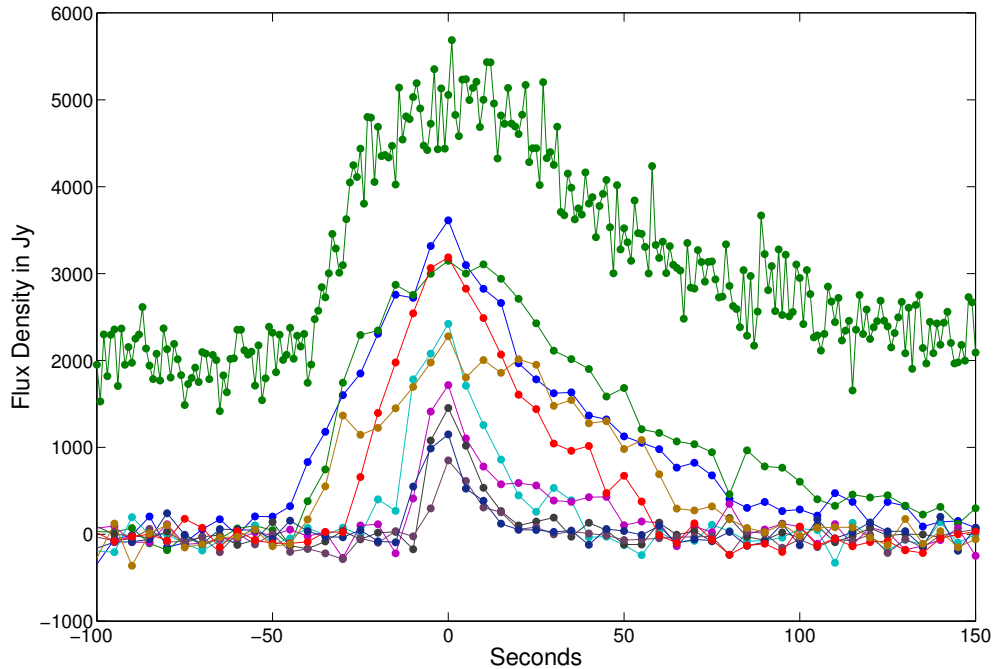
Figure 4.1: Light curves of the 9 brightest transients at 5 s integrations (Bottom). One of the transients shown on bottom (green) was also recorded using 1 s integrations (top), we show this light curve, offset by 2000 Jy, to illustrate that this transient was smooth over 1 s timescales.

The majority of these transients display a fast rise and exponential decay, lasting for tens of seconds to up to a few minutes, and have flux densities ranging from 500 to 3500 Jy (Fig. 4.1). They also show constant power across the 75 kHz band and contain low polarization levels consistent with instrumental leakage of unpolarized sources.

Most of the transients appear as point sources, meaning they are limited to $\leq 4.4°$ at 38 MHz. However some are extended over several degrees across the sky, most of which span less than ten degrees. In one case on January 21 2014, a source leaves a trail covering 92° in less than ten seconds (Fig. 4.2). The trail then slowly recedes to

the end point which glows for ∼90 seconds. The only known source that could cover this distance across the sky in less than 10 seconds and leave a persistent trail is a fireball. To investigate this further, the transients were compared with the detections from NASA's All Sky Fireball Network[1]. The network consists of 12 all-sky cameras, two of which are situated in Southern New Mexico and share a portion of the sky with the LWA1. The cameras are used to determine the 3 dimensional position, speed, absolute magnitude[2], and mass of the of the fireballs.

While the two New Mexico stations are too far South East of the LWA1 to have detected the extended transient candidate, 5 of the other 44 transients correlate in both space and time to fireballs. The fireball network could not have seen the remaining 39 events because they were either too far North West or occurred during the day. Figure 4.3 shows a histogram of the events, demonstrating that groups of transient detections appear around the times of meteor showers. This implies that a large fraction of the events not seen by the network are most likely meteors as well.

The mean delay between an event and the nearest previous major meteor shower in Figure 4.3 is 2.3 time bins[3]. In order to quantify the probability of this distribution with respect to the meteor showers, we performed a Monte Carlo simulation. Random dates were generated and checked if they occurred during actual PASI observing time at 25.6, 37.8, or 37.9 MHz. If they did occur during times at these frequencies, they were saved into an array, otherwise they were discarded. Once 44 events were compiled, the average delay between the simulated events and the closest of the four major meteor showers was calculated. This was performed 10^6 times and a normalized histogram of the results are shown in Figure 4.3. The actual data lies between 2 and 3 bins which has a probability of 0.2%.

Older events from the fireball network were used to search locations and times

---

[1]http://fireballs.ndc.nasa.gov
[2]Stellar magnitude at zenith
[3]Each time bin represents 9.125 days

for our oldest data, which was taken at 25.6 MHz and was only saved as movie files which are not searchable with the image subtraction algorithm[4]. In this data an additional five extremely bright correlated events were found, one of which covered $\sim$ 65° passing through zenith and was of comparable brightness to the Galactic plane. These additional events bring the total number to 49, 10 of which are correlated directly to fireballs.

The fireballs themselves are of the more energetic variety seen by the fireball network. The velocities of all 10 were above 50 km s^{-1}, with an average velocity of 68 km s^{-1}. The observed optical emission of each event lasted for $\sim$ 1 s, and was followed shortly (usually within 1 PASI integration) by the onset of the radio emission. The four seen near 38 MHz had peak absolute visual magnitudes of $\sim$ -4.8, -6.1, -6.3, and -6.4. The six seen at 25.6 MHz had peak absolute visual magnitudes of $\sim$ -3.3, -4.1, -4.3, -4.7, -6.6, and -7.1. Meteors with visual magnitudes brighter than -4 occur about once every 20 hours (Halliday et al., 1996). The chance overlap in space and time of 5 events[5] found randomly in PASI data with fireballs brighter than magnitude -4 within the 11,000 hours of data is about 1 in 10^{28}. Therefore it is clear that these correlations are not mere coincidence but, indeed, connected to fireballs. Figure 4.4 shows images of two fireballs observed simultaneously by the Fireball Network and the LWA1.

---

[4]Figure 4.3 only represents the 44 events found with the image subtraction algorithm, since the other 5 events were found by looking for specific fireballs rather than by a blind search. The inclusion of these would therefore skew the statistics.

[5]The 5 events found by using times and locations from the fireball network were not used in the calculation because they were not found randomly and therefore cannot be added to the random population of PASI transients.

4.3 Reflection vs Emssion

The ionized trails left by meteors have long been known to scatter radio waves, and since the 1940s the use of radar echoes became a popular method for observing their trails allowing the detection of very dim as well as daytime meteors unobservable by optical instruments. A large fraction of these observations have been of specular trails, which occur when a line perpendicular to the meteor's path satisfies the reflection requirement that the angle to the transmitter equals the angle to the receiver (Wislez, 1995). The majority of these reflections last for < 1 s, have electron line densities of $\alpha < 2.4 \times 10^{12}$ cm^{-1}, and are known as underdense meteors. A less common variety of specular trail last for several seconds, have electron line densities of $\alpha > 2.4 \times 10^{12}$ cm^{-1}, and are known as overdense meteors. These are associated with larger meteors, the largest of which are associated with optical fireballs (Ceplecha et al., 1998; Bronshten, 1983; McKinley, 1961).

A smaller subset of meteor trail echoes are non-specular, where signal is scattered in all directions rather than at angles satisfying Snell's law. These types of echoes are are not yet well understood, but most often occur when the radar is pointed perpendicular to the geomagnetic field. These types of trails can last from seconds to several minutes, but are typically much weaker than specular trails and therefore high power large-aperture radars are required to detect them (Bourdillon et al., 2005; Sugar et al., 2010; Close et al., 2011).

Meteor trail echoes are a well studied phenomenon, and their characteristics are well documented. Moreover a recent study by Helmboldt et al. (2014) using 55.25 MHz analog TV broadcasting stations for meteor scatter provides a direct example of how to detect meteor echoes with the LWA1 and how to identify them in the all-sky data. In comparison, several key differences arise between the transients reported in this chapter and what is expected from trail echoes. The differences are as follows:

First, typical transmitters are strongly polarized, resulting in reflections that are strongly polarized (Helmboldt et al., 2014; Close et al., 2011; Wislez, 1995). However no significant amount of linear nor circular polarization has been detected from the observed transients.

Secondly, a large portion of the RFI seen by LWA1 is narrower than the 75 kHz PASI band and is easily identifiable by its spectra (Obenberger and Dowell, 2011). Yet none of the observed transients contain any spectral features.

Thirdly, the light curves of the observed transients are consistent with each other, ranging from 30 to 150 s, showing a linear rise and a long exponential decay, and otherwise show a smooth evolution (Figure 4.1). A typical reflection from an over-dense trail reaches maximum brightness in just a few seconds, maintains a relatively constant average brightness while undergoing sporadic dimming and rebrightening. It then quickly decays away once it expands to the point that the density reaches the underdense criteria (Ceplecha et al., 1998; Wislez, 1995; Helmboldt et al., 2014). The observed transients are also inconsistent with light curves from non-specular echoes, which vary greatly from one to the next, following no particular pattern. More importantly, however, non-specular echoes are weaker and more rare than overdense specular echoes (Bourdillon et al., 2005; Close et al., 2011). Therefore if the LWA1 were seeing non-specular reflections it should also see many more bright specular reflections scattering from the same transmitters.

Finally, the observed transients have azimuths and elevations consistent with a uniform distribution convolved with the LWA1 power pattern (Figure 4.5). This distribution implies that the sources appear in random locations with no preferable sky position. This is inconsistent with what is expected from specular echoes of man-made radio frequency interference (RFI), which should increase towards the horizon due to the increased number of incident angles with distant transmitters required for forward scattering (Wislez, 1995). The observed pattern could be con-

sistent with nearby transmitters. However, because the signal strength depends on the inverse-cube of the distance to the meteor, there should be many very bright nearby RFI sources on the horizon but these are not observed. This pattern is also inconsistent with non-specular reflections, which are preferentially located in a relatively small region of the sky that satisfies the requirement that the pointing vector is perpendicular to the geomagnetic field (Bourdillon et al., 2005; Close et al., 2011).

For these reasons it seems unlikely that forward scattering is responsible for the signals detected from fireballs. It is therefore our conclusion that fireball trails radiate at low frequencies.

4.4 Physical Constraints on the Emission

Since PASI can only record at one center frequency at a time, there is limited spectral information for each event. Nevertheless the similarity of the light curves of fireballs recorded at 25.6, 29.9, 37.8, and 37.9 MHz implies that this emission is broad band. It also appears that they are brighter at 25.6 than at 38 MHz, suggesting a spectral slope favorable to lower frequencies. Also, there have been no detections at 52.0 or 74.0 MHz which may be the result of a sharp cutoff at higher frequencies or a steep spectrum. In either case it is clear from these observations that the emission is non-thermal, yet the exact mechanism is currently unknown.

If a magnetic field of 10 to 15 G were present within the trail, it follows that cyclotron radiation would be emitted at the observed frequencies by the electrons in the plasma. However, the surface geomagnetic field is only 0.5 G, so this would require the generation of a strong magnetic field by a fireball, an effect that has never been observed.

Brightness temperature for a radio source can be calculated using the equation:

$$T_b = \frac{S_\nu \lambda^2}{2k\Omega} \tag{4.1}$$

Where S_ν is the flux density of the source, λ is the observed wavelength, k is the Boltzmann constant, and Ω is the solid angle of the source. The solid angle of the emitting portion of the fireball is estimated by using typical size scales reported for bright meteors trails.

A typical fireball observed by the LWA1 has a peak flux density of 1 kJy, 20 s after first light, and most are point sources with a measured beam size of 4.4° at 37.8 MHz. Meteor plasma trails are typically modeled as long cylinders with radii much smaller than their length. Assuming a height of 110 km and zenith angle of 40°, an angular size of 4.4° corresponds to 12 km, which is a reasonable value for the length of the emitting part of the plasma trail. However for large plasma trails a typical initial radius is 10 m, which quickly expands due to diffusion. It is estimated that at 20 s after entry, the radius of the expanding trail would be ~100 m (Ceplecha et al., 1998; Bronshten, 1983; McKinley, 1961). Given these dimensions the estimated brightness temperature is 3×10^5 K. This temperature is two orders of magnitude higher than the typical peak temperature of a fireball trail, and this provides further evidence that the emission is non thermal.

While the spectral slope has yet to be fully measured, the total energies of the radio emission are estimated by assuming a flat spectrum from 10 to 50 MHz and heights of 110 km. These assumptions yield total radio energy estimates ranging from 10^{-4} to 10^{-2} J, which is one part in 10^{12} to 10^{10} of the kinetic energy of a typical fireball. Further observations are in progress to better characterize the spectral properties of this emission, and to get better estimates of the total amount of energy radiated at radio frequencies.

4.5   Discussion

Decametric radio emission from meteors has not been previously detected, but this is not the first time its existence has been discussed. Hawkins (1958) conducted a search for radio emission, but reported only upper limits with a 5 σ sensitivity of $\sim 10^8$ Jy at 30 MHz for 1 s bursts. It is also interesting to note that in the last several decades detections of extremely low frequency (ELF[6]) and very low frequency (VLF[7]) emission have been reported coincident with large meteors (Guha et al., 2012; Keay, 1980; Beech et al., 1995). The physical mechanism responsible for this emission is not well understood, but might be related to our detections of higher frequency emission.

Given the vast range in energies and size scales of meteors and their corresponding plasma trails, this emission may exist at a wide range of frequencies, timescales, and energies. Investigating this emission further will yield new insights into the physics of meteors and their interaction with our atmosphere. Moreover fireballs are now a known radio transient foreground source and need to be taken into account when searching for cosmic transients. It is interesting to note that transient atmospheric phenomena, unknown to emit at radio frequencies, have been proposed as the possible source of Fast Radio Bursts (Kulkarni et al., 2014; Katz, 2014; Burke-Spoloar et al., 2011; Thornton et al., 2013; Lorimer et al., 2007). In this chapter we reported observations of atmospheric radio emission, namely high energy meteors, which may be in some way related to FRBs.

---

[6] 3 Hz to 3 kHz
[7] 3 kHz to 30 kHz

4.6 Acknowledgments

Figure 4.2: Image of the sky, after subtraction, of the fireball which covered 92°. The edge of the circle marks a cutoff of 25° above the horizon. Strong constant sources Cassiopeia A and the Virgo A, Taurus A, and the Galactic Plane have left weak residual signals in the image.
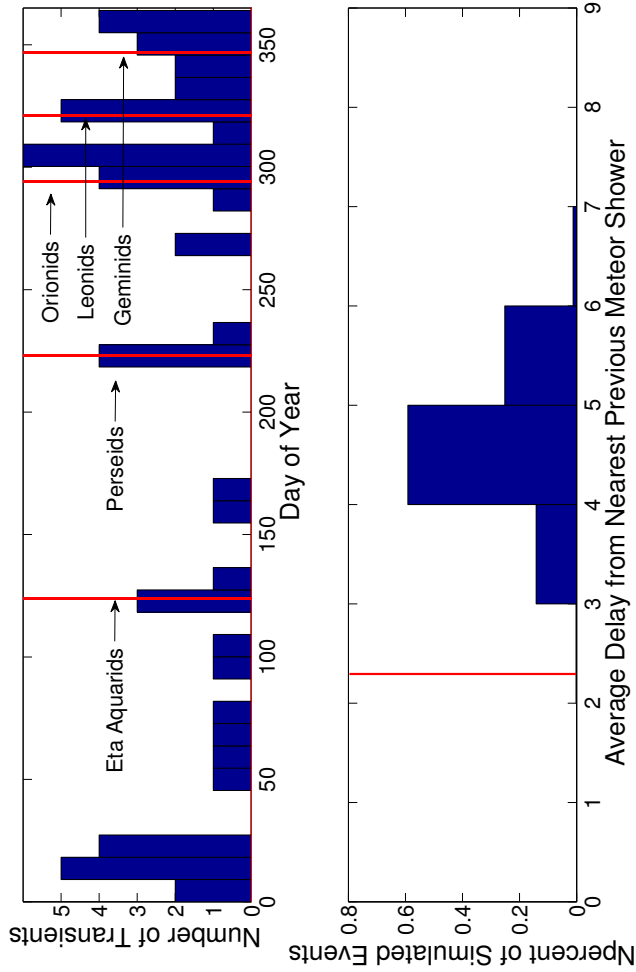
Figure 4.3: (Top) A histogram showing the number of events per day of year. The full 365 days of the year are grouped into 40 bins, each bin representing 9.125 days. The red lines show the dates of several major meteor showers. The large clump which occurs near January 10 - 25 does not have a major meteor shower associated with it and may be evidence of a previously unknown fireball stream. (Bottom) Shown here are the normalized results of conducting 10^6 iterations of simulated data spread over the 7028 hours of data recorded at 25.6, 37.8, and 37.9 MHz. For every iteration 45 events were generated within the actual observing times, and the mean delay of all the events to the closest meteor shower was calculated. The actual measured delay of 2.3 is shown in red.
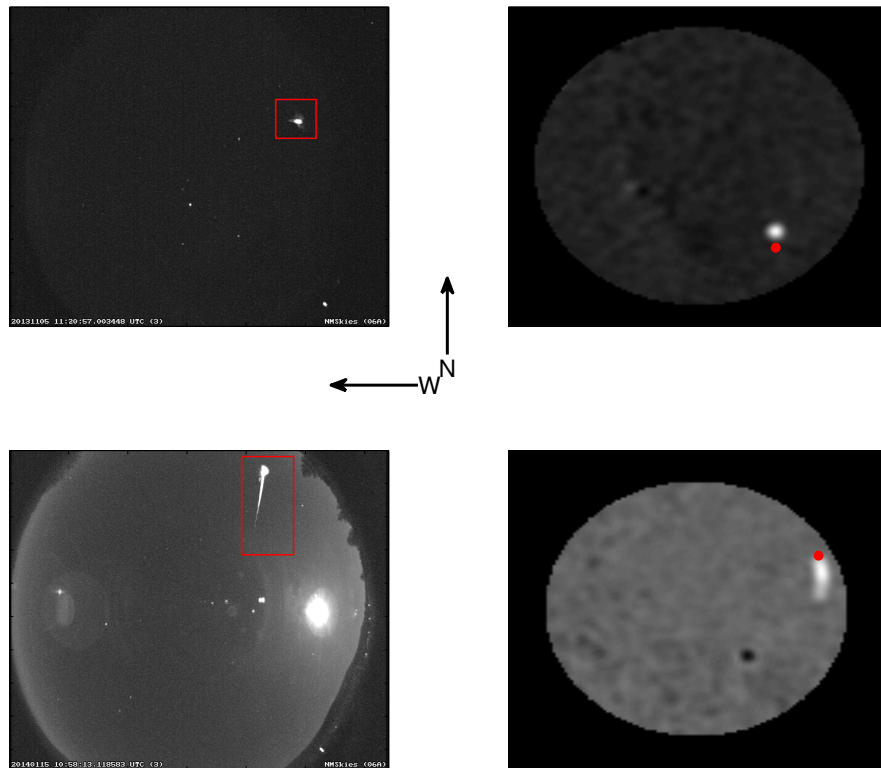
Figure 4.4: Comparison images from the NASA All-Sky Fireball Network station located in Mayhill, NM (Left) and PASI (Right). The red rectangles outline the fireballs in the Fireball Network images. The red dots on the PASI images show the final location of the fireball as provided by the Fireball Network. For the PASI images, the edge of the circle marks a cutoff of 25° above the horizon. East-West orientation of the PASI images have been reversed from their normal appearance to have the same orientation as the Fireball Network Images. The large bright disk in the lower left image is the moon.
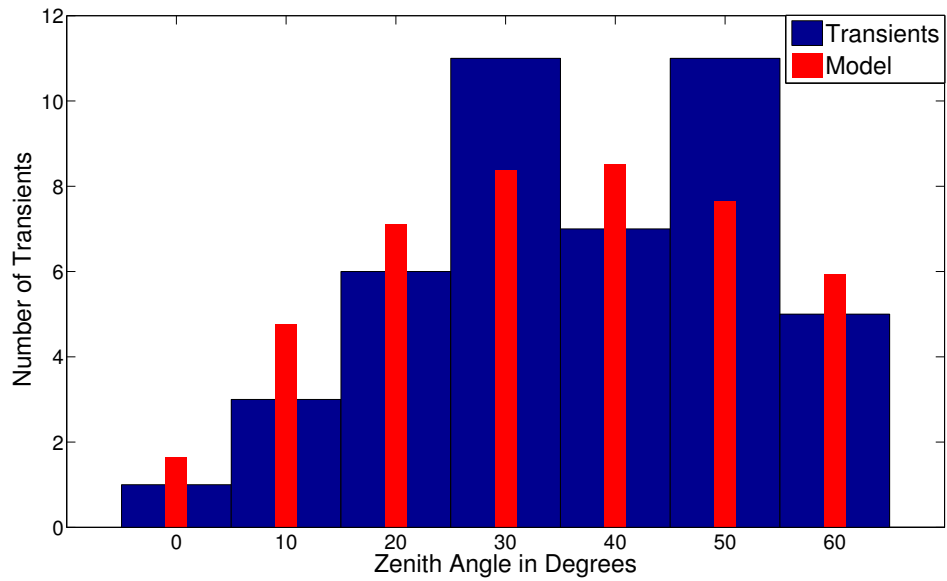
Figure 4.5: A histogram showing the number of events as a function of zenith angle. The blue bars show the actual measured distribution of the transients. The red bars show a model based on a uniform distribution convolved with the power pattern of the LWA1.

Chapter 5

Fireball Radio Spectra

The contents of this chapter were submitted in a modified form as Obenberger et al. 2015, to JGR Space-Physics

Abstract: We present dynamic spectra from the LWA1 telescope of two large meteors (fireballs) observed to emit between 37 and 54 MHz. These spectra show the first ever recorded broadband measurements of this newly discovered VHF emission. The spectra show that the emission is smooth and steep, getting very bright at lower frequencies. We suggest that this signal is possibly emission of Langmuir waves and that these waves could be excited by a weak electron beam within the trail. The spectra of one fireball displays broadband temporal frequency sweeps. We suggest that these sweeps are evidence of individual expanding clumps of emitting plasma. While some of these proposed clumps may have formed at the very beginning of the fireball event, others must have formed seconds after the initial event.

5.1   Introduction

Generally speaking, fireballs are meteors that appear optically brighter than the planet Venus (magnitude -4) , and occur from meteoroids larger than ~ 100 grams. Such large meteors are considered rare given that an observable area of 10^6 km^2 has a rate of occurrence of ~ 200 per year (Halliday et al., 1996). Several fish eye camera observatories currently operate year round, finding hundreds of fireballs a month. For instance the NASA All Sky Fireball Network (http://fireballs.ndc.nasa.gov) operates 15 cameras in 8 different states including two in New Mexico and 3 in Arizona. These cameras are situated such that they can triangulate the position of the fireballs, and thereby get the velocities and orbital parameters.

Similarly the First Station of the Long Wavelength Array (LWA1; Ellingson et al. (2013a); Taylor et al. (2012)), located in central New Mexico, creates images of the entire sky. However these images probe the low end of the electromagnetic spectrum (10 - 88 MHz) in the high frequency (HF) and very high frequency (VHF) bands. In 2014 the LWA1 was used to serendipitously discover that meteors, specifically fireballs, radiate non-thermal emission in this frequency range (Obenberger et al., 2014b). These radio transients were identified as fireballs in part because the two Fireball Network cameras in New Mexico are close enough to the LWA1 to see some of the same events.

Little is known about the radio properties of fireballs. In Obenberger et al. (2014b) we used polarization, light curves, sky position, meteor shower correlation, and a limited amount of spectral information to show that the 49 radio transients we detected were most likely due to non-thermal radio emission from fireballs. These fireballs were detected at 25.6, 30, and 38 MHz, and it was noted that those at 25.6 MHz were considerably brighter, suggesting that the emission had a steep spectrum. The light curves of these fireballs were all very similar, displaying a fast linear rise

70

followed by a slower exponential decay, with a total duration of 10 to 200 seconds. Such long durations are unusual for atmospheric radio transients at these frequencies; this fact alone sets this phenomenon apart from other sources. Radio frequency (RF) emission from electrical discharges such as lightning are short (10s of ms) (Warwick et al., 1979), therefore the two are most likely unrelated. Similarly the fireball emission does not appear to be related to the other known meteor RF phenomenon, namely the sub microsecond EMPs caused by hypervelocity impacts (Close et al., 2013, 2010) and the short pulses of very low frequency (VLF) and extremely low frequency (ELF) radio emission observed to come from large fireballs (Guha et al., 2012; Keay, 1980; Beech et al., 1995). Finally the fact that the gyro-frequency of the geomagnetic field is ~1.5 MHz, an order of magnitude less than the observed frequencies, indicates that the emission is not cyclotron.

A possible candidate for the emission is the radiation of Langmuir waves from the meteor plasma trail. These waves could possibly be driven by an electric and/or turbulent interaction with the ionosphere. The observed emission would be near the local plasma frequency, $f_p = \sqrt{n_e e^2/\pi m_e}$, where n_e is the electron density, e is the charge of the electron, and m_e is the mass of the electron. This and the rest of the equations in the chapter are given in cgs units. Since the meteor trail would contain a gradient in the electron densities, such emission would be a probe into the profile of the trail and give clues to how the trail evolves.

The initial fireball emission discovery was made using images from the Prototype All-Sky Imager (PASI; Obenberger et al. 2015a), a backend correlator of the LWA1 telescope. PASI creates narrowband (75 kHz) all-sky images, integrated for 5 seconds; and the center frequency can be tuned anywhere between 10 and 88 MHz. The images are permanently stored in an archive which now contains over 11 million images (> 15,000 hours). These images have been searched in the manner described in Obenberger et al. (2014b) and have resulted in the detection of 101 transients, the

vast majority (if not all) of which are fireballs.

We also observe with the LWA1 phased array mode, where the antennas are delayed and summed to form a pencil beam. Since this is done digitally we can point multiple beams at one time. During PASI operation we fix three beams on the sky around zenith, covering a narrow region (~ 50 deg^2) of the sky. These observations had the primary objective of finding dispersed transient events, and in addition they could be used to capture low frequency spectra from fireballs. The beams provide 36 MHz of bandwidth coverage with high frequency and time resolution, and since we can readily detect fireballs with PASI, if one occurs within a beam we can retrieve the broadband spectra. This campaign has been successful, with the recording of two dynamic spectra from fireballs.

This chapter presents radio dynamic spectra of these two fireballs, and is organized as follows: §5.2 describes the observations made. §5.3 provides analysis of the image data. §5.4 provides analysis of the dynamic spectra. §5.5 describes why the observations cannot be due to reflections of celestial sources. §5.6 provides a basic model for the emission. Finally §5.7 presents our conclusions.

5.2   Observations

In October of 2013, we began an observing campaign to search for transients with LWA1 beam formed data. This mode of operation uses three beams centered around zenith at azimuths of 60°, 180°, and 240° each at an elevation of 87°, and runs simultaneously with the PASI all-sky imaging mode described in Obenberger et al. (2015a). For simplicity, these beams will hereafter be referred to as B1 (60°), B2 (180°), and B3 (240°).

Each beam has two tunings centered at 45.45 MHz and 65.05 MHz, and each

tuning has 19.6 MHz of bandwidth, only 18 MHz of which are usable due to the digital filter roll off. These center frequencies were selected to avoid the video carrier for analog TV channel 2 at 55.25 MHz, which is one of the strongest radio frequency interference (RFI) emitters in the LWA1 frequency range. This channel has actually been used by LWA1 scientists to study meteors using forward scatter (Helmboldt et al., 2014).

Rather than saving the raw voltage time series, we use the spectrometer mode, provided through the data recording subsystem, which channelizes, integrates, and records the data in real time at a much lower data rate. For these observations we selected a mode that provides 1024 19.14 kHz wide channels and 40 ms integration steps. Due to limited computational resources, only the XX and YY auto correlations are computed, which allows us to calculate the Stokes I and Q polarizations. However, since we do not compute the XY and YX cross correlations we cannot calculate Stokes U and V. The dynamic spectra are recorded at a data rate of 1.37 GB hr^{-1} beam^{-1} and are copied to the LWA1 Data Archive. This project has accumulated over 5,600 beam hours to date.

Fireballs are detected and located using PASI and the image subtraction pipeline described in Obenberger et al. (2015a). When a fireball occurs within one of the three beams, the corresponding data can be downloaded from the archive and analyzed. So far this has occurred twice, with both events occurring during the Orionid meteor shower. The first was on October 17, 2014 at 7:21 UT (hereafter referred to as FB1) and the second on October 26, 2014 at 12:58 UT (hereafter referred to as FB2). FB1 was also caught by the NASA All-Sky Fireball Network and was measured to have a velocity of 52 km/s with an upper altitude of 100.9 km and lower altitude of 85.9 km. The estimated peak absolute magnitude was $\sim$ -3 resulting in an estimated initial mass of $\sim$ 10 grams.

Without optical spectra or LIDAR it is impossible to determine the temperature

of the plasma, especially in the 10s of seconds after the initial optical emission. For typical meteors, the initial temperature of the plasma trail is between 5,000 and 10,000 K (Ceplecha et al., 1998), and quickly decreases coming into equilibrium with the ambient surroundings ($\sim$ 200 K) usually within milliseconds (Ceplecha et al., 1998). However in the case of optical persistent trains, a potentially related phenomenon, the walls of the plasma tube have been shown to be about 20 - 50 K above the ambient surroundings 3 minutes after vaporization (Chu et al., 2000).

5.3   PASI Images Analysis

The transient detection pipeline is straightforward and described in detail in Obenberger et al. (2015a). Once detected however, further analysis needs to be conducted to determine whether the transients are indeed fireballs. In the two cases presented in this chapter, it is clear from their light curves and resolved image elongation that they match the description of fireballs presented in Obenberger et al. (2014b). As can be seen in Figure 5.1, the light curves display the typical shape of a fast rise and slower decay, and the images of the fireballs show clear elongation. Moreover FB1 was confirmed by the fireball network to have an optical counterpart leaving no doubt that it was indeed a fireball. FB2 occurred 21 minutes before sunrise and therefore could not have been detected by the fireball network.

Figure 5.1 also shows the proximity of the three beams to the trails of the fireballs. It is clear that not all of the beams will have equal amounts of emission within them, moreover some lack any significant emission. In particular for FB1, PASI shows that B1 did not have any significant emission present, which was confirmed when analyzing the beam data. The fireball network calculated a trajectory for FB1 heading NW, which in the PASI image is to the upper right. Therefore B3 is located near the end of the trail, while B2 is located more towards the middle, which is the brightest

region. For FB2, the beams were more equally distributed, with B2 containing the most received power. However since FB2 was not detected by the fireball network, we do not know the trajectory.

Still, we may be able to determine the trajectory of FB2. Both FB1 and FB2, along with many other fireballs, create observable streaks in the radio images. These streaks are similar to the optical counterparts, in that the radio emission starts at one end of the trail and moves to the other end. However it typically takes 10 to 40 seconds for the radio emission to reach the end of the trail, whereas the optical portion typically takes less than 2 seconds. Therefore the radio streak is not displaying the physical formation of the trail. Despite this, in all 10 cases (including FB1) where a fireball was detected by the fireball network and displayed observable elongation in PASI, the emission moves from the upper portion of the trail to the lower portion.

The radio emission of FB2 streaks to the south east. Therefore, if we assume that the emission starts at the upper region for all fireballs, then we can say that FB2 was headed SE. This method may allow for the LWA1 to determine the trajectory of all observed fireballs.

Given the fact that the timescale of the upper-to-lower transition is much too long to be tracing the initial formation of the plasma we consider the idea that it may be related to the diffusion of the dense plasma trail into the less dense ionosphere. The diffusion constant is exponentially dependent on the altitude, where the diffusion rate increases at higher altitudes. Therefore if the majority of the trail has a high enough electron density that the plasma frequency is above the observing frequency of PASI, then as the trail expands the plasma frequency of the upper regions will reach the observing frequency first, followed by the lower regions. It should be noted that the diffusion would be further complicated at higher altitudes by geomagnetic field and nonlinear diffusion (Jones, 1991; Dyrud et al., 2001). If the emission is indeed coming from radiation of Langmuir waves, then further study may prove useful for studying

high elevation diffusion phenomena.

5.4   Dynamic Spectra Analysis

Each dynamic spectrum had a model bandpass divided out. This model is based on the responses from the antennas and filters. Once the bandpass is divided out, the background sky needs to be subtracted out. This is done by simply subtracting a smoothing spline fit; spectral features due to RFI were removed in the data that we fit to the median spectrum from the minute prior to each fireball. This method works well because the spectral and amplitude features of the sky change very little over the period of a few minutes, and this is confirmed by the fact that the sky corrected spectrum is still flat and centered at zero after the fireball emission has ended.

In all of the beam data there were several narrow band transmitters that leaked into the beams via the side lobes. Furthermore, both plasma trails reflected numerous additional transmitters. The majority of these frequencies have been masked out in the dynamic spectra. In a few instances the reflections are so bright that they saturate the beam formed output, and all other frequencies at those times drop significantly in power. These times have been masked out as well. It is interesting to note that the duration of the narrow band reflections as a function of frequency is similar to the broad band emission. This would make sense if the emission was coming from Langmuir waves given that the reflections of a transmitter would end once the plasma frequency dropped below the transmitter's frequency.

No significant flux for either FB1 or FB2 was detected in B1. In B3 we did detect FB1, although it contained less flux than B2 as was expected from the PASI images in Figure 5.1. For FB2, B3 was completely saturated by a very strong reflection lasting the duration of the event.

Figure 5.2 shows the full dynamic spectra from B2 of FB1 and FB2. Figures 5.3 and 5.4 show closeups from B2 of FB1, in both Stokes I and Q, while Figure 5.5 shows a similar closeup of B3.

5.4.1   Unpolarized Broadband Power Emission

Qualitative inspection of the dynamic spectra of each fireball revealed that the received power has a steep, smooth dependence in frequency for most of its duration, where the power increases at lower frequencies. This was not the case in FB1 between 10 and 20 s, which contained narrow, linearly polarized frequency sweeps with enhanced emission from 40 to 41, 42 to 44, and 50 to 54 MHz. Figures 5.3, 5.4, and 5.5 show that these regions are linearly polarized with enhanced dark red between 40 and 44 MHz, and enhanced yellow between 50 and 54 MHz. Figure 5.6 shows the averaged spectra from the times when these sweeps are present and when they are not. The smooth emission from FB1 was analyzed by examining the averaged spectrum between 26 and 34 s, which only exhibited a small number of spectral sweeps. No spectral sweeps were detected in the case of FB2, thus the entire duration of the emission was averaged.

While we accounted for the bandpass of the instrument, there is still an instrumental contribution to the spectra, and there are two components to this. First the full width at half maximum (FWHM) beam size depends on the frequency like: FWHM$\sim c/fD$ where f is the frequency, c is the speed of light, and D is the diameter of the telescope. So if a source is off the center of the beam, the higher frequencies will have a weaker response. Secondly, the meteor is not a point source, rather it is a line with effectively no width. This is because a fireball in this size range would only create a plasma trail tens of meters wide, which would appear on arc second scales from ~ 100 km away, far smaller than the size of the LWA1 beams. Therefore more

of the physical source is seen at the lower frequencies, further adding to the spectral shape.

We modeled these effects by creating 2D Gaussian point spread functions (PSF, Taylor et al. 1999) for a 100 m diameter dish at 13 frequencies from 20 to 85 MHz. We then simulated an infinitely long meteor with a width that is much smaller than the angular beam size and flat spectrum passing through each PSF at different offsets from center. Since the beam-width goes like f^{-1}, the zero angle offset is a perfect power law with index -1. However, as the offset angle increases, the shape deviates from a power law.

We estimate the angle offsets of FB1 and FB2 from the nearest beam (B1 in both cases) by simply using the images in Figure 5.1. Doing this gives offsets of $\sim 0.75°$ and $\sim 2.75°$. Dividing out the spectral contribution for these offsets gives a seemingly linear dependence below ~ 50 MHz. Above 50 MHz the spectra of both fireballs flatten to zero. See Figure 5.7.

The temporal smoothness of the dynamic spectrum further bolster the argument that the observed fireballs are not mere reflections. Reflections fluctuate in brightness due to both interference of multiple reflection points as well as the changes in shape and orientation of the trail caused by local winds. The dynamic spectra show smoothness on timescales of 40 ms, which is much finer than the previous finest example showing 1 s resolution (Obenberger et al., 2014b).

5.4.2   Polarized Broadband Frequency Sweeps

The dynamic spectrum of FB1 contains linearly polarized spectral sweeps. Figures 5.3 and 5.4 show closeups of these regions in B2, with both Stokes I and Q polarizations, and Figure 5.5 shows a similar closeup of B3. Given their large bandwidth and periodicity they are certainly not reflected radar, and are most likely an inherent

feature of the emission. The sweeps seen in B2 are very defined and have a frequency separation of ~ 1 MHz and a temporal separation of ~ 250 ms, whereas the sweeps seen in B3 are less defined and have a frequency separation of ~ 1.5 MHz and a temporal separation of ~ 900 ms.

Polarization

With only Stokes I and Q we do not get the full polarization picture. However, at least some portion of the sweeps are linearly polarized, and this polarization is the same with both the sweeps seen in B2 and B3. At 43 MHz the sweeps are $\sim 80\%$ -Q, whereas at 51 MHz they are $\sim 50\%$ +Q, with the magnitude of Q polarization dropping off significantly on either side of these two frequencies. We find that Faraday rotation cannot account for the severity of the change from -Q to +Q. To show this we take 51 and 43 MHz to be the frequency separation between a 90° rotation in polarization. Assuming that the pulse has $\sim 80\%$ polarization at 43 MHz and $\sim 50\%$ at 51 MHz, the angle of rotation between two frequencies is:

$$\gtrsim \Theta = RMc^2 \left(\frac{1}{f_1^2} - \frac{1}{f_2^2} \right), \tag{5.1}$$

where RM is the commonly used rotation measure (Taylor et al., 1999), which is given by:

$$RM = \frac{e^3}{2\pi m_e^2 c^4} \int_0^d n_e(l) B_{||}(l) dl, \tag{5.2}$$

where e is the charge of an electron, m_e is the mass of the electron, and $B_{||}$ is magnitude of the magnetic field parallel to the propagation of the wave. In this case since the fireball was at zenith, $B_{||}$ is just the vertical component of the local

geomagnetic field, and is considered constant between 0 and 100 km. Using the National Geophysical Data Center of the National Oceanic and Atmospheric Association (www.ngdc.noaa.gov/geomag-web/) we estimate $B_{||}$ to be 0.4 G. Therefore, assuming a 90° polarization angle rotation between 43 and 51 MHz, we calculate an electron column density of 1.2×10^{12} cm^{-2}.

While we do not have the exact electron density of the ionosphere surrounding the fireball trail, the event occurred at 01:21 MT, which implies that the electron density of the ionosphere was most likely very low. Indeed, we can limit the density using public ionogram data from the Digital Ionogram Database (DID). At the time of the fireball, the electron density below 200 km for Boulder, CO; Austin, TX; and Melrose, CA was less than 10^3 cm^{-3}. Therefore, for the ionosphere to contribute such a large rotation would require a path length of 10,000 km, rendering this scenario impossible.

Next we consider the electron contribution from the fireball trail itself. We assume the pulse originated inside the trail, traveling a distance d through the plasma. Since the lower end of our band is ~ 37 MHz we set an upper limit for the plasma frequency within the distance d to 37 MHz, which corresponds to an electron density of 1.7×10^7 cm^{-3}. At such a density the required distance would be ~ 760 m. As can be seen from Figure 5.1 the angular size of FB1 is $\sim 20°$, which gives it a projected length of ~ 30 km at ~ 90km, and the fireball network calculates a similar length of 32 km. Therefore the fireball appears to be viewed nearly edge on, where the projected depth of the trail is approximately equal to the actual width of the trail. Therefore it is unlikely that the trail would have expanded to a width of 760 m 10 seconds after impact. Moreover, while a plasma density of 37 MHz is reasonable for a portion of the trail, it is very unlikely that such a density would expand outward for 100s of meters.

For these reasons the opposite polarity at 43 and 52 MHz appears to be an

inherent property of the frequency sweeps, and are no doubt clues to their origin.

Frequency-Time Dispersion

At first glance it is difficult to tell if the sweeps in B2 are continuous across the entire band. There appears to be a decrease in brightness between 45 and 50 MHz, moreover there was a significant amount of RFI removed from this portion of the band. Nevertheless, we can see that the sweeps do move through the whole band, an observation that is perhaps more obvious for the sweeps in B3 (Figure 5.5) than those in B2 (Figure 5.3). This is also confirmed when we extracted the brightest points from the sweeps below and above the region of decreased emission, and they were noticed to be connected via a power law. We therefore modeled each set of points using a least squares fit of the function:

$$t(f) = \frac{a}{f^b} + c, \tag{5.3}$$

where t is the arrival time of the pulse, f is the frequency and a, b, and c are all free parameters. The results of the fits are given in Table 1. The values of b ranged from 0.8 to 1.8, with an average value of 1.28, and standard deviation of 0.35. It is interesting to note that all modeled values of b are less than 2. If the dispersion was caused by typical electromagnetic dispersion in a plasma, where the group velocity of a wave is a function of frequency, the measured value for b should always be greater than or equal to 2. This is because within an unmagnetized plasma the group velocity for an electromagnetic wave is:

$$v_g = c\sqrt{1 - \frac{f_p^2}{f^2}}, \tag{5.4}$$

where f_p is the plasma frequency and c is the speed of light. We are only considering O-mode waves, where the electric field is parallel with the background magnetic field (E $\parallel$ B$_0$) and the dispersion relation is the same as an unmagnetized plasma (Kallenrode, 1998). We do this because the gyro-frequency of the geomagnetic field is nearly a factor of 30 less than the observed frequencies and thereby the assumed plasma frequencies. Therefore the upper hybrid frequency is only $\sim$ 20 kHz greater than the plasma frequency. Since X-mode waves (E $\perp$ B$_0$) have a cutoff at the upper hybrid frequency they would not be distinguishable from O-mode waves within the parameters of our observations. At this time we cannot rule out the possibility that the plasma emission could contain hybrid waves; further study of the radio emission may shed light on the responsible wave modes. Either way the fact that the hybrid frequency is so close to the plasma frequency indicates that the unmagnetized approximation in Equation 5.4 is valid for the propagation of X-mode waves as well. Therefore the time of arrival of a pulse generated at a distance d within a plasma can then be calculated as:

$$t(f) = \int_0^d v_g dl = \frac{1}{c} \int_0^d \frac{dl}{\sqrt{1 - \frac{f_p^2}{f^2}}} =$$

$$\frac{1}{c} \int_0^d \left(1 + \frac{f_p^2}{2f^2} + \frac{3f_p^4}{8f^4} + \frac{5f_p^6}{16f^6} + O(f^{-\delta}) \right) dl. \quad (5.5)$$

Comparing Equation 5.3 and Equation 5.5 it can be seen that the value for b due to this type of dispersion would be a minimum of 2. Moreover this only occurs when $f \gg f_p$, which is certainly not the case for the observed fireballs. Therefore the frequency-time dispersion must have some other explanation.

5.5 Reflections from Celestial Continuum Sources?

Up until this point we have assumed the conclusions of Obenberger et al. (2014b), namely that the observed fireballs are emitting. In Obenberger et al. (2014b) we showed that it was very unlikely that the detected signals associated with fireballs were due to reflections of man-made RFI. However we did not address the possibility of reflections from bright celestial sources (e.g. Taurus A, Virgo A, Cassiopeia A, Cygnus A, and the Galactic Center). Such reflections would not be subject to many of the previously presented arguments against reflections of man-made RFI. In particular these sources are unpolarized and broadband, so they are similar to the fireballs in this respect. Nevertheless, we find that such reflections are highly unlikely for the following reasons.

For one, reflections of celestial sources should also undergo the same sporadic variations seen in reflections of man-made RFI. As described in §5.4.1 the radio counterpart to fireballs are very smooth in time.

Moreover there are only 5 sources brighter than the fireballs we see ($\gtrsim 1$ kJy at 38 MHz). Therefore the probability that the proper geometry would be present for a specular reflection is very low, certainly much lower than the occurrence of fireballs we observe (Obenberger et al., 2014b).

Furthermore the received power from an overdense reflection drops like the inverse square of the distance to the trail (McKinley, 1961; Ceplecha et al., 1998; Wislez, 1995). Therefore such reflections should be much dimmer than the sources they are reflecting. However in several cases the received power is 10 to 20% of the brightest possible reflected source.

5.6 The Nature of the Emission

In this section we provide a simple hyopothesis that is a first approach to explain the emission through radiation of Langmuir waves. Since the cyclotron frequency is over a factor of 30 less than the observed plasma frequencies we ignore the role of the geomagnetic field. It may be that the magnetic field is an important factor for the emissive process, so the following hypothesis should only be considered valid parallel to the magnetic field.

5.6.1 Langmuir Wave Generation

Meteor trails possess the necessary electron densities such that if Langmuir waves were produced they would be within the LWA frequency range (Ceplecha et al., 1998; McKinley, 1961). Yet this fact neither explains the occurrence of Langmuir waves nor the mechanism by which they are radiated.

The Langmuir waves could not be left over from the initial vaporization because such waves would be damped out due to the high electron-neutral collision rate. From (Kelley, 2009), the electron-neutral collision rate for the lower ionosphere is given by:

$$\gamma_{en} = 5.4 \times 10^{-10} n_n \sqrt{T_e}, \tag{5.6}$$

where n_n is the neutral density and T_e is the electron temperature. The neutral density at 90 km is 3.9×10^{13} cm^{-3} (Kelley, 2009) and the electron temperature has come to equilibrium with the ambient ionosphere at ~ 200 K. Therefore the electron/neutral collision frequency is $\gamma_{en} = 3 \times 10^5$ s^{-1}. The observed plasma frequencies are ~ 100 times greater than the collision frequency, allowing plasma

waves to be driven and amplified, provided the driving mechanism has a growth rate greater than the collision frequency.

In comparison Type II and III solar radio bursts are thought to be the product of Langmuir wave radiation (Reid & Ratcliffe, 2014; Melrose, 1987). Electron beams are well known to be efficient drivers of Langmuir waves through the bump-on-tail instability, in which a high velocity bump in the electron velocity distribution drives the electrons to oscillate. It is thought that this is the mechanism in which Langmuir waves are produced in Type III bursts.

In the case of meteors, it is possible that an electron beam streaming through the ionosphere could interact with the meteor trail, or perhaps a beam could be generated within meteor trail itself. A recent model predicts that meteor trails may effectively short circuit the ionosphere creating current running down the length of the meteor (Dimant et al., 2009), this may be sufficient means of creating the necessary electron beam.

To explore the idea of electron beam generated Langmuir waves, let us consider an electron beam with a Maxwellian distribution traveling through a meteor trail, and lets assume the trail and beam have the same thermal velocity. Also for simplicity let us ignore the diffusion effects of the geomagnetic field. Under the weak growth rate approximation for a thermal plasma the growth rate (Gurnett, 2005) is given by:

$$\gamma = \frac{\pi}{2} \frac{\omega_p^3}{k^2} \frac{n_b}{n_e} \left. \frac{\partial F_0}{\partial v_z} \right|_{v_z = \omega/k}, \tag{5.7}$$

where $\omega_p = 2\pi f_p$, k is the wave number, n_b is the beam density, n_e is the local electron density in the meteor trail, v_z are the electron velocities in the direction of the beam, and F_0 is the normalized distribution function of the meteor plasma and

the beam. Since this is only valid for large phase velocities, we only need to consider the contribution to F_0 by the beam, which we assume has a velocity at least four times the average thermal velocity. F_b is represented by:

$$F_b = \frac{1}{\sqrt{\pi}v_{th}}e^{-\frac{(v_z - v_b)^2}{v_{th}^2}}, \tag{5.8}$$

where v_b is the beam velocity and v_{th} is the electron thermal velocity. Substituting F_b for F_0 in Equation 5.7, taking the derivative, and evaluating at $v_z = \omega/k$, we can find the growth rate any frequency. The maximum growth rate is at $\omega \approx k(v_b - v_{th})$, evaluating at this frequency we get:

$$\gamma \approx \frac{\sqrt{\pi}}{e}\frac{n_b}{n_e}\frac{\omega_p^3}{(kv_{th})^2}. \tag{5.9}$$

Finally using the approximation $k \approx \omega_p/v_b$, we obtain,

$$\gamma \approx \frac{\sqrt{\pi}}{e}\frac{n_b}{n_e}\left(\frac{v_b}{v_{th}}\right)^2\omega_p. \tag{5.10}$$

Insisting that the growth rate is greater than the electron-neutral collision frequency, i.e. $\gamma > \gamma_{en}$, we can solve for n_b/n_e given a beam velocity. Assuming a 0.4 eV electron beam ($v_b \sim 4v_{th}$), to excite waves within a plasma with a plasma frequency of 37 MHz would require a beam density of $n_b = 2,000$ cm^{-3} or about 0.01% of the local electron density ($1.7{\times}10^7$ cm^{-3}). Although speculative, it is not unreasonable to hypothesize that such a weak beam could be generated directly within the trail itself. Dimant et al. (2009) predicts large currents flowing outside and within meteors trail due to the large potential differences in this region of the ionosphere. The high electron/neutral collision frequency ($\sim 3 \times 10^5$ Hz) may indeed suppress the

formation of any self generated electron beam from this current. However a beam might form if the current were to heat a narrow channel of plasma to high temperatures along the length of the trail. The decreased collision frequency of the heated channel may allow electrons to be accelerated to high velocities and escape into the surrounding plasma.

It should also be noted, that the bump-on-tail instability does not require a beam; any source of high energy non-thermal electrons would be sufficient. Optical persistent trains, known to occur from high velocity fireballs, display an infrared to extreme ultra-violet (EUV) glow in the meteor trail and last for seconds up to hours after the disappearance of the meteor (Borovicka, 2006). The luminosity of long lasting persistent trains is thought to be driven by exothermic chemical reactions, although all of the the relevant relations have not yet been identified. It is hypothetically possible that the energetic processes involved or the resultant emitted photons could pump energy into some electrons creating a bump in the distribution function. A related process has been suggested as an explanation for suprathermal electrons detected in the lower E-region, where thermal electrons may gain energy through interactions with vibrationally excited N_2 molecules and possibly form an non-Maxwellian distribution (Oyama et al., 2011).

5.6.2 Langmuir Wave Emission

As emitters of Langmuir waves, Type II and III Solar bursts are natural analogs to our proposed model for meteor emission. Although it should be noted that a complete theory describing the radiation mechanism of Langmuir waves from Solar bursts has yet to be determined. Several mechanisms have been proposed such as wave-wave interactions (Cairns and Melrose, 1985; Cairns, 1988), linear mode conversion (Hinkel-Lipsker et al., 1992; Kim et al., 2013), and antenna radiation (Papadopoulos

& Freund, 1978; Malaspina et al., 2012).

Three dimensional models of meteors trails have shown that atmospheric winds can create high levels of turbulence (Oppenheim & Dimant, 2015). This turbulence then creates clumps of plasma along the trail, which is in contrast to the idea that the trail remains a pristine cylinder with a Gaussian-like electron density distribution. It is not known if this could help drive Langmuir waves, however it would easily create large density gradients, which may aid the emission process. Especially in a scenario such as antenna radiation, which requires density clumps of size scales similar to the wavelength of the emitted waves (5 to 10 m).

Ionospheric scientist have already detected stimulated HF emission coming from the ionosphere Leyser (2001). In this phenomenon Langmuir waves are stimulated at frequencies around high power transmitters pointed at the F-region of the ionosphere. While the Langmuir waves are generated artificially, the emission mechanism may be relatable to that in meteor trails.

5.6.3 Spectral Sweeps

The spectral sweeps of FB1 described in §5.4.2 appear distinct among the rest of the emission. The short burst-like nature and polarization do indeed set it apart from the bulk of the emission in both FB1 and FB2. While we do not have an explanation for the linear polarization we suggest that the frequency-time dispersion could be the result of high density clumps of plasma expanding into a lower density trail.

To explore this idea, let us assume that small spheres of plasma with high electron density form within a less dense trail and diffuse isotropically in three dimensions. Let us also assume no significant recombination occurs on the time scale of the expansion. Using the conservation of particle number within an expanding sphere we obtain:

$$N_i = n_{ei}\frac{4}{3}\pi r_i^3 = n_e(t)\frac{4}{3}\pi r^3(t), \tag{5.11}$$

where N is the initial number of free electrons, n_e is the electron density, r is the radius of the sphere, and the subscript i denotes initial values.

In this scenario we assume that the number of electrons contained within a growing sphere is constant, and that the entire sphere is kept at a uniform, yet decreasing electron density. We can approximate the radius of the sphere with the mean square displacement

$$r^2(t) = 6Dt + r_i^2, \tag{5.12}$$

where D is the diffusion coefficient, which is typically given in cm^2s^{-1}, and depends exponentially on the height within the atmosphere (Ceplecha et al., 1998; McKinley, 1961). It should be noted that diffusion at high altitudes ($\gtrsim 100$ km) becomes nonlinear and no longer follows the mean square displacement (Dyrud et al., 2001; Oppenheim et al., 2003). Moreover at altitudes above 95 km the trails diffuse primarily along the geomagnetic field lines, creating elongation along this direction (Jones, 1991; Oppenheim & Dimant, 2015). Both of these effects are subjects of current research, and further study of the radio emission may prove useful in the future of this field.

To avoid a more complicated diffusion scenario we assume that these clumps are lower than 95 km and that diffusion is unaffected by the geomagnetic field. Substituting the mean square displacement for the radius in Equation 5.11 and substituting in the plasma frequency we get:

$$f_p^2(t)(6Dt + r_i^2)^{3/2} = f_{pi}^2 r_i^3. \tag{5.13}$$

Solving for t as a function of f_p we get:

$$t(f_p) = \frac{r_i^2}{6D}\left[\frac{f_{pi}^{4/3}}{f_p^{4/3}} - 1\right] + \tau, \tag{5.14}$$

where τ is the time when the sweep began, $t(f_{pi})$. Given this model we refit the eight sweeps of B2 using Equation 5.3 with b fixed to 4/3. The results are given in Table 2. We also fit the most defined sweep of B3, which is shown in Table 2 as #9. Holding b at 4/3 had only a small effect on the goodness of the fit with only minor decreases in the coefficient of determination (R^2). Despite this decrease, it is possible that the functional fit is the correct form, with the discrepancy being a result of a systematic error in the way the points were acquired. Nevertheless, if we assume that the fit is correct, the values for a allow us to estimate D using:

$$D = \frac{f_{pi}^{4/3} r_i^2}{6a}. \tag{5.15}$$

While we do not know the exact values for r_i and f_{pi}, if the model is correct, ballpark estimates should get us to the right order of magnitude of D. If we assume $r_i = 400$ cm and $f_{pi} \sim 100$ MHz, D ranges from 9,000 to 11,000 cm^2 s^{-1} for the eight modeled sweeps in B2 and 3,700 cm^2 s^{-1} for the sweep seen in B3. The estimates of D for all modeled sweeps are tabulated in Table 2.

From the NASA All-Sky Fireball Network we know that the plasma trail for FB1 had an upper altitude of 100 km and lower altitude of 86 km. Based on the atmospheric density, we would expect meteors in this range to have dispersion coefficients

in the range of 5,000 to 15,000 cm^2 s^{-1} (McKinley, 1961; Ceplecha et al., 1998; Wislez, 1995). Our estimates for the B2 sweep indicate they occurred in the middle ($\sim$ 92 km) of the trail, which is where the PASI images show B2 was pointed. This altitude also agrees with our assumption that the clumps were below 95 km, above which our diffusion assumptions become invalid. Our estimate for the B3 sweep indicates that it occurred just below the lower end ($\sim$ 85 km) of the trail, which is where the PASI images show B3 was pointed. The fact that the estimate for the B3 sweep is slightly low may mean that we are under estimating the initial radius or initial plasma frequency for this sweep. Indeed the fact that these pulses are much broader in time and frequency than those seen in B2, could be a clue that they were larger in size to begin with.

At the same time we should emphasize that we really only guessed at the initial radius in the first place, and due to the square dependance, a small error in r_i would have a large effect on D. Furthermore r_i would most likely have a strong dependance on the height, further complicating the determination of D, which itself was more complicated than the simple linear model we assumed to begin with.

Next let us look at the modeled values for c. For all eight sweeps of B2 the values lay between 9.9 and 10.1 s. We can use Equations 5.3 and 5.14 to get:

$$\tau = a/f_{pi}^{4/3} + c \qquad (5.16)$$

Therefore assuming this model is correct, we know that all of these sweeps must have started sometime after $\sim$9.9 s. This implies that there must be some mechanism triggering the formation of these clumps long after the meteor disintegrated. Moreover it is interesting to note that the one sweep modeled in B3 had c = -6.7. Since the sweep could not start before the onset of the fireball, we set $\tau \geq 0$ s, which yields $f_{pi} \leq 106$ MHz. This limit is certainly well within the physical bounds, and

this would mean that $r_i \gtrsim 500$ cm for the sweeps in B3, assuming that $D \gtrsim 3{,}700$ cm^2 s^{-1}.

The regular periodicity of the sweeps could be a sign that the plasma is interacting with a large amplitude acoustic wave with a period of 0.1 to 0.2 s (5 to 10 Hz). Such a wave may be resonating within the trail and forming the dense plasma clumps through large neutral density fluctuations and plasma instability. These clumps would then begin to diffuse outward, sweeping through plasma frequency with a temporal separation of 0.1 to 0.2 s. A formal derivation of this mechanism is beyond the scope of this chapter, but future exploration of this idea could prove useful.

As noted earlier we did not take into account the effects from the geomagnetic field, which decreases the diffusion rate in the direction perpendicular to the geomagnetic field. At sufficiently high altitudes ($\gtrsim 100$ km) the diffusion is much greater in the direction of the geomagnetic field, creating a non-spherically symmetric expansion (Ceplecha et al., 1998; Oppenheim & Dimant, 2015). The small clumps of plasma would then expand as an ellipsoid rather than a sphere, meaning the functional dependence of t on f_p would be different. Similar to the derivation of Equation 5.14, it can be shown that in the case of a cylinder expanding only in length, $t(f_p) \propto f_p^{-2}$. Therefore an expanding ellipsoid would have a value of b between 4/3 and 2.

In addition it should be noted that most large fireball trails have a dusty component (Kelley et al., 1998), and it is thought that a build up of charge onto the dust may aid in the process of long duration meteor echoes (Kelley, 2003). We did not consider this dusty component but it may indeed need to be considered in further studies of the radio emission.

5.7   Conclusions

The dynamic spectra presented here confirm the earlier discovery of long duration, non-thermal radio emission from fireballs, occurring near the plasma frequency. The spectra also confirm that the bulk of the emission is broadband, unpolarized and has a fairly smooth and steep spectrum. Furthermore the high temporal and frequency resolution of the LWA1 has allowed for the detection of finely structured, linearly polarized sweeps on top of the smooth unpolarized emission in one of the two fireballs observed.

Using the all sky imaging capabilities of the LWA1 as well as the triangulation of the NASA All Sky Fireball Network, we correlated the different appearance of these sweeps with different heights of the plasma trail. The broad sweeps of ~ 1 s width and higher dispersion are connected with the lower end of the trail at a height of ~ 85 km, and the narrow sweeps of ~ 0.2 s width with lower dispersion have been connected with the middle portion of the trail at a height of ~ 92 km. It was shown that the bulk of the dispersion cannot be caused by typical electromagnetic dispersion within a plasma and that some other explanation is necessary. The sweeps also displayed complicated frequency dependence in Stokes Q with 80% -Q at 43 MHz and 50% +Q at 51 MHz, and the amount of polarization dropping off significantly within 1 MHz on either side of these frequencies. It was shown that this change in polarization angle is almost certainly a feature of the emission and not due to Faraday rotation.

We postulated that the emission is most likely due to radiation of simple plasma oscillations (Langmuir waves), and modeled the sweeps as clumps of high density plasma diffusing into a lower density surrounding. The expanding clump model does provide a reasonable explanation for the frequency-time dispersion as the plasma frequency of the clump changes. However this model does not explain the observed

Table 5.1: Pulse Sweep Parameters

Sweep #	a s MHz^b	b	c s	R^2
1	1042	1.31	10.0	0.9993
2	1778	1.48	10.9	0.9994
3	3413	1.67	11.6	0.9996
4	5630	1.81	12.0	0.9998
5	836	1.19	9.0	0.9997
6	608	1.07	8.0	0.9996
7	493	0.989	7.1	0.9995
8	280	0.7746	4.0	0.9998

linear polarization features.

A second LWA station is under construction at the Sevilleta National Wildlife Refuge, about 75 km distant from LWA1. This should allow for triangulation of fireballs leading to precise measurements of the heights and trajectories of the fireballs. Eventually it will be possible to employ radio interferometry techniques to image the fireballs in detail and measure their expansion.

5.8 Acknowledgments

Table 5.2: Pulse Sweep Parameters

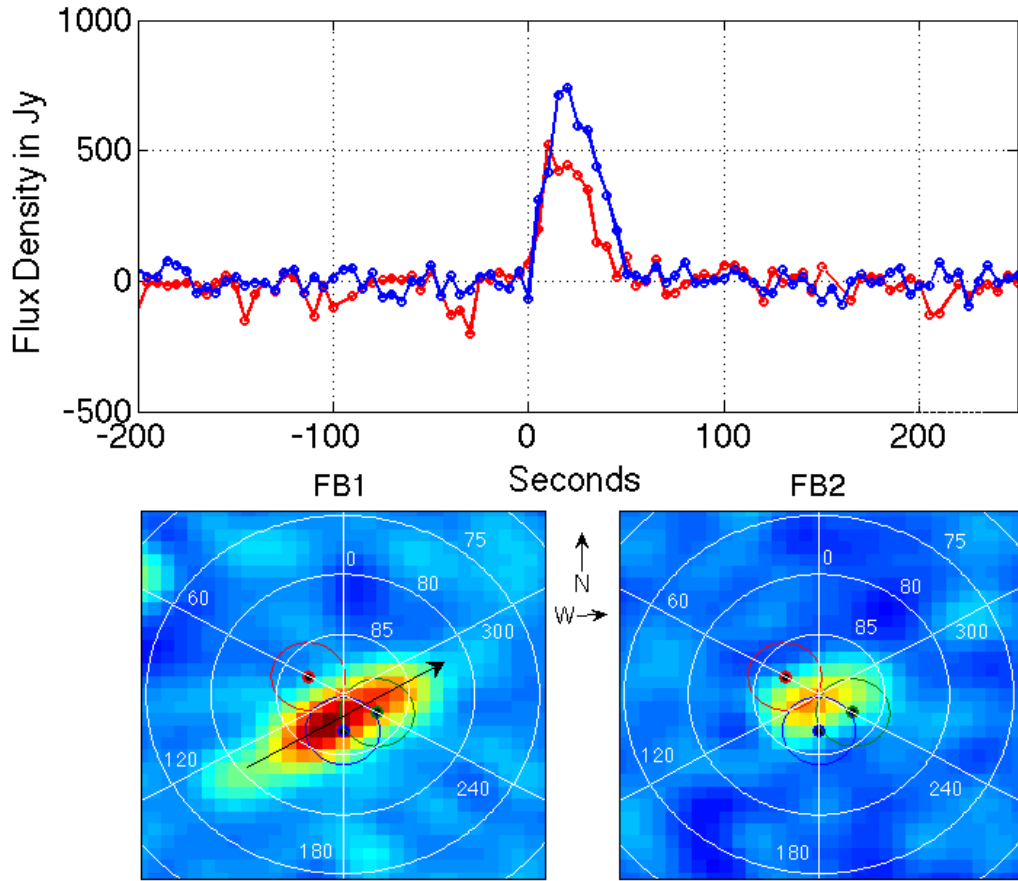| Sweep #	a	b	c	R^2	D
	s MHz$^{4/3}$		s		cm^2 s^{-1}
1	1,101	4/3	10.1	0.9993	11,242
2	1,120	4/3	10.2	0.9993	11,051
3	1,158	4/3	10.2	0.9995	10,689
4	1,222	4/3	10.0	0.9995	10,129
5	1,274	4/3	9.9	0.9997	9,716
6	1,315	4/3	9.9	0.9995	9,413
7	1,356	4/3	9.9	0.9994	9,128
8	1,382	4/3	9.9	0.9997	8,956
9	3,344	4/3	-6.7	0.9990	3,701

Figure 5.1: Top: Light curves showing the flux density from the brightest region from both fireballs. Units are in Janskys. (1 Jy = 10^{-23} erg s^{-1} cm^{-2} Hz^{-1}) Bottom: Closeups of the averaged images of the FB1 (left) FB2 (right). The image for FB1 also shows an arrow indicating the trajectory of the fireball heading NW. Also shown are the locations of B1 (Red), B2 (Blue), and B3 (green), each encircled by the estimated full width at half maximum (FWHM) beam size at 38 MHz. A horizontal coordinate map is overlaid on the image, and each pixel is approximately $1° \times 1°$.
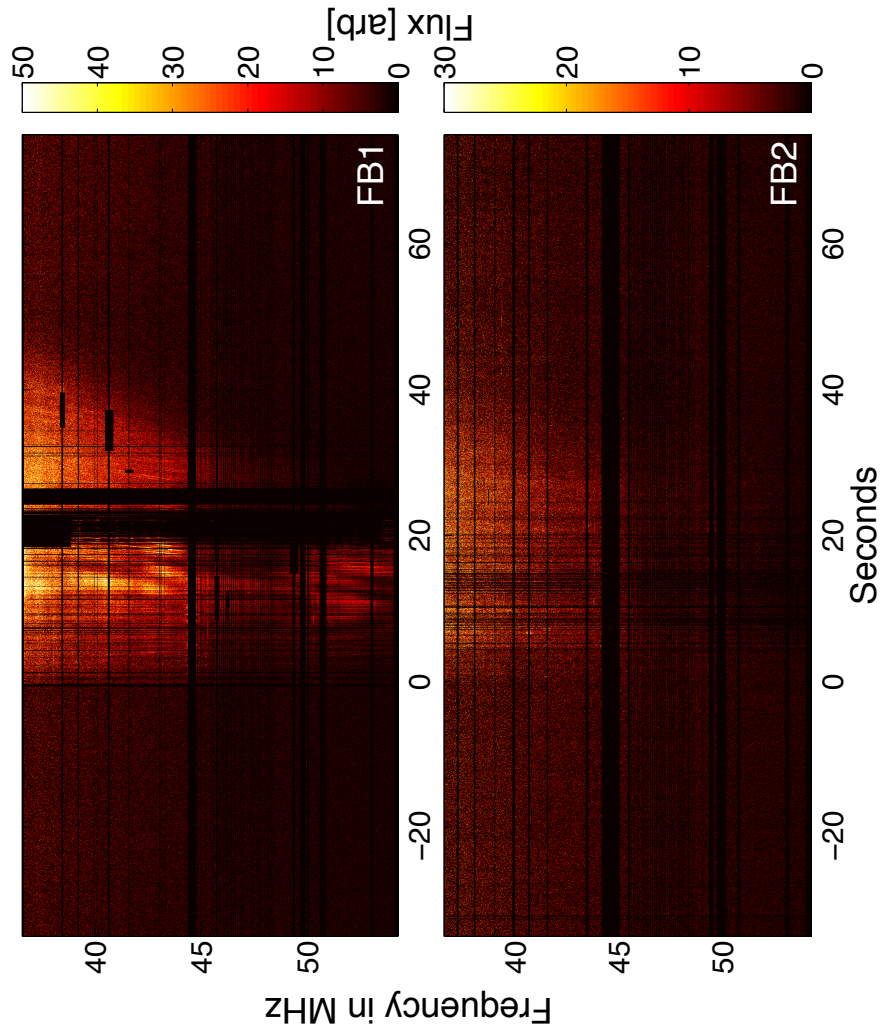
Figure 5.2: Dynamic spectra from B2 for FB1 (top) and FB2 (Bottom). Flux scales are in arbitrary units, but are the same for both FB1 and FB2. However notice that the color axes of FB1 and FB2 are different.

Figure 5.3: A closeup of the dynamic spectrum from B2 of FB1 from 12 to 20 seconds, shown in both Stokes I (top) and Stokes Q (bottom). For Stokes Q, positive values correspond to East-West polarization, and negative values correspond to North-South Polarizations.

Figure 5.4: A closeup of the dynamic spectrum from B2 of FB1 from 27 to 35 seconds, shown in both Stokes I (top) and Stokes Q (bottom). For Stokes Q, positive values correspond to East-West polarization, and negative values correspond to North-South Polarizations.
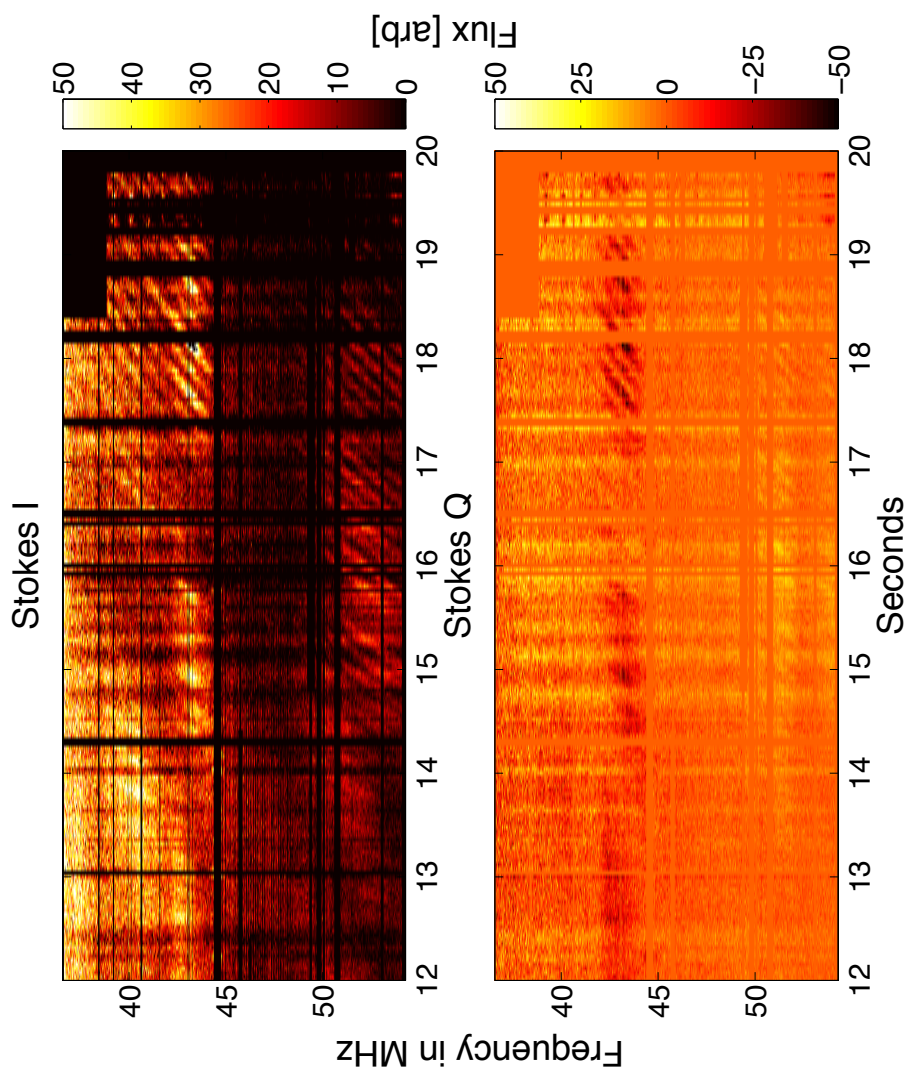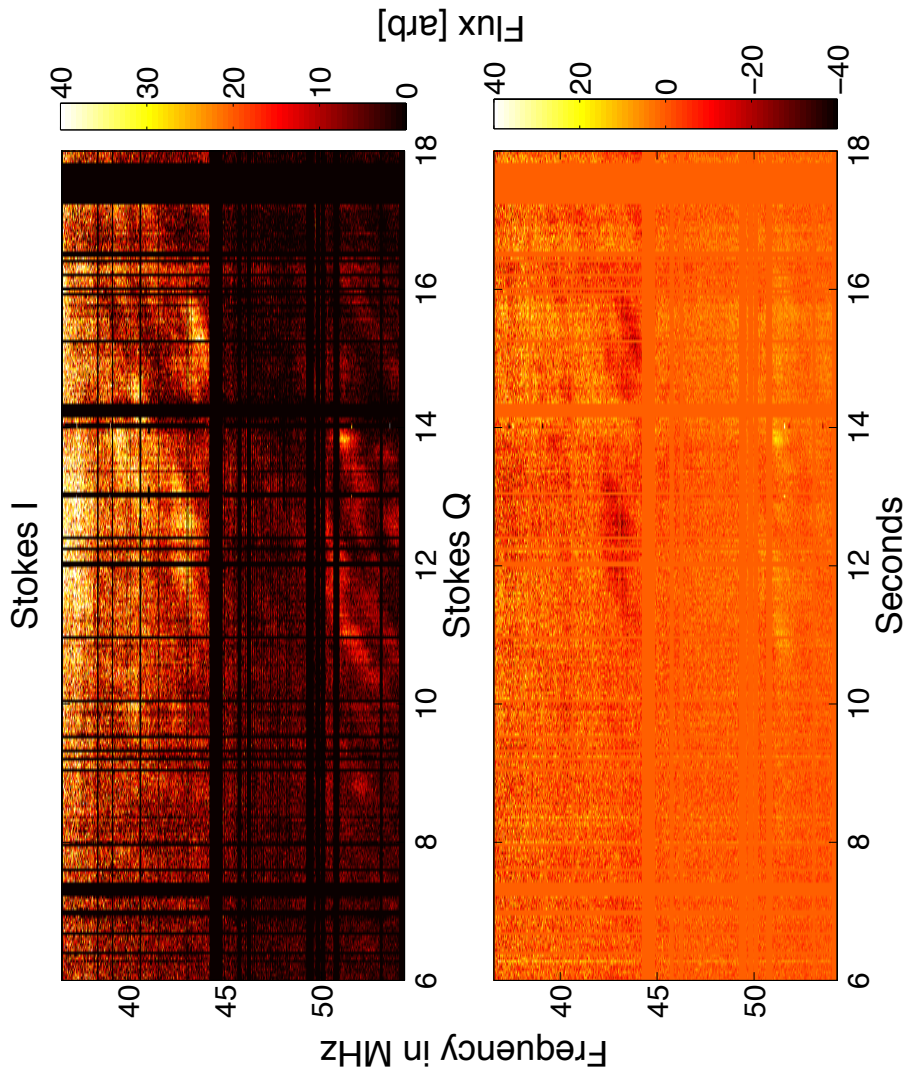
Figure 5.5: A closeup of the dynamic spectrum from B3 of FB1 from 6 to 18 seconds, shown in both Stokes I (top) and Stokes Q (bottom). For Stokes Q, positive values correspond to East-West polarization, and negative values correspond to North-South Polarizations.
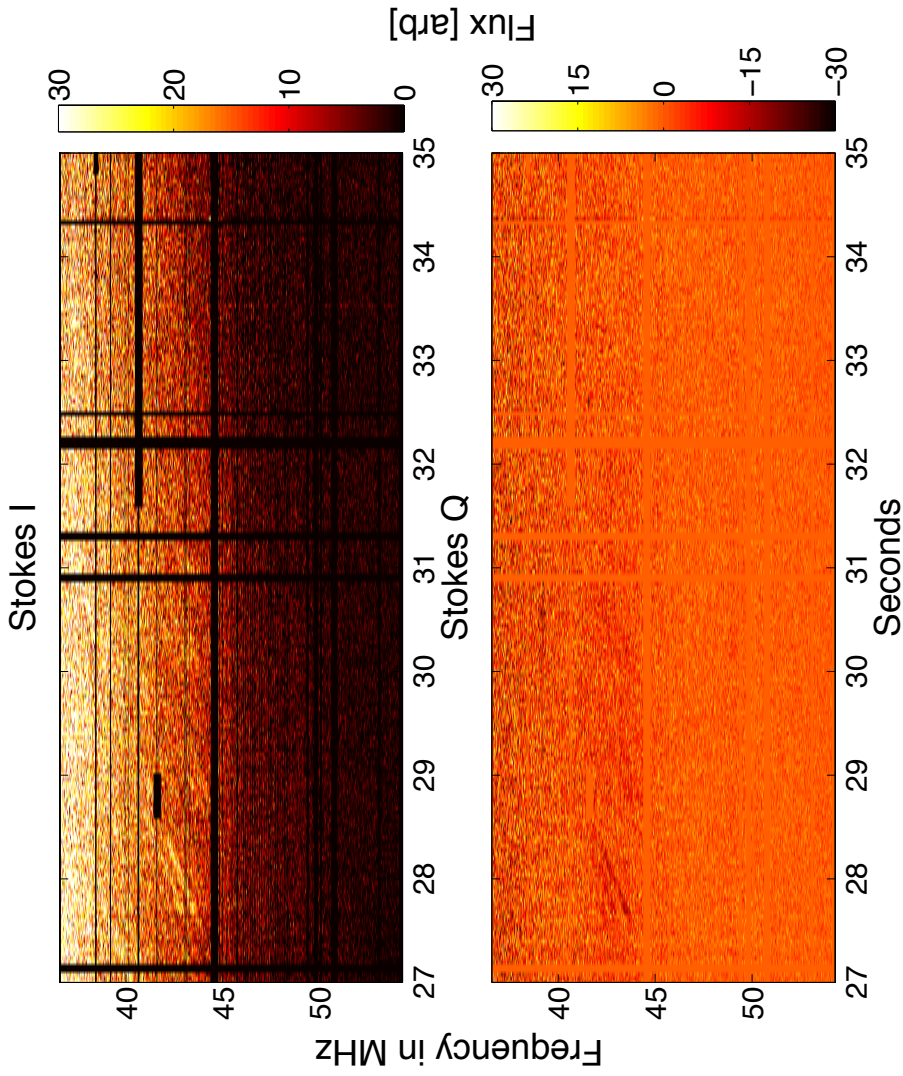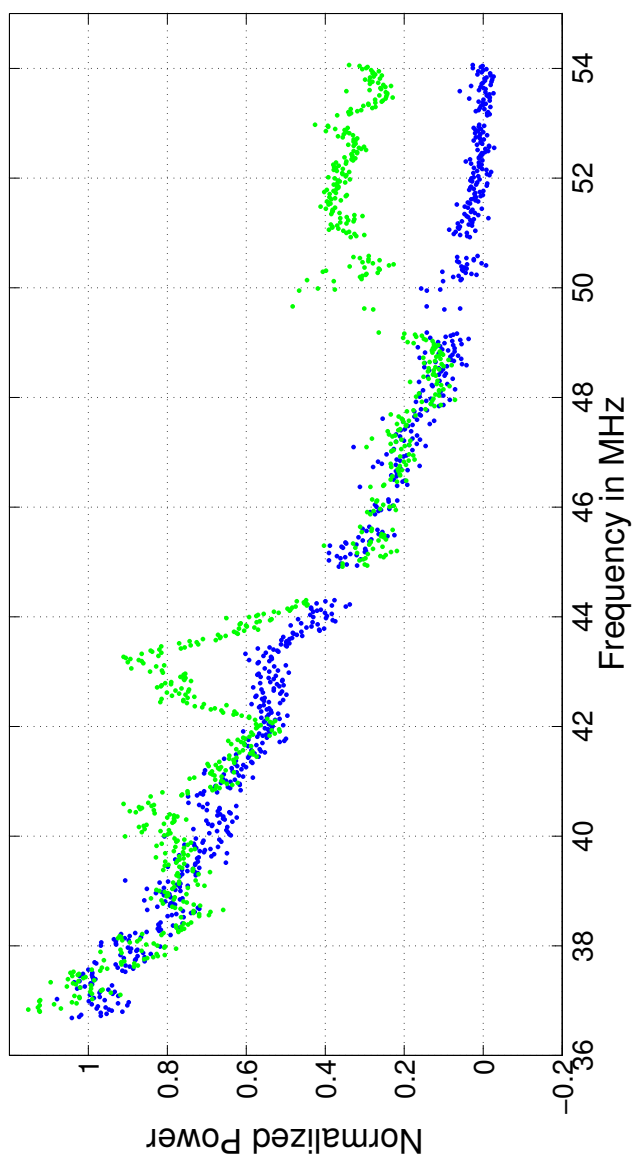
Figure 5.6: Comparing the averaged spectra from B2 of the 14th to 20th second (green) and the 26th to 34th second (blue) for FB1. Both averaged spectra have been corrected for bandpass, sky, and beam contributions, and are normalized to the brightest averaged frequency. As can be seen there is enhanced emission from 40 to 41, 42 to 44, and 49 to 54 MHz. These bumps correspond to the polarized frequency sweeps.
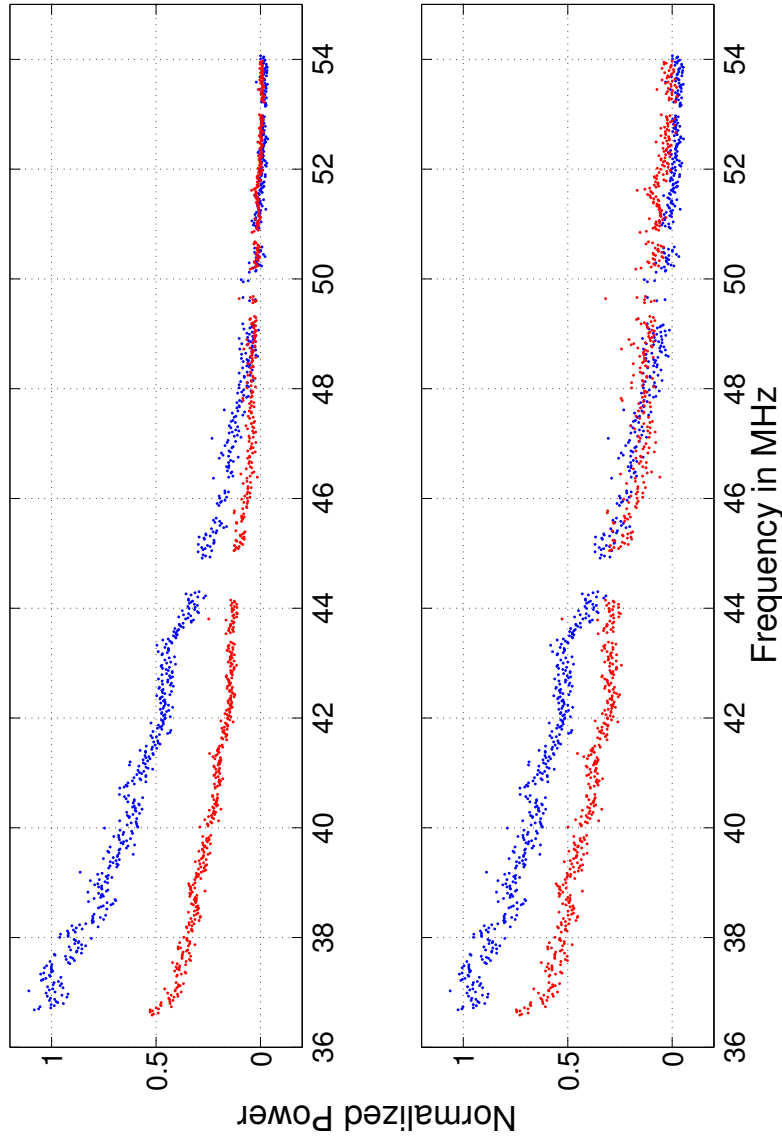
Figure 5.7: (Top) Mean spectra from FB1 (blue) and FB2 (red) after bandpass and sky contribution are removed, but before the beam contribution is removed. (Bottom) Mean spectra after beam contribution has been divided out. Both plots are normalized to the brightest region of FB1. Note: For FB1 only the averaged spectra between the 26th and 34th seconds are used, whereas for FB2, the entire duration of the emission is averaged.

Chapter 6

Astronomical Transients Limits

This chapter contains an updated version of the results originally published as part of Obenberger et al. 2014, Journal of Astronomical Instrumentation, 4, id. 1550004.

To date PASI has found 104 transients between 25.6 and 37.9 MHz, by searching 16,000 hours of data recorded between 25.6 and 74.0 MHz. Of these 104, 18 have been directly correlated with optical fireballs, but nearly all of the remaining 86 events display a fast linear rise followed by a longer exponential decay similar to the 18 fireball correlated events. Furthermore, the events are correlated strongly with dates of meteor showers. This evidence suggests that a large fraction, if not all, of these transients are bursts of non-thermal radio emission from fireballs (Obenberger et al., 2014b). The fact that not all have optical counterparts, is most likely due to the fact that the events occurred outside of the field of view of the NASA Fireball Network, they occurred during daylight, or they occurred on a cloudy night. By assuming that all of the 104 transients are fireballs, we can place limits on the rate density of astronomical transients that are an order of magnitude lower than previously set by similar studies at these frequencies (Cutchin, 2011; Kardashev et al., 1977; Lazio et al., 2010). However it should be noted that some of the transients may indeed be

related to some other phenomenon.

Since 93% of the data recorded by PASI has been at 38, 52, and 74 MHz, we only provide transient limits for these frequencies. While PASI has an extensive amount of sky coverage, the sensitivity is not uniform across the sky. As shown in §2.5.1 the sensitivities of subtracted PASI images at zenith are 41, 19, and 35 Jy at 38, 52, and 74 MHz and follow the zenith angle dependance shown in Figure 2.5. At a zenith angle of 40° the RMS sensitivities are 56, 24, and 60 Jy, while at a zenith angle of 60° the RMS sensitivities are 90, 38, and 95 Jy. However, the portion of the sky with zenith angles $< 40°$ includes 23% of the sky above the LWA1, while zenith angles $< 60°$ includes 50%.

With the above considerations we place rate density limits on transients at 38, 52, and 74 MHz occurring at zenith angles $< 60°$ brighter than the thresholds of 540, 230, and 570 Jy (6σ at z $= 60°$). With 11,400 hours recorded at 38 MHz and 8,353.7 deg^2 of sky observable on thresholds[1] of > 540 Jy, the transient rate density is limited to $< 8.8 \times 10^{-5}$ yr^{-1} deg^{-2}. These limits are for 5 s integrations, and we assume that the transients are 5 s rectangular pulses and that the entire duration of each pulse lies within one integration. Under these assumptions the pulse energy density limit becomes $> 2.7 \times 10^{-23}$ J m^{-2} Hz^{-1}.

Similarly for 1,900 and 1,400 hours recorded at 52.0 and 74.0 MHz, the rate density for 5 s transients at those frequencies is limited to $< 5.6 \times 10^{-4}$ and $< 7.2 \times 10^{-4}$ yr^{-1} deg^{-2} with pulse energy densities of $> 1.1 \times 10^{-23}$ and $> 2.8 \times 10^{-23}$ J m^{-2} Hz^{-1}. Table 6.1 shows these values with comparison to similar studies at these frequencies, which were discussed in §1.4. PASI has decreased the existing rate density limits by an order of magnitude for comparable pulse energy densities at

---

[1]At zenith angles $< 60°$, the flux density thresholds at each frequency begin to include the regions within the Galactic plane that are held at higher S/N thresholds because the sensitivity gets better at smaller zenith angles. Combining the regions removed for bright sources and the high threshold set for diffuse emission excludes 19% of the sky.

these frequencies.

It should be noted that no dedispersion is applied on the PASI data, therefore we begin to lose sensitivity to transients with high dispersion measures (DM) due to dispersion smearing (Obenberger et al., 2014a). For 5 s bursts at 38, 52, and 74 MHz, the S/N drops[2] by > 1.5 at $DMs > 220$, 570, and 1,600 pc cm^{-3}. However, if the bursts are longer than 5 s then dispersion smearing has a smaller effect on the sensitivity. For instance, if the burst lasted 30 s then the S/N would drop by 1.5 at DMs of 1,300, 3,400, and 9,800 pc cm^{-3}.

These limits are more sensitive than those for GRBs reported in Chapter 3. This is because the method used to search for GRB emission was not as sensitive as that used in this blind search, specifically image subtraction using a running average. Therefore these limits may then be applied to GRBs as well as any other transient phenomenon generating pulses on 5 s timescales. Furthermore these limits are applicable to all of the potential sources discussed in Chapter 1, and any search for such emissions would need to improve upon the sensitivity of PASI.

It is interesting to note that bright Crab Giant Pulses (CGP) are within the energy density limits of PASI and are readily detectable with LWA1 beam formed observations (Ellingson et al., 2013b). For instance, 1 s CGP above 1 kJy would be detectable by PASI at 52 MHz. However the Crab pulsar is imbedded within the Crab Nebula (Taurus A), supernova remnant that is ~ 2 kJy. This source undergoes a large amount of scintillation, and is therefore ignored by PASI. Even if we had searched this source for CGPs, we would not be able to decipher the difference from scintillation of the nebula. Beam observations are able to make this distinction because the large bandwidth allows for measurements of the characteristic frequency time dispersion expected from a pulse.

---

[2]The factor of 1.5 was chosen as a reference because it is roughly half the range of the zenith angle dependent RMS function.

Table 6.1: Pulse Rate Limits

Name	Frequency (MHz)	Rate Density $(\mathrm{yr}^{-1}\ \mathrm{deg}^{-2})$	Pulse Energy Density $(\mathrm{J\ m}^{-2}\ \mathrm{Hz}^{-1})$	Pulse Width
Kardashev et al. (1977)	60	10^{-3}	3.1×10^{-22}	0.5 s
	38	1.5×10^{-3}	2.1×10^{-22}	0.5 s
Lazio et al. (2010)	73.8	10^{-2}	1.5×10^{-20}	300 s
Cutchin (2011)	38	2.5×10^{-1}	2.6×10^{-23}	3 s
This dissertation	38	8.8×10^{-5}	2.7×10^{-23}	5 s
	52	5.6×10^{-4}	1.1×10^{-23}	5 s
	74	7.2×10^{-4}	2.8×10^{-23}	5 s

Chapter 7

Conclusions

7.1 Summary of the Chapters

The chapters of this dissertation have presented a variety of transient Radio astronomy research using the LWA1 telescope. This research was initiated with a targeted search followed by a blind search, a discovery, and a followup study to that discovery. This was accomplished using a combination of LWA1 beam formed data and all sky image data.

The Prototype All-Sky Imager (PASI) was introduced in Chapter 2 and its capabilities were described in full. PASI is a backend correlator of the LWA1 and is able to produce images of the entire visible sky between 10 and 88 MHz in near real time. Because of its large field of view, covering nearly $2\,\pi$ sr instantaneously, high sensitivity, and good time resolution, the LWA1 + PASI is a fantastic transient finding instrument.

As described in Chapter 3 the PASI all-sky images were first used to place stringent limits on prompt low frequency radio emission from GRBs. We placed $5\,\sigma$ limits

on 34 GRBs ranging from 175 to 1000 Jy for pulses longer than 5 s at 38, 52, and 74 MHz. In the search for prompt GRB emission we discovered two transients of unknown origin, displaying a fast rise and exponential decay. These transients had a flux density of nearly 1 kJy and lasted for about a minute each.

This discovery sparked a search of a much larger data volume, which in turn resulted in the discovery of 47 more events. Many of these events were then correlated with optical observations large meteors (fireballs) and it was soon thereafter revealed that they were the result of radio emission from the plasma trails left by fireballs, a previously unknown phenomenon. This discovery was presented in Chapter 4. While the bandwidth of the PASI correlator is much too small for spectral characterization, we made arguments based on the extreme brightness temperature that the emission could not be thermal.

This hypothesis was confirmed with broadband spectra captured for two events, which was presented in Chapter 5. These spectrograms, which cover 36 - 55 MHz show that the fireballs emit a very broad and steep spectrum. The emission was both brighter and of longer duration at lower frequencies, and in addition to the emission we also detected many man-made signals reflected off the plasma trail. We noted that the emission at any given frequency lasted a similar duration to reflections at nearby frequencies. This fact along with a lack of any other explanation prompted the hypothesis that the emission was likely coming from the radiation of plasma waves, since both the duration of the radiation and reflections at any frequency would be related to the plasma frequency of the trail.

In the case of one of the two measured fireballs we found frequency/time dispersed pulses sweeping across the entire band. These sweeps were linearly polarized and followed an inverse power law dependance on the frequency. We modeled the sweeps as individual clumps of diffusing plasma. These models yielded reasonable values for the diffusion constants at the altitude of the trails.

Table 7.1: Circular Polarized Pulse Parameters

Date	Time (UTC)	RA (Deg)	Dec (Deg)
12/31/2012	02:04:35	23h 32m 24s	+47d 00m 00s
07/21/2014	03:54:23	18h 07m 36s	+15d 42m 00s

Finally we reported the transient rate density and pulse energy density limits, which we arrive at presuming all of the transients found by PASI are indeed fireballs. Since all the transients were found at frequencies below 50 MHz, the limits at 52 and 74 are certain, however it is currently impossible to know if all the transients found at 38 MHz are indeed fireballs. The fact that there remains good correlation between the events and meteor showers does at least suggest that most of these events are meteoritic in origin. Future studies with multiple stations will be able to be able to use anti coincidence to determine if the origin of the transients is atmospheric or celestial.

It is interesting to note that there are two events that showed high $> 50\,\%$ circular polarization, without any linear polarization, and both of these events were detected at 38 MHz. The dates, times, and locations of the events are given in Table 7.1. The fact that they are circularly polarized certainly separate them from the rest of the transient events, and may indicate an origin other than meteors. However, with such limited spectral information it is difficult to say what they could be, and with only one detection from each location it is currently impossible to rule out RFI. As mentioned in §2.5.4 ionospheric scintillation of celestial sources can cause circularly polarized transients. While no sources above 20 Jy were within a beam width of these events, it is possible that dimmer objects could undergo an extreme ionospheric scintillation event and be responsible for the events. If these sources are indeed celestial in origin, likely candidates could then be extrasolar Jupiter sized planets or flare stars.

7.2 Future Work

7.2.1 Transient Search: All-Sky

While PASI does not fully utilize the full bandwidth and therefore the full sensitivity potential of the LWA1, it is still more sensitive than previous transient finding instruments. Moreover the fantastic field of view combined with unparalleled observing time enables extremely stringent rate density limits, especially at 38 MHz. Even with a more sensitive instrument it may take a considerable amount of observing time to beat the limits set here in this dissertation. Such sensitivity improvements would presumably be gained with a wider bandwidth, which would require more computation and sophistication in RFI rejection. These facts should be taken into consideration when designing future transient finding experiments.

The LWA-OVRO (Owens Valley Radio Observatory), is a next generation LWA station designed to search for auroral emission from Jupiter sized planets as well as emission from flare stars. With all-sky imaging analogous to PASI, but 60 MHz of bandwidth and greater angular resolution, LWA-OVRO will push beyond the sensitivity of PASI by nearly a factor of 50 (Hallinan et al., 2015). However this sensitivity improvement assumes that the target sources emit fully across this 60 MHz, which may not be the case for exoplanets.

The LWA-SV (Sevilleta), is currently under construction at the Sevilleta National Wildlife Refuge. This station will have similar wideband all-sky imaging capabilities to LWA-OVRO and will be a useful transient searching instrument as well. Both LWA-SV and LWA-OVRO could be used simultaneously with the LWA1 to provide anti coincidence observations when looking for transients.

Using all-sky images for non dispersed pulses is generally very easy, and can be carried out in a manner described in §2.5.1. However searching for dispersed pulses

would be far more complicated. This is because all-sky imagers typically do not track sources, they simply phase to zenith before they correlate and image (see. §2.3.1). This method is adequate if all the frequencies of a pulse arrive at the same time. If they are staggered as in the case of a dispersed pulse, then that source will appear in different pixel locations across the observed band. For larger DMs and lower frequencies this effect is large and would need to be corrected.

The best solution would be to phase to a specific RA and DEC before correlation, that way the pixel location of sources in the sky is constant and the images can simply be stacked. Another method would be to generate light curves for specific RAs and DECs, and simply average over frequency. This method would be much less sensitive however, since the amount of sky in each pixel would change from frequency to frequency as a result of sky being projected onto a 2D image.

7.2.2 Transient Search: Beam

As mentioned in §5.1 we have observed with LWA1 for ∼ 5000 beam hours for the purpose of searching for dispersed pulses. The search pipeline to look for pulses in this data is still under development, having taken a lower priority to the fireball research carried out in this dissertation. This project utilizes the spectrometer beam mode of the LWA1 to perform drift scans around zenith during PASI operation. See Figure 7.1. Each beam has two tunings each with 19.6 MHz of bandwidth, centered at 45.45 and 65.05 MHz. Forthcoming research using this data may yet find interesting results.

Similarly another LWA1 campaign is currently being carried out where beams are quickly pointed at the locations of GRBs triggered by notices from the GCN network. The LWA1 beams can be pointed in less than two minutes. The pipeline being developed for the drift scan observations is also to be used for this campaign.

Finally another campaign is currently being carried out where beams are being pointed at the known locations of several Jupiter sized extrasolar planets. These observations are being made with full polarization capabilities, since the expected auroral emission from these planets is circularly polarized. A positive detection of one of these planets would allow for the first magnetic field strength measurement of an extrasolar planet, and any measured periodicity of the emission would allow for calculations of the rotation rate of the planet.

An even more interesting application would be the possibly of detecting moons and measuring their contributions to the emission. The moons of Jupiter (especially Io) emit gas that is ionized by sunlight and particle collisions, and is funneled by the Jovian magnetic fields onto Jupiter's auroral regions. This process creates hotspots on Jupiter that follow the orbits of the contributing moon, and is made detectable by plotting the periodicity of burst probability. Similarly this method could be applied to extrasolar planets to make the first detections extrasolar moons, and measure their orbital parameters.

7.2.3   Radio Emission from Meteors

The discovery of radio emission from meteors, was quite unexpected, and certainly raises a large number of questions. The biggest of which is quite simply: How? As discussed in Chapter 4 and 5 the emission cannot be from a thermal process such as black body or Bremsstrahlung, nor can it be due to cyclotron radiation within the geomagnetic field. Furthermore the duration separates it from the short broadband radiation mechanisms such as EMPs, where uncoupled electrons radiate freely.

We have made the hypothesis that the emission is due to the radiation of plasma waves, such as Langmuir waves. However these waves are electrostatic, and therefore typically do not radiate out of a plasma (see §5.6.2). Moreover as discussed in §5.6.1

these waves would need to be constantly replenished since the collision rate at 80 - 110 km altitudes is so large. An analogy with Type III solar bursts suggested a weak electron beam could be responsible, and we show that only a very weak beam could be sufficient. A more rigorous theoretical explanation needs to be worked out.

The construction of LWA-SV only 75 km away from LWA1 offers a unique opportunity for co-observation of the same events. First, a mere detection of a fireball at both stations would 100% rule out any possibility that the detections are due to a reflected signal. Furthermore observations of the same meteor trail from the two stations could be correlated using near field imaging techniques. If fringes could be derived from these observations then the sizes of the emitting regions could be estimated. Such observations could pave the way for a future, 8 to 16 station LWA to make high resolution images of the emitting plasma trail. If the radiation is due to the emission of Langmuir waves, then the observed frequencies would trace out the electron density distribution within the trail. Therefore a simple map of the emitting region could in turn test our hypothesis of the emission mechanism.

Another unanswered question concerns what population of fireballs result in radio emission. It is currently unknown if all fireballs have an equal chance of emitting or if there are parameters such as velocity, mass, or ionospheric conditions that indicate likelihood. To better answer this question Fireball Network cameras need to be installed in closer proximity to the LWA1 and LWA-SV stations to better increase the odds of optical/radio observation. The optical observations would allow for velocity and magnitude measurements, which could then in turn be turned into mass estimates. Comparing these parameters from both the radio emitting events and the non radio emitting events may show trends. Also the amplitude of the radio emission could then be compared to these parameters to see if there is any correlation.
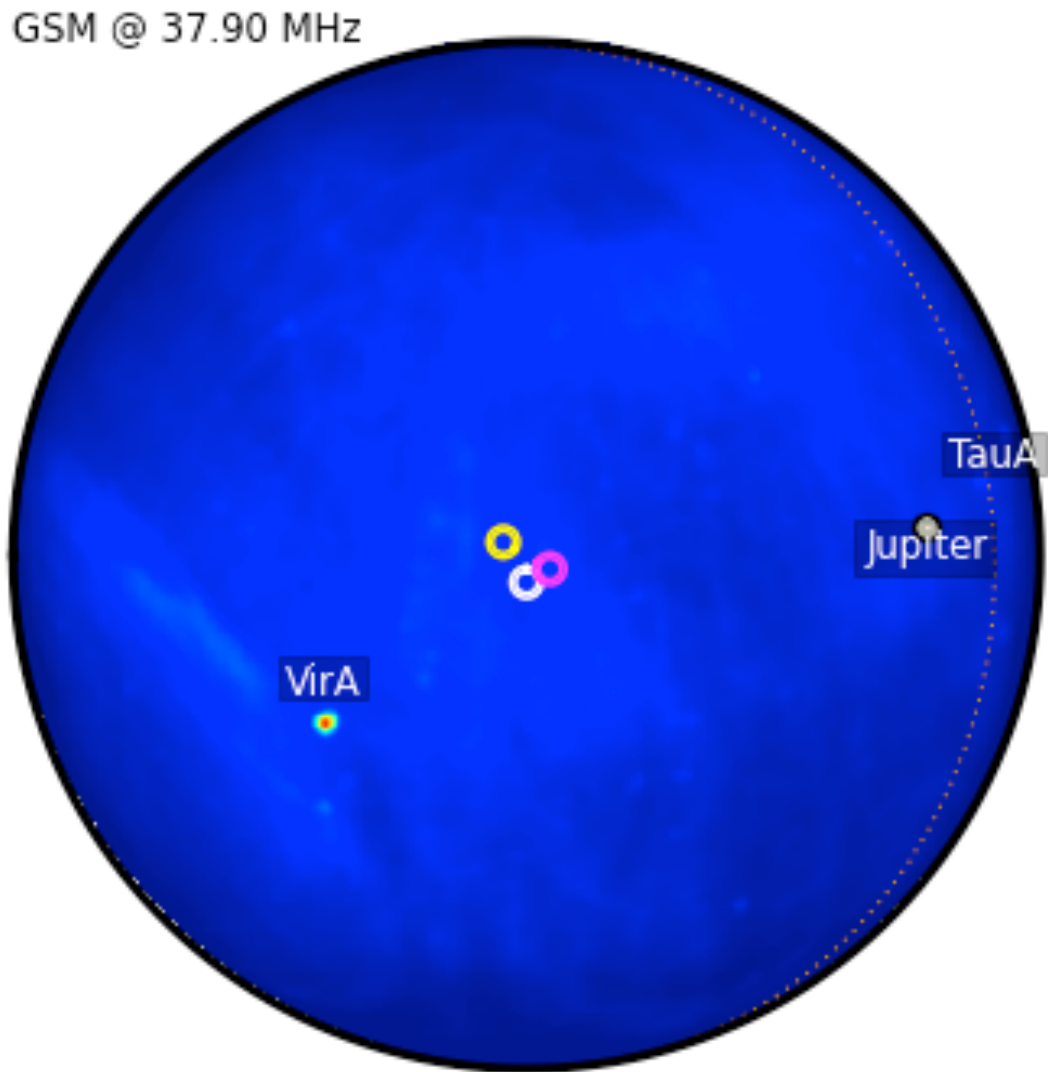
Figure 7.1: The locations of the three drift scan beams (colored rings), overlaid on a sky model at 38 MHz.

References

Baars, J.W.M., Genzel, R., Pauliny-Toth, I.I.K., & Witzel, A., 1977, A&A, 61, 1, 99

Baird, G.A., Delaney, T.J., Lawless, B.G. et al. 1975, ApJ., 196, L11

Balsano, R.J. 1998, Ph.D. Thesis, Princeton University

Bannister, K.W., Murphy, T., Gaensler, B.M., & Reynolds, J.E. 2012, ApJ, 757, 38, 15

Barthelmy, S. D., Butterworth, P., Cline, T.L. et al. 1995, Ap & SS, 231, 235

Barthelmy, S. D., Barbier, L.M., Cummings, J.R. et al. 2005, Space Science Reviews, 120, 3-4, 143

Beech, M., Brown, P., & Jones, J., 1995, Earth, Moon, and Planets, 68, 181

Bell, M.E., Murphy, T., Kaplan, D.L., et al. 1977, MNRAS, 438, 1, 352-367

Benz, A.O. & G. Paesold 1998, A&A, 329, 61

Berger E., 2014, Annu. Rev. Astron. Astrophys.,52, 43-105

Bezrodny, V.G., Charkina, O.V., Galushko, V.G. et al. 2008, Radio Science, 43, 6

Blandford, R.D. 1977, MNRAS, 181, 489

Borovicka, J. 2006, JRASC, 100, 194-198

REFERENCES

Bourdillon, A., Haldoupis, C., Hanuise, C., Le Roux, Y., & Menard, J., 2005 Gephysical Research Letters, 32

Bowman, J.D., Cairns, I., Kaplan, D.L. et al. 2013, PASA, 30, 28

Briggs, M.S., Connaughton, V., Meegan, C.A., et al. 2009, AIP, 1133, 40-42

Bronshten V.A. 1983, Physics of Meteoric Phenomena, D. Reidel Publishing Company

Burke, B.F., Franklin, K.L. 1955, JGR, 60, 2, 213

Burke-Spolaor, S., Bailes, M., Ekers, R., Maquart, J., & Crawford, F. 2011, ApJ, 727, 5

Burrows, D. N., Hill, J.E., Nousek, J.A. et al. 2005, Space Science Reviews, 120, 3-4, 165

Cairns, I. H. 1988, JGR, 93, 3958

Cairns, I. H., & Melrose, D. B. 1985, JGR, 90, 6637

Cameron, P. B., Chandra, P., Ray, A. et al. 2005, Nature, 434, 7037, 1112

Ceplecha, Z., Borovicka, J., Elford, W.G., et al. 1998 Space Science Reviews, 84, 327

Chu, X., Liu, A.Z., Papen, G., et al. 2000, GRL, 27,13, 1815

Close, S., Linscott, I., Lee, N. et al. 2010, AIP Physics of Plasmas, 20, 092102

Close, S., Kelley, M., Vertatschitsch, L. et al. 2011, JGR, 116, A1

Close, S., Linscott, I., Lee, N. et al. 2013, AIP Physics of Plasmas, 20, 092102

Coenen, T., van Leeuwen, J., Hessels, J.W.T., et al. 2014, A&A, 570, 60, 16

Cohen, A. S., Lane, W.M., Cotton, W.D. et al. 2007, AJ, 134, 1245

REFERENCES

Cutchin, S.E. 2011, Ph.D. Thesis, Virginia Polytechnic Institute and State University

Dessenne, C.A.-C., Green, D.A., Warner, P.J. et al. 1996, MNRAS, 281, 977

Dimant, Y. S., Oppenheim, M.M., & Milikh, G. M., 2009, Annales Geophysicae, 27, 1, 279

Dyrud, L. P., Oppenheim, M.M., & Axel, G. M., 2001, GRL, 28, 14, 2775

Ellingson, S.W., Craig, J., Dowell, J., Taylor, G.B., & Helmboldt, J.F. 2013, eprint arXiv:1307.0697

Ellingson, S.W., Clarke, T.E., Craig, J., et al. 2013, ApJ, 768,2, 136, 10

Frail, D.A., Kulkarni, S.R., Ofek, E. O., Bower, G.C., & Nakar, E. 2012, ApJ, 747, 1, 12

Ginzburg, V.L., 1973, Nature, 246, 415

Guha, A., De, B.K., Choudhury, A., & Roy, R. 2012, Astrophysics and Space Science, 341, 287

Gurnett, D. A. 2005, Introduction to Plasma Physics, Cambridge University Press

van Haarlem, M.P., Wise, M.W., Gunst, A.W. et al. 2013, arxiv, arXiv:1305.3550

Hales, S.E.G., Waldram, E.M., Rees, N., & Warner, P.J. 1995, MNRAS, 274, 2, 447

Hallinan, G., Antonova, A., Doyle, J.G., et al. 2008, ApJ, 684, 1, 644

Hallinan, G., Bourke, S., Anderson, M., et al. 2015, AAS Meeting 225, 328.01

Halliday, I., Griffin, A.A., Blackwell, A.T. 1996 Meteoritics and Planetary Science, 31, 185

Hansen, B.M.S. & Lyutikov, M. 2001, MNRAS, 322, 695

REFERENCES

Hawkins, G.S. 1958, Nature, 181, 1610

Helmboldt, J.F., Kassim, N.E., Cohen, A.S., Lane, W.M., & Lazio T.J., 2008, ApJS, 174, 2, 313

Helmboldt, J.F., Clarke, T.E., Craig, J., et al. 2013, Radio Science, 48, 491

Helmboldt, J.F., Ellingson, S.W., Hartman, J.M. et al. 2014, Radio Science, 49, 157

Hicks, B. C., Paravastu-Dalal, N., Stewart, K. P. et al., 2010, Publications of the Astronomical Society of the Pacific, 124, 920, 1090-1104

Hinkel-Lipsker, D. E., Fried, B. D., & Morales, G. J. 1992, Phys. Fluids B, 4, 1772

Hyman, S.D., Lazio, J.T., Kassim, N.E., & Bartleson, A.L., 2002, AJ, 123, 3, 1497

Hyman, S.D., Lazio, J.T., Kassim, N.E., et al. 2005, Nature, 434, 50

Hyman, S.D., Wijnands, R., Lazio, J.T., et al. 2009, ApJ, 696, 280

Ioka, K., 2003, ApJ, 598, L79

Inoue, S., 2004 MNRAS, 348, 3, 999

Jones, W. 1991, Planetary and Space Science, 39, 1283

Kallenrode, M.B. 1998, Space Physics: An Introduction to Plasmas and Particles in the Heliosphere and Magnetospheres, Springer-Verlag Berlin Heidelberg

Karastergiou, A., Chennamangalam, J., Armour, W., et al. 2015, MNRAS, 452, 2, 1254

Kardashev, N.S, Soglasnov, V.A., Savel'eva N.A. et al. 1977, Soviet Astronomy, 21, 1

Katz, J.I. 2014, arXiv:1403.0637

REFERENCES

Kavic, M., Simonetti, J.H., Cutchin, S.E., Ellingson, S.W., & Patterson, C.D., 2008, JCAP, 11, 017, 10

Keane, E.F., Stappers, B.W., Kramer, M., & Lyne, A.G. 2012, MNRAS, 425, L71

Keay, C.S.L. 1980, Science, 210, 11

Kellermann, K.I., Pauliny-Toth, I.I.K., & Williams, P.J.S., 1969, ApJ, 157, 1

Kelley, M. C., Alcala, C., & Cho, J. Y. N., 1998 Journal of Atmospheric and Solar-Terrestrial Physics, 60, 3, 359

Kelley, M. C., 2003 Radio Science, 39, 2

Kelley, M. C., 2009, The Earth's Ionosphere, Academic Press.

Kim, E.H., Cairns, I.H., & Johnson, J.R. 2013, AIP Physics of Plasmas, 20

Klebesadel, R.W., Strong, I.B., & Olson, R.A. 1973, ApJ, 182, L85

Kogan, L., Cohen, A. 2009, "A 110 m x 100 m Elliptical Station Design Optimized to Minimize Sidelobes" Memo 150, LWA Memo Series, http://www.ece.vt.edu/swe/lwa/memo/lwa0150.pdf

Koranyi, D. M., Green, D.A., Warner, P.J., Waldram, E.M., & Palmer, D.M. 1995, MNRAS, 276, L13

Kulkarni, S.R., Ofek, E.O., Neill, J.D., Zheng, Z., & Juric, M. 2014, 2014arXiv1402.4766

Lane, W.M., Cotton, W.D., Helmboldt, J.F., Kassim, N.E. 2012, Radio Science, 47, 6

Lazio,T. J.W., Clarke, T.E., Lane, W.M. et al. 2010, AJ, 140, 1995

Leyser, T.B., 2001, Space Science Reviews, 98, 3, 223

REFERENCES

Loeb, A., Shvartzvald, Y., Maoz, D. 2013, preprint (arXiv:1310.2419)

Loi, S.T., Trott, C.M., Murphy, T., et al. 2015, arXiv:1506.01798

Lorimer, D.R., Bailes, M., McLaughlin, M.A., & Narkevic, D.J., Crawford, F. 2007 Science, 318, 777

Lovell, B. 1963, Nature, 198, 4877, 228

Malaspina D.M., Cairns, I.H., Ergun, R.E. 2013, ApJ, 755, 45

T. C. Marshall, M. Stolzenburg, C. R. Maggio, et al., 2005, Geophysical Research Letters 32 3

Matsuoka, M., Kawasaki, K., Ueno, S. et al. 2009, PASJ, 61, 999

McKinley, D.W.R. 1961, Meteor Science and Engineering, McGraw-Hill

McLaughlin, M. A., Lyne, A. G., Lorimer, D. R., et al. 2006, Nature, 439, 7078, 817

McMullin, J. P., Waters, B., Schiebel, D., Young, W., & Golap, K. 2007, Astronomical Data Analysis Software and Systems XVI (ASP Conf. Ser. 376), ed. R. A. Shaw, F. Hill, & D. J. Bell (San Francisco, CA: ASP), 127

Meegan, C., Lichti, G., Bhat, P.N. et al. 2009, ApJ, 702, 791

Melrose D.B. 1987, Sol. Phys., 111, 89

Morales, M.F., Hewitt, J.N., Kasper, J.C., Lane, B., & Bowman, J. 2005, ASP Conference Series, 345, 512

Moortgat, J., & Kuijpers, J. 2004, Phys. Rev. D, 70, 023001

Murphy, T., Bell, M.E., Kaplan, D.L. et al. 2015, MNRAS, 446, 3, 2560

Nordgren, T.E., Cordes, J.M., & Terzian, Y. 1992, AJ, 104, 4, 1465

REFERENCES

Obenberger, K.S. Hartman, J.M., Taylor, G.B. et al. 2014, ApJ, 785, 1, 7

Obenberger, K.S., Taylor, G.B., Hartman, J.M. et al. 2014, ApJL, 788, L26

Obenberger, K.S., Taylor, G.B., Hartman, J.M. et al. 2015, Journal of Astronomical Instrumentation, 4

Obenberger, K.S., Taylor, G.B., Lin, C.S. et al. 2015, JGR Space Physics, Submitted

Obenberger, K.S & Dowell, J., 2011 "LWA1 RFI Survey" Memo 183, LWA Memo Series http://www.ece.vt.edu/swe/lwa/memo/lwa0183.pdf

Oppenheim M.M. & Dimant, Y.S., 2015 GRL, 42, 3, 681

Oppenheim M.M., Dyrud, L. P. & Ray, L., 2003 JGR Space Physics, 108, A2

Oyama K.I., Shimoyama, M., Liu, J.Y. & Cheng, C.Z., 2011, Annales Geophysicae, 29, 3

Papadopoulos, K. & Freund, H.P. 1978 GRL, 5, 881

Petroff, E., Bailes, M., Barr, E.D., et al. 2015, MNRAS, 446, 1, 246

Planck Collaboration 2013, arXiv, arXiv:1303.5090

Pshirkov, M. S., & Postnov, K. A. 2010, Ap&SS, 330, 13

Rees, M.J. 1977, Nature, 266, 333

Rees, N. 1990, MNRAS, 244, 233

Reid, H.A.S., Ratcliffe, H. 2014, RAA, 14, 7, 773

Rison, W., R.J. Thomas, P.R. Krehbiel, T. Hamlin, & J. Harlin, 1999, Geophysical Research Letters, 26, 3573-3576,

Sagiv, A. & Waxman, E. 2002, ApJ, 574, 861

REFERENCES

Schinzel, F.K. 2013, "The Influence of Shelter Temperature on Gain Stability of LWA1", Memo 198, LWA Memo Series http://www.ece.vt.edu/swe/lwa/memo/lwa0198.pdf

Schinzel, F.K. & Polisensky, E., 2014, "System Equivalent Flux Density of LWA1 Beams", Memo 202, LWA Memo Series http://www.ece.vt.edu/swe/lwa/memo/lwa0202.pdf

Schinzel, F.K., Polisensky, E., Dowell, J., & Taylor, G.B. 2015, AAS Meeting #225, #337.02

Spitler, L. G., Cordes, J. M., Hessels, J. W. T., et al. 2014, arXiv:1404.2934

Stevens, I. R. 2005, MNRAS, 356, 1053

Sugar, G., Oppenheim, M.M., Bass, E., Chau, J.L., JGRSP, 115, A12

Taylor, J.H., & Cordes, J.M. 1993, ApJ, 411, 2, 674

Taylor, G.B., Carilli, C.L., Perley, R.A. 1999, Synthesis Imaging in Radio Astronomy II, ASP Conference Series, Vol. 180

Taylor, G.B., Ellingson, S.W., Kassim, N.E., et al. 2012, Astronomical Instrumentation, 1, 1

Thornton, D., Stappers B., Bailes, M., et al. 2013, Science, 341, 53

Usov, V.V. & Katz, J.I. 2000, A&A, 364, 655

Warwick, J.W., Hayenga, C.O., & Brosnahan, J.W. 1979, Journal of Geophysical Research, 84, 2457

Wayth, R.B., Tingay, S.J., Deller, A.T. et al. 2012, ApJ, 753, 2, L36

Wei, T., Simonetti, J.H., Akukwe, B., et al. 2015, AJ, 149, 2, 65

REFERENCES

Wislez, J.M. 1995, Proceedings of the International Meteor Conference, Roggemans, P. & Knofel, A. , 83

S.E. Woosley & J.S. Bloom, 2006, Annu. Rev. Astron. Astrophys., Volume 44, pp. 507 - 556

Yancey, C.C., Bear, B.E., Akukwe, B. et al. 2015, ApJ S. Accepted

Zhou, B., Li, X., Wang, T. et al. 2014, Physical Review D, 89, 10